Imperial College London

Peridynamics Modelling of Weibull Distributions for Nuclear Fuel Fracture

Lloyd Jones

A thesis submitted in partial fulfilment for the degree of Doctorate of Philosophy

in the

Department of Materials & Centre for Nuclear Engineering,

June 2021

Declaration

This thesis is the work of Lloyd Jones, and work by any other author has been appropriately attributed.

Abstract

Peridynamics is a non-local continuum mechanics modelling method, with fundamental equations built upon integrals as opposed to partial differentials, which gives benefits when modelling brittle fracture relative to other continuum mechanics modelling techniques. Notably absent from peridynamics literature is an investigation of the effect of fracture strength distributions (an important element of brittle fracture) in peridynamics. This thesis outlines a method for appropriately including fracture strength distributions in peridynamics, and presents a model of a UO_2 fuel pellet fracturing in service using this method.

It was shown that using a Weibull distribution in peridynamics without adjusting the distribution of strengths to account for the difference in size between bonds and the part to be modelled produces inaccurate results. Using Weibull scaling to account for this did not alone solve this problem, as there was still a disconnect between the stress at which the first bond fails (stage 1 failure) and the stress at which the overall part modelled fails (stage 2 failure). Bond strengths were localised by linking bond strength to the material points they are connected to. Combining this localisation with using the most extreme strengths, the shape of the Weibull curve was accurately recreated in 1D peridynamics.

The method was applied in two dimensions, and it was shown that the method which had worked in one dimension is no longer adequate. It was found that edge length is the most appropriate size-scaling criteria, as opposed to total area of the two-dimensional model. The model was able to recreate Weibull distributions of fracture strain in a two dimensional tensile test using a Weibull modulus of 10, but was less accurate with lower Weibull moduli.

The effect of Weibull distributions on radial crack numbers in in-service UO_2 nuclear fuel pellets was investigated. It was found that using a Weibull distribution of fracture strains in a peridynamics model of fuel pellets allows the model to more accurately predict the number of cracks expected at a given power. The model was compared to low-burnup post irradiation examination data.

Acknowledgements

Thanks are due to my supervisor at Imperial College, Dr. Mark Wenman, and to Dr. Thomas Haynes, whose technical (and moral) support was vital in the completion of this thesis, and the work upon which it is based.

I should also thank the National Nuclear Laboratory for their funding, and Glyn Rossiter for his supervision on their behalf. I was fortunate to have such an understanding and helpful industrial sponsor.

Thank you to my friend Joanna, for reminding me to keep putting one foot in front of the other.

I'd also like to thank my family: my mum, Tracy; my dad, Dave; and my sister, Carys. Thank you all for supporting and inspiring me throughout this.

Most of all, I need to thank my partner, Ellen, without whom I wouldn't have had the strength to start this journey, much less finish it. I'll never be able to pay you back for the support you've given me over these years (and I know you'll insist I don't have to) but I'm going to try my best anyway.

Contents

List of Figures

List of Tables

Chapter 1 Introduction

1.1 Nuclear Power Generation

1.1.1 Nuclear Fission

An atom is composed of negatively charged electrons orbiting a nucleus, which in turn is made up of positively charged protons and uncharged neutrons. An element is composed of atoms of the same type, and is defined by its atomic number: the number of protons in the nucleus of its atoms. It is possible for atoms with the same atomic number (i.e. of the same element) to contain different numbers of neutrons, and therefore have different mass numbers (the total number of protons and neutrons – or nucleons – in the nucleus of its atoms). These forms of elements are called isotopes.

The mass of any nucleus (with the exception of hydrogen) is less than that of its constituent nucleons. This additional mass has its origins in the energy required to overcome the Coulombic repulsion of the nucleus' protons, and is a measure of the nuclear binding energy holding the nucleus together. The binding energy may be calculated using Einstein's mass-energy relation $E = mc^2$, where E is the binding energy of the nucleus, m is mass, and c is equal to ~299,792,458 ms^{-1}, the speed of light. The specific binding energy of a nucleon varies with the mass and make-up of a nucleus (see Figure 1-1).

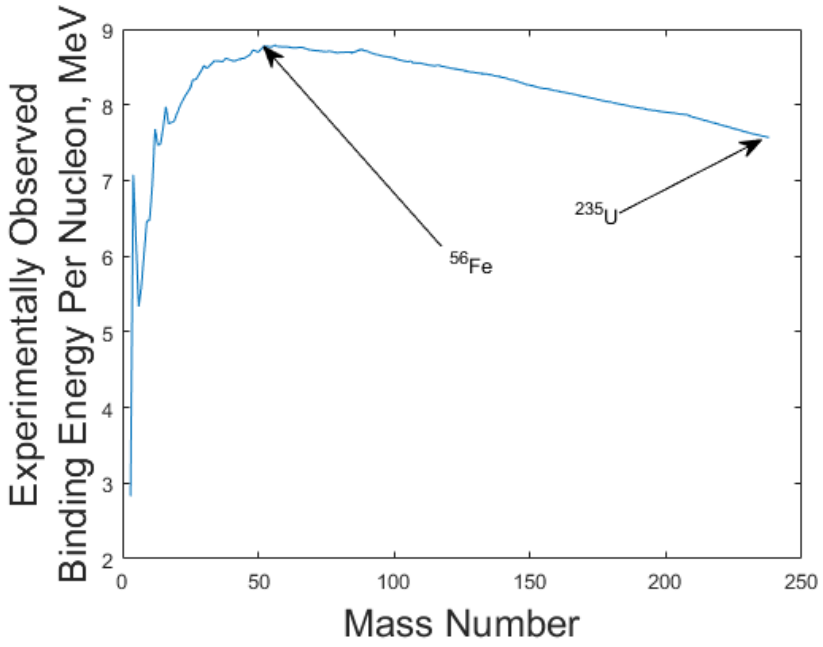

Figure 1-1 Binding energy per nucleon as a function of mass number, annotated with ^{56}Fe, the nucleus with the largest binding energy per nucleon, and ^{235}U, the nucleus most commonly used for producing fission energy in commercial nuclear power plants. Data from [1]

There are two ways in which the variation in specific binding energy of nuclei can be practically used to extract energy: fusion and fission. Nuclear fusion is the act of fusing two nuclei together, while nuclear fission is the act of splitting apart two nuclei. The resulting nucleus (fusion) / nuclei (fission) now has / have a different total mass than the original nuclei (fusion) / nucleus (fission), meaning either a release or absorption of energy must take place. Since processes tend to happen in an energetically favourable manner, it is more typical to see fusion of light atoms, and fission of heavy atoms, such that energy is released. Fusion exists in nature in an energy releasing form, as the process that powers stars. Knowing that the energy released in either a fission or fusion reaction is proportional to the mass change between the initial and final nucleon arrangements, it is clear to see that fusion, on a per nucleus basis, has much greater potential to produce energy than fission. The conditions that allow fusion to

take place in stars are difficult to mimic, however, so commercial nuclear power plants have only ever been powered by fission.

An example of an energetically favourable fission event can be seen in the splitting of ^{235}U into two nuclei with atomic number, A = 117 and A = 118. The binding energy per nucleon of the original nucleus would be around 7.6 MeV per nucleon, and the binding energy per nucleon of the 2 products would be close to 8.5 MeV per nucleon. The binding energy decrease is around $(238 \times \text{-}7.6)\text{-}(2 \times 119 \times \text{-}8.5) \cong 214$ MeV and, in order to comply with the law of conservation of energy, this amount must be emitted. This can come in a variety of forms such as neutrons, or β and γ emissions, but the majority of the energy is emitted as kinetic energy of the fragments (i.e. the fission product nuclei) [2].

Uranium metal is found naturally in uranium ore, such as uraninite, since it has a tendency to react with oxygen and nitrogen, even at room temperature. Having been mined, it is refined into "yellowcake" (primarily U_3O_8) before enrichment can take place. The majority (99.27%) of natural uranium is ^{238}U, which is not fissile. Only around 0.72% is ^{235}U, which constitutes the fissile material in nuclear fuel, and the yellowcake must therefore in general be processed to increase the proportion of ^{235}U to around 3-5% in order to make the fuel more reactive (one exception is for MAGNOX reactor fuel, where natural uranium is used: see section 1.1.3). This enrichment process involves converting the yellowcake to uranium hexafluoride (UF_6) gas and then gradually increasing the concentration of ^{235}U (relative to that of ^{238}U) in a series of gas centrifuges. The resulting enriched UF_6 is the feed product for fuel manufacture .

^{235}U is the only naturally occurring fissile material, and is therefore the obvious option for nuclear fuel, having at one stage been the only option. Under neutron irradiation some ^{238}U will absorb neutrons and transmute into ^{239}Pu, another fissile isotope, and this will contribute to the reactivity of the fuel. This process is termed "breeding" fissile isotopes. It is possible to make further use of the plutonium in waste fuel by reprocessing (which has been done in the UK (36) and France (37), as well as in other countries to a lesser extent (38)), extracting the plutonium, and reusing it in-reactor, which has been done in over 40 reactors world-wide, saving over 1000 tonnes of natural uranium (39). The corresponding fuel is termed mixed-oxide (MOX) fuel.

1.1.2 Components of a Nuclear Reactor

The key components of a nuclear reactor are:

- The Fuel
- The Fuel Cladding
- The Coolant
- The Moderator
- Neutron absorbers

This is not meant as an exhaustive list of all components of a nuclear reactor, nor is this section meant to represent a complete summary of the workings of an entire nuclear reactor. Knowledge of these five components (described in some detail in this section) is necessary to understand the workings of a nuclear reactor on a basic level, sufficient to understand the work in this thesis.

In addition to being the source of energy through fission reactions, there are other demands on fuel pellets. Primary amongst these is the need to maintain some semblance of mechanical integrity despite the multitude of degrading effects that act upon it, in order to act as the first barrier to fission product release. The fuel must resist

relocation or melting, even under the stresses arising from thermal expansion and radiation swelling, and the high thermal energy being released by the fission process. These demands require the fuel to have high thermal conductivity, specific heat capacity and melting point. Fuel fracture is more complex, as some cracking is inevitable, and resisting it may make the eventual effects worse. It is important that the fissile material remains fundamentally the same shape, and is not able to relocate to any significant extent within the cladding.

The fuel cladding acts as the second barrier to fission product release. It usually exists as a more explicit barrier, in the form of a sealed tube for the fuel to sit in, separating it from the coolant. Cladding therefore has requirements on its response to thermo-mechanical, thermo-chemical and neutronic effects. Since rupture of the cladding in a significant fraction of the fuel rods is of consequence to the plant (large-scale contamination, resulting in interruption of power generation and massive increase in decommissioning costs) it is typical to run the plant in conditions far from possible cladding rupture. This is primarily achieved by limiting maximum fuel burnup (energy produced per unit mass), fuel rod linear rating (power per unit length), coolant temperatures and cladding fast neutron fluence (the fast neutron flux through the cladding integrated over time) since the driving forces for clad failure (e.g. fuel pellet deformation) depend on burnup, linear rating and coolant temperatures, and the mechanical properties (thermal conductivity, elastic modulus, yield strength, ultimate tensile strength) of the cladding degrade with increasing neutron fluence. Cladding material must therefore have high yield stress and ductility (failure strain), and these properties must be resistant to degradation under high neutron flux conditions. An

equally important requirement for cladding is to not affect the neutron economy by absorbing neutrons which otherwise would have caused fission events. Finally, the cladding must be resistant to corrosion in the high-temperature coolant.

The energy from fission events is harvested from the fuel in the form of heat. The coolant around the fuel is heated, and the coolant is pumped around a circuit in one or more coolant loops. Heat from this coolant is used to boil water, with the resulting steam then turning a turbine, from which electricity can be generated. For light-water-cooled reactors (LWRs), the predominant reactor type worldwide, this steam can be either in the primary circuit (meaning the water evaporating is the coolant) or via a steam generator leading into a secondary circuit. One reactor design utilising a secondary circuit is the pressurised water reactor (PWR); where the primary loop is pressurised. A schematic of such a plant is shown in Figure 1-2. The use of a secondary circuit can decrease the spread of contamination throughout the turbine plant, and acts as a form of containment.

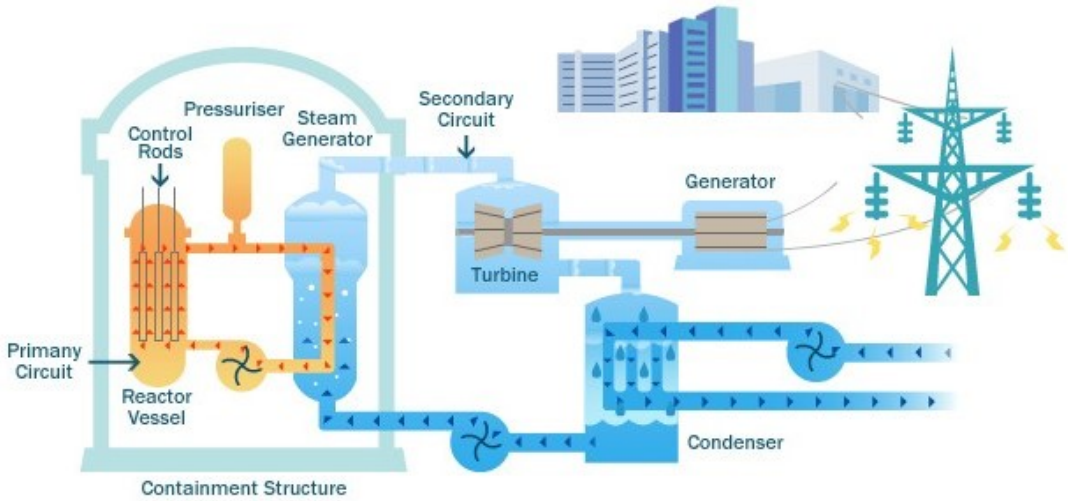

Figure 1-2 A schematic of a pressurised water reactor reproduced from [3]

The PWR is the most common reactor design globally, first operated in 1955 with the purpose of powering US Navy submarines, before being brought on land for electricity generation in 1958. PWRs tout intrinsic safety due to negative moderator temperature coefficients of reactivity (a decrease in reactivity as coolant temperatures increase) as a major benefit over other designs with separate coolant and moderator [4]. Additionally, if some small amount of boiling occurs in a PWR, moderation will be decreased, because water is less able to moderate neutrons in a gaseous state. This is known as a negative void coefficient of reactivity.

In light-water-cooled reactors, the coolant also acts as a moderator. When fission events occur and neutrons are released, they are "fast" neutrons with high energies of ~2MeV. To be usable as triggers for more fission events without the need for high fissile material content of the fuel, they must be slowed down to speeds at which the fissile material (typically ^{235}U) has a large fission cross-section (i.e. a high probability of initiating a fission event). Neutrons are slowed down by collisions with lighter atoms, in materials known as moderators, by conservation of momentum. The result is "thermal" neutrons with low energies comparable to the thermal excitation energies of the fissile material nuclei. Reactors that employ a moderator are therefore known as thermal reactors (with those that do not – which employ fast neutrons for fission with a high fissile material content – known as fast reactors). In thermal reactors cooled by fluids other than light water (e.g. helium-cooled high temperature reactors) the coolant and moderator are separate. In the case of the Advanced Gas-Cooled Reactor (AGR), the primary reactor type currently used in the UK, the coolant is carbon dioxide gas and the moderator is in the form of graphite surrounding the fuel.

In order to control the neutron economy (and therefore the reactor reactivity), a neutron-absorbing material is placed in the reactor, usually in the form of steel-clad rods containing pellets of the absorbing material, entering from above in the case of PWRs. As well as acting as a routine control device, these control rods are also a major safety component, and can be used in an emergency to shutdown the reactor. For this reason, there are typically separate banks of control rods for routine control of reactivity and for emergency shutdown. In addition to control rods, burnable poisons can be used to control reactivity. Unlike the neutron-absorbing material in control rods, which depletes, or 'burns', only gradually with time, the neutron-absorbing material in burnable poisons depletes rapidly with time. In PWRs, the burnable poisons can be in the form of rods that are inserted into the guide tubes of the fuel assemblies, or can be incorporated into the fuel pellets. Burnable poisons allow fuel to be designed with excess reactivity at beginning-of-life, with fissile material depletion due to fuel burnup being compensated for by reduction in burnable poison concentration. This permits higher fuel loading with less complex control rod systems [5]. Most commonly, boron and gadolinium are used as burnable poisons [6], [7].

1.1.3 Nuclear Power in the UK: Past, Present and Future

Following the Second World War, the United Kingdom decided to develop its own nuclear weapons programme. Having been involved with the Manhattan project during the war, a relatively large knowledge base existed in the country. In fact the MAUD report, originating in the UK, is described as "the most influential study on the feasibility of the atomic bomb" [8] Very little physical infrastructure was in place though, since much of the work had taken place in the US, who had now effectively

barred the international transfer of any nuclear knowledge. In order to generate weapons-grade nuclear material, the Windscale piles were commissioned, and became operational in 1950 [9].

The Windscale piles were large, air-cooled, graphite-moderated reactors. In order for air to be safely passed over the fuel for cooling without radioactive release, two barriers were used. The metallic uranium fuel was coated in an aluminium cladding, and there was a filter at the top of the cooling chimney. The piles were in operation until a fire in 1957, which caused a significant radioisotope release into the surrounding area. The fire originated from a build-up and subsequent release of Wigner energy in the graphite moderator [10].

Around this time, the first MAGNOX reactor at Calder Hall was completed and connected to the grid. MAGNOX reactors, named for the magnesium "non-oxidising" alloy fuel cladding [11], were CO_2-cooled reactors fuelled by natural uranium rods. In the initial design process, they served the dual purpose of producing plutonium (either for weapons or a future fast reactor fleet) and generating electricity. Calder Hall operated primarily as a commercial power plant from 1964, but only officially ceased production of plutonium for weapons purposes in 1995 [12]. MAGNOX reactors continued to be built in the UK until Wylfa in 1971, and were exported to Italy and Japan in 1963 and 1966 respectively [13]. The last MAGNOX plant operating in the UK was Wylfa A, which was permanently shut down in 2015 [14].

The second generation of nuclear reactors in the UK was made up of advanced gas-cooled reactors (AGRs). This was unusual compared to other nations, where water-

cooled reactors made up the majority of new-build reactors at this time. The AGR was designed to match conventional coal-fired power stations in terms of steam conditions, allowing for the use of the same turbo-generation plant. As opposed to the metallic uranium fuel with natural uranium isotopic mix (~0.7% ^{235}U) used in MAGNOX reactors, AGR fuel pellets are uranium dioxide, with the uranium enriched to around 3-5% ^{235}U [15]. This allowed the AGRs to be operated at higher temperatures than both the MAGNOX reactors that preceded them and the water-cooled reactors of the same generation, allowing for higher thermal efficiency.

Construction started on the last AGRs (Torness and Heysham 2) in 1980, by which time there was a desire to move away from the reactor design to a PWR design more in line with the global nuclear industry. The Sizewell B PWR, having been initially announced as an AGR, eventually started construction in 1988 [16].

There followed a gap of almost 30 years before the next nuclear power station, Hinkley Point C, also a PWR, would begin construction. This gap can be attributed to a number of causes, including relatively low prices of fossil fuel power generation; several high profile nuclear accidents causing a downturn in public opinion of nuclear power; and the privatisation of energy generation in the UK, along with a general disinclination of government to involve itself in large scale infrastructure projects in the latter part of the 20th century [17]. Projecting the fortunes of the nuclear industry has never been easy. In 1981, the UK government envisaged ordering one nuclear reactor per year for a decade [18]. Just one reactor, Sizewell B, started construction in that decade. The Chernobyl disaster, coming in 1986, certainly contributed to this reduction in scope. The UK would not start construction on another reactor until Hinkley Point C, in 2018.

This reflected a global trend in which nuclear power production has remained fairly constant in the 20th century, varying by less than 10% [19].

There are plans for more new-build nuclear plants in the UK, but it is clear that the old adage “The best laid plans of mice and men oft go awry” is as true in the nuclear industry as anywhere. In other industries, safety and cost are often separate considerations. In civil nuclear power generation, safety is such a paramount consideration that they may be considered directly and proportionately linked. Making a component safer may allow for it to be used for longer, meaning savings can be made by replacing it less frequently. Making a process cheaper may allow for greater spending on redundancy, increasing safety.

There are three major ways in which the nuclear industry is attempting to increase cost efficiency: reducing construction costs; extending the life of reactors; and reducing operation costs per unit of electricity produced. Although a significant reduction in operation or construction costs is unlikely, there is some promise in the idea of altering the funding structure of nuclear new build to reduce the cost of finance and the risk of building new nuclear plants. By building smaller reactors, often termed small modular reactors (SMRs), the lead time in plant construction and the total finance costs may be reduced [20], [21]. Any losses in economy of scale (i.e. savings and efficiencies gained by building larger plants) may be recouped by economies of volume (i.e. savings gained by building similar plants repeatedly) were the plants to be mass produced [22]–[25].

Life extension of nuclear power plants is an established practice, and mostly revolves around the reactor pressure vessel as the critical component [26]–[28]. Further advances in understanding of processes such as radiation-induced embrittlement could buy time for the next generation of nuclear power plants by extending the life of the current generation [27]. Nuclear power plants could be made to produce more energy by reducing inefficiencies around power ramping. When power needs to be increased (following a refuel, or less often, for load following) there are limits on the time over which this is done [29]. Rapid increase in power leads to high stresses in the fuel cladding which can potentially cause failure by yielding, or, more likely, stress-corrosion cracking [30]. Since these high stresses are driven by pellet-clad interaction, (see Section 1.1.4.1) and are concentrated over fuel pellet cracks, [30] a better understanding of the fuel pellet fracture process could allow for improved safety and less stringent regulations around power ramping.

Operational costs are more difficult to achieve savings in. The cost of fuel is difficult to influence, and operation and maintenance of the plant is typically not a large portion of costs. One significant way to improve the profitability of a running plant is to increase capacity factor, the amount of power the plant is outputting as a percentage of its maximum. Since many of the costs (e.g. finance, safety maintenance, decommissioning) of the plant are incurred regardless of the operational status of the plant, time with no (or low) power output can be extremely costly [31].

1.1.4 Fuel Types

Uranium can be used as a fuel in metallic form, including in MAGNOX reactors (see Chapter 1.1.3) and some fast reactor designs (e.g. U-Zr fuel in EBR-II). Various other

‘exotic’ uranium materials, including the intermetallics uranium aluminide and uranium silicide (dispersed within aluminium) and uranium hydride (mixed with zirconium hydride), have been, or are, used as research reactor fuels (generally in plate form).

Molten plutonium fuel has been tested in experimental reactors, but proved to be impractical [32]. Other liquid fuels include molten salt fuels, which take the form of nuclear fuel dissolved within a molten salt coolant. As a relatively immature technology, the engineering challenges with molten salt fuels are numerous, chief among which is the risk of corrosion [33], [34]. The redox state of the fuel-salt mixture must be closely managed in order to avoid corrosion of the coolant circuit. There is considerable desire to pursue the development of molten salt fuels though, due to two significant purported advantages of liquid fuels. Liquid fuel reactors are purportedly intrinsically safe, in that the possibility of a reactor meltdown-type accident is eliminated, and salt expansion produces a negative temperature coefficient of reactivity. This raises the possibility of significant load-following, and at the expense of the lack of cladding as a fission product barrier. There is also the possibility to periodically vent fission gasses from liquid fuels (although containment of the vented radioisotopes, at least temporarily, is then required). This is particularly useful for xenon gas, which acts as a neutron absorber.

The vast majority of nuclear fuel currently in service and of that which will be deployed in new reactors over the coming decades is in the form of ceramic pellets. Uranium nitride (UN) and uranium carbide (UC) pellets have been used in some fast reactors, but uranium dioxide (UO_2) pellets are by far the most common choice. UO_2

has become so ubiquitous as a nuclear fuel thanks in large part to its high melting temperature of around 3000 K [35]–[38], and its propensity to accommodate fission products within its lattice. For water-cooled reactors, its good compatibility with water is also important in the event of cladding failure. In the advanced gas-cooled reactors (AGRs) utilised in the UK, the UO_2 pellets are annular, roughly 15 mm in diameter and height, with a central bore of roughly 6 mm diameter to help accommodate swelling and fission gas release [39] and reduce the temperature difference between the hottest (usually the centre) and coldest (the surface) parts of the pellet [40]. The PWR fuel pellets used more frequently around the world – and in designs likely to be deployed in the UK in the foreseeable future – are roughly 8 mm in diameter, and usually have no central bore. Just as the AGR pellets' manufactured shape is informed by the dimensional changes that occur in service, so is that of the PWR pellets. The pellet end faces are chamfered, both to prevent chipping during fuel manufacture and reduce the concentration of stress in the clad at the pellet ends caused by contact with the pellets. More analogous to the central bore of the AGR pellet is dishing, meaning small depressions in the end faces, deeper in the centre than at the surface [40], to accommodate differential thermal expansion across the fuel radius.

The typical arrangement of fuel pellets in a PWR (see Figure 1-3) is a ~4 m long Zr alloy tube filled with stacked pellets, termed a rod or pin. At the top, and sometimes also bottom, of a PWR pin is a plenum volume to accommodate fission gases and dimensional changes of the pellets. An upper plenum contains a spring to hold down the pellet stack to prevent damage during transport and handling. The pins are arranged in a square lattice held together by grids and a top and bottom nozzle.

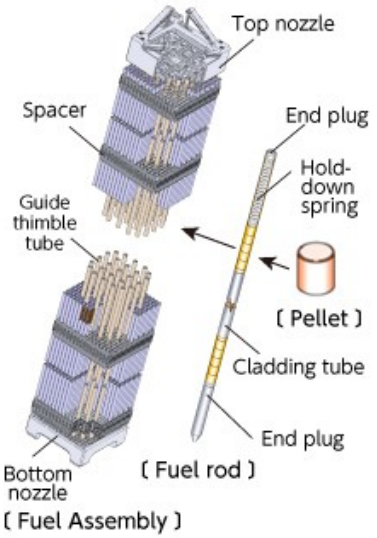

Figure 1-3 A schematic of a PWR fuel assembly. Reproduced from [41].

Two of the major disadvantages of UO_2 fuel are its low thermal conductivity (approximately 4 W m^{-1} K^{-1} [42]) and tendency to fracture in a brittle manner, which combine to produce cracks in the fuel pellets from the time at which the fuel is first brought to power in the reactor. Since the thermal conductivity is low, large temperature gradients arise between the centre and the surface of the pellets. This can be alleviated by either removing the centre of the pellet (producing annular pellets), or by preferentially enriching the surface of the pellets, such that they are more reactive and therefore hotter [42]. However, the expense of doing this (and the loss of fissile material in the case of the former) means that these approaches are not followed in practice.

During service, the tendency is for the thermal conductivity to decrease as burnup increases due to the accumulation of fission products; at high burnup, thermal conductivity is reduced further due to the formation of high-burnup (HBS) structure near the pellet surface which has a high volume fraction of pores [42]. HBS was observed and named by Lassman [43] who noted that microstructural changes at high

burnups had been noted as far back as 1962 [44] [bleiberg et al]. In this case, “high burnup” is defined as in the range of 60-75 GW d/t U, with the lower end of that range denoting the onset of HBS and the upper corresponding with fully developed HBS. Given local burnup is the parameter of most interest, it follows logically that HBS would be most prevalent around the outside surface of the pellet, and it is in fact sometimes termed “rim effect”. HBS is characterised by Lassman et al. as significant decrease in grain size, and a development of subgrain microstructure transforming each original grain into ~10,000 new grains. These fine grains contain a lower dislocation density and much lower density of intergranular fission gas bubbles [45]Fission gas pores with diameter of 1-2 μm and density increasing with local burnup are also found [43]. Additionally, Xe was found to be released from the matrix into fission gas pores {4-12, lassman}.

A more recent review [46] of HBS discusses aspects of HBR including fission gas release, mechanical interaction between pellet and cladding, and thermal conductivity. Increased fission gas release would be a highly deleterious side-effect of HBS, but it is thought that almost all locally generated fission gas is retained in the HBS porosity [47]–[49]. Microhardness measurements by Vickers indentation showed that HBS material is both softer and tougher than original material, which offers significant benefits when considering the mechanical interaction between pellet and clad, as the mechanical stress imparted on the clad will be less as a result [50]. Although thermal conductivity is generally observed to decrease with increasing burnup, it was noted that formation of HBS can in fact correspond with a slight increase in thermal conductivity [51]. The mechanism for this increase is believed to be associated with

the removal of fission gas atoms from the lattice and the reduction in defect concentration [51].

Between the rim zone (where HBS tends to occur) and the central zone, is an intermediate zone. This region is generally referred to as the ‘dark zone’ and can contain several sub-regions with variable bubble concentrations [52].Significant proportions of fission gas are believed to be contained within the dark zone. In addition to making the area prone to fine fragmentation fission gas bubbles alter the macro-scale material properties of the fuel, notably reducing the thermal conductivity, and increasing thermal gradients.

Degradation of thermal conductivity at high burnup increases the radial temperature gradients in the pellet, and the propensity for pellets to fracture. Pellet fracture alone does not pose a safety issue: the issue is in its effects on the interaction of the pellets with the cladding.

1.1.4.1 Pellet-Clad Interaction

Pellet-cladding interaction (PCI) is an umbrella term for a number of processes which can lead to failure of cladding of nuclear fuel, and is the subject of significant research. Notable reviews of this research include those by Garzarolli et al. [53], El-Adham [54], and Cox [55].

The characteristics of PCI failures are radial through-wall cladding cracks which initiate on the fuel side surface after only a moderate fuel burn-up. Usually, they follow within a few hours after a significant increase in rod power [56]. The failure mechanism is typically stress corrosion cracking (SCC), the growth of cracks under

combined influence of non-cyclic tensile stress and a reactive environment [57]. The failures occur when a fuel pellets come into hard contact with the cladding due to thermal expansion, with the cladding cracks normally forming adjacent to fuel pellet radial cracks due to the resulting stress concentration. Fission products are released into the fuel cracks, some of which can lead to embrittlement of the cladding. Iodine in particular was identified early as a cause of this embrittlement [58], [59] and investigations of its role are ongoing [60]–[62]. The PCI process is illustrated in schematic form in Figure 1-4.

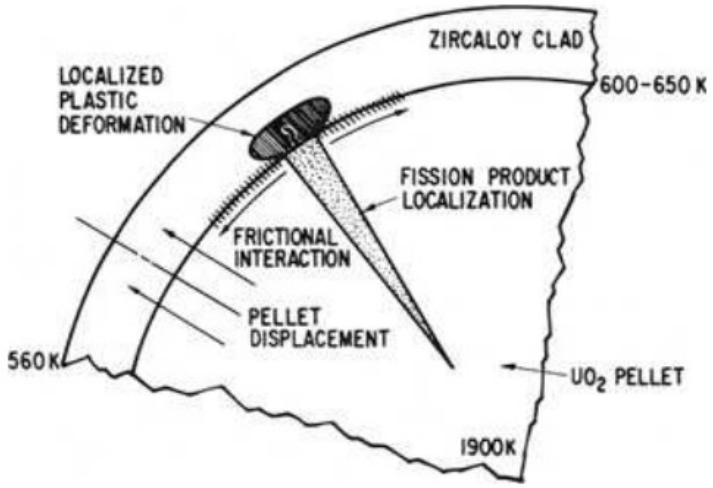

Figure 1-4 A schematic of pellet-clad interaction. Reproduced from [56]

Hydrogen is also a species of some concern with regards to cladding failure [63].Several failures of zirconium alloy cladding have been attributed to delayed hydride cracking [64]–[66]. The delayed hydride cracking mechanism involves a stress-raiser, such as a crack, where zirconium hydride precipitation occurs. Usually the precipitates are in the form of platelets. Cracking of the hydride upon a critical

condition is rapid, but there is some time between the imposition of stress and the start of cracking, during which growth of the hydride occurs.

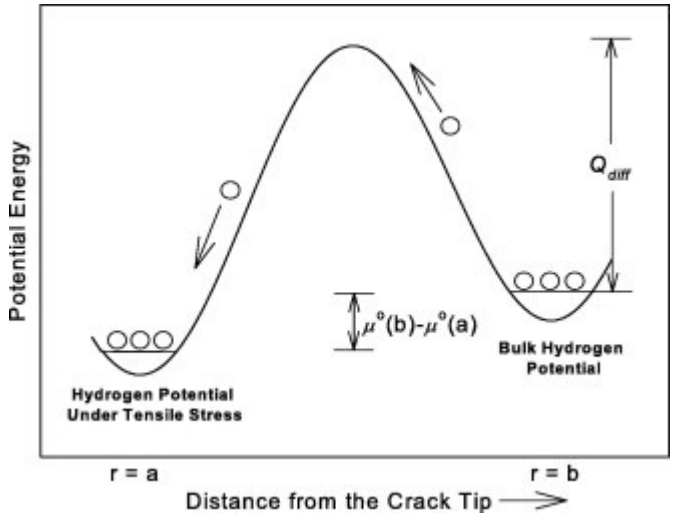

Figure 1-5: A representation of how the chemical potential changes for hydrogen under stress at a crack tip relative to the bulk. If tensile stress is applied at a crack for which the initial hydrogen concentration is the same a reproduced from [63].

Another form of interaction between pellet and clad, common in some form to LWRs [67], BWRs [68], and AGRs [69], is pellet-clad bonding. In this process hot fuel, held in high pressure contact with cladding for long periods can form a bond strong enough to induce circumferential cracking on cool-down, with the central regions reducing in size while the outer regions are held in place. The cladding then retains a 'sliver' of fuel on its inner surface, and cracking in the clad has been found to be coincident with cracking through this sliver layer though it should be stressed this is not always the case [70].

1.2 Fracture of Brittle Solids

In the framework put forward by Griffith, [71] cracking is the process of a system minimising its total energy by reducing its mechanical (i.e strain) or kinetic energy by

increasing surface energy. The system energy, U, is given as the sum of the mechanical energy, U_M, the surface energy, U_S, and the kinetic energy, U_K:

$$U = U_M + U_S + U_K \tag{1.1}$$

Griffith hypothesised cracking as a static process, and therefore

$$U_K = 0 \tag{1.2}$$

Crack growth and stopping is therefore controlled by the derivatives of mechanical energy and surface energy with respect to crack length, c. Crack growth occurs when

$$\frac{dU_M}{dc} > 0 \tag{1.3}$$

and stops when

$$\frac{dU_S}{dc} \geq 0 \tag{1.4}$$

Note that U_M and U_S are the additive inverse of each other in this case, so it is impossible for both conditions to be satisfied.

In the system proposed by Inglis [72], mechanical energy may be calculated according to crack length c, stress σ_A, and elastic modulus E:

$$U_M = \frac{\pi c^2 \sigma_A^2}{E} \tag{1.5}$$

and surface energy is given by

$$U_S = 4c\gamma \tag{1.6}$$

where U_S is surface energy, c is crack length and γ is the energy required to break atomic bonds per unit length of the crack.

Substituting (1.2), (1.5) and (1.6) into (1.1) yields

$$U = \frac{\pi c^2 \sigma_A^2}{E} + 4c\gamma. \tag{1.7}$$

The critical stress where crack growth begins must occur when $\frac{dU}{dc} = 0$ since this the point at which $\frac{dU}{dc}$ changes from positive (crack growth would absorb energy) to negative (crack growth would release energy). In the equilibrium condition where the crack length is equal to the critical crack length, c_0, the fracture stress, σ_f, may be calculated as

$$\frac{dU}{dc} = 0 \Rightarrow \sigma_f = \sqrt{\frac{2E\gamma}{\pi c_0}} \tag{1.8}$$

Theoretical strength of a material is often approximated as [73], [74]

$$\sigma_f \approx \sqrt{\frac{E}{2\pi}} \tag{1.9}$$

Two things are notable from comparison of the real strength of brittle materials, compared to the theoretical strength. Firstly, the real strength is far lower than the theoretical strength, and secondly, the strength of a ceramic object is determined by the size of its critical flaw as much as by any inherent property of the material.

During processing of ceramic materials small, microscopic flaws and cracks are introduced into both the surface and the bulk of the product. In objects of any significant scale, this is virtually unavoidable, although small fibres may be produced for composite materials with very small concentrations of such flaws. Imperfections exist in ductile materials too, but the ability of the material to plastically deform allows for these flaws/defects to be blunted, reducing the stress concentration they produce. In brittle materials, this yield process does not occur, and stress increases until it is sufficient to cause fracture.

Given that the strength of brittle materials is dependent on the size of their critical flaws, and that the size of their critical flaws is a variable that cannot practically be controlled in most components, it follows that the fracture strength of brittle materials is variable. Modelling this variability in a mechanistic sense would be difficult in itself, and would then require that each component's processing route be examined to determine the length of any flaws that may have been imparted into it. Instead, the cause of the variability may be ignored, and an empirical fit may be made to describe the results.

1.2.1 Weibull Distributions

In 1951 Waloddi Weibull formulated "A Statistical Distribution Function of Wide Applicability" [75] which is now known as the Weibull distribution, a common empirically fitted probability distribution for lifetime analysis of brittle materials. As the title suggests though, this is far from the only application of the distribution. In an appendix to the original paper, Weibull lists "Statures for adult males, born in the

British Isles" and "Breadth of beans of Phaseolus Vulgaris" as variables to which the Weibull distribution may be fitted.

Although the Weibull distribution does not have a firm theoretical grounding in fracture theory, it does have a basis in an analogy to fracture. Weibull considered a chain, made of n links, and postulated that the probability of survival P_s at a given force X on that chain is equal to the probability that all n links are able to survive force X:

$$P_s = \left(1 - P_f(X)\right).\left(1 - P_f(X)\right)...\left(1 - P_f(X)\right) = \left(1 - P_f(X)\right)^n \qquad (1.10)$$

The probability that a given link has a failure load smaller than or equal to x is given by

$$F(x) = P(X \leq x) \qquad (1.11)$$

This can be written, without loss of generality, as

$$F(x) = 1 - e^{-\varphi(x)} \qquad (1.12)$$

Combining (1.10) with (1.12) yields

$$P_s = \left(1 - F(x)\right)^n = e^{-n\varphi(x)} \qquad (1.13)$$

And given that

$$P_f = 1 - P_s \tag{1.14}$$

we can put the equation in terms of the probability of failure of the whole chain as

$$P_f = 1 - e^{-n\varphi(x)} \tag{1.15}$$

The function *φ(x)* must then be determined. The conditions upon it are that the probability must be equal to zero at some value for *x*, either *x* = 0 or otherwise; and it must be a positive non-decreasing function. These conditions allow for a distribution in which probability of failure increases with increasing load, and probability of failure being non-zero at negative loads is impossible.

The simplest function that satisfies these conditions for the variable *x* is

$$\varphi(x) = \left(\frac{x - x_u}{x_0}\right)^{\beta} \tag{1.16}$$

where x_u is the value for *x* at which $\varphi(x)$ is equal to zero, which may be set to zero to form the two-parameter Weibull distribution, x_0 is the characteristic value of the variable *x* for which $\varphi(x) \approx 63\%$ and β is the Weibull modulus, which controls the gradient of the distribution.

So

$$F(x) = 1 - e^{-\left(\frac{x - x_u}{x_0}\right)^{\beta}} \tag{1.17}$$

And for a chain:

$$P_f = 1 - e^{-n\left(\frac{x-x_u}{x_0}\right)^{\beta}} \tag{1.18}$$

The analogy of the chain allows the Weibull distribution to be particularly useful in cases where several probabilities are combined, in a manner such that failure in one case means failure overall. For example, a machine may have many components, each with a low likelihood of failure during operation. Failure of a single component would mean failure of the machine though, meaning the components must be assessed holistically, and Weibull analysis allows this.

In materials engineering, the Weibull distribution is used as an analogue for defect populations leading to fracture. It would be impractical to examine every component to ascertain the size and orientation of every defect, then determine, based on the expected stresses in service, whether the given component is sufficiently strong. It is possible though, to test many components, in the correct loading state, and determine the probability of failure for a component, given a certain material, geometry and load.

This testing is informed by the chain analogy in Weibull's original formulation. Even if, in service, the component is very large (i.e a long chain) testing may be conducted on smaller components (i.e. the links of that chain) and predictions can reliably be made about the larger component.

1.2.1.1 Size Scaling

The randomness of fracture strengths described by Weibull distributions stems from the random size and orientation of the critical flaw within specimens of the material. Since larger specimens have more volume in which to contain a large flaw, the probability of containing such a flaw is higher, and their fracture strength is, on

average, lower. The manner of this decrease in strength can be described in the manner of a chain, where the probability of failure of each link $P_{link,F}$ for a given stress σ is known, and given by

$$P_{link,F} = 1 - exp\left(-\left[\frac{\sigma}{\sigma_{0,link}}\right]^{\beta}\right) \tag{1.19}$$

where $\sigma_{0,link}$ is the characteristic stress of a single link, and β is the Weibull modulus. The probability that an object will fail, P_F, is related to the probability that it will survive, P_S, by (1.20).

$$P_S = 1 - P_F \tag{1.20}$$

The probability that a single link in the chain will survive, $P_{link,S}$, is found by substituting (1.19) into (1.20) to give (1.21):

$$P_{link,S} = 1 - \left[1 - e^{-\left(\sigma/\sigma_{link,0}\right)^{\beta}}\right] = e^{-\left(\sigma/\sigma_{link,0}\right)^{\beta}} \tag{1.21}$$

A chain of N such links will only survive if all of the N links in the chain survive. The probability that the chain survives, $P_{chain,S}$, is therefore given by (1.22):

$$P_{chain,S} = \left(P_{link,S}\right)^{N} \tag{1.22}$$

Substituting (1.21) into (1.22) gives

$$P_{chain,S} = \left(e^{-\left(\sigma/\sigma_{link,0}\right)^{\beta}}\right)^{N} = e^{-N\left(\sigma/\sigma_{link,0}\right)^{\beta}} \tag{1.23}$$

Using (1.20) and (1.23) gives the probability that the chain will fail, $P_{chain,F}$:

$$P_{chain,F} = 1 - e^{-N\left(\sigma/\sigma_{link,0}\right)^{\beta}} \tag{1.24}$$

Requiring that the probability of the failure of the chain will take the same functional form as (1.24) and making the assumption that the Weibull modulus is an extrinsic material property and therefore invariant, gives (1.25):

$$P_{chain,F} = 1 - e^{-\left(\sigma/\sigma_{chain,0}\right)^{\beta}} \tag{1.25}$$

where $\sigma_{chain,0}$ is the characteristic stress of the chain. Comparing (1.24) and (1.25) and equating the exponents enables $\sigma_{chain,0}$ to be determined as follows:

$$\sigma/\sigma_{chain,0} = N^{(1/\beta)}\sigma/\sigma_{link,0}$$

$$\sigma_{chain,0} = \frac{\sigma_{link,0}}{N^{(1/\beta)}} = \left(\frac{1}{N}\right)^{1/\beta}\sigma_{link,0} \tag{1.26}$$

Materials do not in actuality consist of long chains of individual elements, but N may be considered the ratio of the number of links in the initial scenario described in (1.19)(i.e. 1) and the eventual chain of N links. Now a different ratio can be used, the ratio of the volume of a sample V_{sample} to the reference volume V_{ref} for which the Weibull parameters are known:

$$N = \frac{V_{sample}}{V_{ref}} \tag{1.27}$$

In the simplest case, the component is uniformly loaded, and defects anywhere within the volume can nucleate large cracks. In this case, the scaling is simply dependent on the difference between the sample volume and the reference volume. Where stress profiles are more complex, it is necessary to determine the effective volume of the component [76].

1.3 References

[1] N. Ghahramany, S. Gharaati, and M. Ghanaatian, "New approach to nuclear binding energy in integrated nuclear model," *J. Theor. Appl. Phys.*, vol. 6, no. 1, p. 3, Jul. 2012, doi: 10.1186/2251-7235-6-3.

[2] K. S. Krane, *Introductory Nuclear Physics*. 1987.

[3] "Pressurised Water Reactor VS Boiling Water Reactor | Nuclear Energy | CLP Group." https://www.clpgroup.com/NuclearEnergy/Eng/power/power4_1_2.aspx (accessed Aug. 26, 2020).

[4] M. Ho, E. Obbard, P. A. Burr, and G. Yeoh, "A review on the development of nuclear power reactors," *Energy Procedia*, vol. 160, pp. 459–466, Feb. 2019, doi: 10.1016/j.egypro.2019.02.193.

[5] J. A. Renier, "Development of Improved Burnable Poisons for Commercial Nuclear Power Reactors," ORNL Oak Ridge National Laboratory (US), ORNL/TM-2001/238, Apr. 2002. doi: https://doi.org/10.2172/814398.

[6] H. Guo, P. Sciora, T. Kooyman, L. Buiron, and G. Rimpault, "Application of Boron Carbide as Burnable Poison in Sodium Fast Reactors," *Nucl. Technol.*, vol. 205, no. 11, pp. 1433–1446, Nov. 2019, doi: 10.1080/00295450.2019.1620054.

[7] L. Goldstein and A. A. Strasser, "A Comparison of Gadolinia and Boron for Burnable Poison Applications in Pressurized Water Reactors," *Nucl. Technol.*, vol. 60, no. 3, pp. 352–361, Mar. 1983, doi: 10.13182/NT83-A33122.

[8] "Manhattan Project: The Maud Report, 1941." https://www.osti.gov/opennet/manhattan-project-history/Events/1939-1942/maud.htm (accessed Jul. 03, 2022).

[9] A. D. Smith, S. R. Jones, J. Gray, and K. A. Mitchell, "A review of irradiated fuel particle releases from the Windscale Piles, 1950–1957," *J. Radiol. Prot.*, vol. 27, no. 2, pp. 115–145, May 2007, doi: 10.1088/0952-4746/27/2/001.

[10] R. Wakeford, "The Windscale reactor accident—50 years on," *J. Radiol. Prot.*, vol. 27, no. 3, pp. 211–215, Aug. 2007, doi: 10.1088/0952-4746/27/3/E02.

[11] S. E. Jensen and E. Nonboel, "Description of the magnox type of gas cooled reactor (MAGNOX)," Nordisk Kernesikkerhedsforskning, NKS--2, 1999. Accessed: Sep. 02, 2020. [Online]. Available: http://inis.iaea.org/Search/search.aspx?orig_q=RN:30052480

[12] "Plutonium and Aldermaston: A historical Account," UK Ministry of Defence, Aldermaston, 2000.

[13] R. Boardman and M. Grieve, "The Politics of Fading Dreams: Britain and the Nuclear Export Business," in *Nuclear Exports and World Politics: Policy and Regime*, R. Boardman and J. F. Keeley, Eds. London: Palgrave Macmillan UK, 1983, pp. 98–119. doi: 10.1007/978-1-349-05984-3_6.

[14] "Nuclear Development in the United Kingdom |UK Nuclear Energy Development - World Nuclear Association." https://www.world-nuclear.org/information-library/country-profiles/countries-t-z/appendices/nuclear-development-in-the-united-kingdom.aspx (accessed Apr. 08, 2021).

[15] "Fact sheet: uranium enrichment and fuel manufacture," *UK NDA*, Accessed: Feb. 02, 2021. [Online]. Available: https://ukinventory.nda.gov.uk/wp-

content/uploads/2014/01/Fact-sheet-uranium-enrichment-and-fuel-manufacture.pdf
[16] “World Nuclear Association Sizewell B Dashboard.” https://www.world-nuclear.org/reactor/default.aspx/SIZEWELL%20B (accessed Feb. 28, 2021).
[17] M. Pisu, B. Pels, and N. Bottini, “Improving infrastructure in the United Kingdom,” Jul. 2015, doi: https://doi.org/10.1787/5jrxqbqc7m0p-en.
[18] F. Tombs, “Nuclear energy - past present and future,” *Electron. Power*, vol. 27, no. 4, pp. 283–284, Apr. 1981, doi: 10.1049/ep.1981.0137.
[19] “Reactor Database Global Dashboard - World Nuclear Association.” https://www.world-nuclear.org/information-library/facts-and-figures/reactor-database.aspx (accessed Aug. 26, 2020).
[20] B. Mignacca and G. Locatelli, “Economics and finance of Small Modular Reactors: A systematic review and research agenda,” *Renew. Sustain. Energy Rev.*, vol. 118, p. 109519, Feb. 2020, doi: 10.1016/j.rser.2019.109519.
[21] M. D. Carelli *et al.*, “Economic features of integral, modular, small-to-medium size reactors,” *Prog. Nucl. Energy*, vol. 52, no. 4, pp. 403–414, May 2010, doi: 10.1016/j.pnucene.2009.09.003.
[22] A. Abdulla, I. L. Azevedo, and M. G. Morgan, “Expert assessments of the cost of light water small modular reactors,” *Proc. Natl. Acad. Sci.*, vol. 110, no. 24, pp. 9686–9691, Jun. 2013, doi: 10.1073/pnas.1300195110.
[23] S. Boarin, G. Locatelli, M. Mancini, and M. E. Ricotti, “Financial Case Studies on Small- and Medium-Size Modular Reactors,” *Nucl. Technol.*, vol. 178, no. 2, pp. 218–232, May 2012.
[24] G. Locatelli, C. Bingham, and M. Mancini, “Small modular reactors: A comprehensive overview of their economics and strategic aspects,” *Prog. Nucl. Energy*, vol. 73, pp. 75–85, May 2014, doi: 10.1016/j.pnucene.2014.01.010.
[25] J. Vujić, R. M. Bergmann, R. Škoda, and M. Miletić, “Small modular reactors: Simpler, safer, cheaper?,” *Energy*, vol. 45, no. 1, pp. 288–295, Sep. 2012, doi: 10.1016/j.energy.2012.01.078.
[26] G. R. Odette and G. E. Lucas, “Embrittlement of nuclear reactor pressure vessels,” *JOM*, vol. 53, no. 7, pp. 18–22, Jul. 2001, doi: 10.1007/s11837-001-0081-0.
[27] C. Li, L. Han, G. Yan, Q. Liu, X. Luo, and J. Gu, “Time-dependent temper embrittlement of reactor pressure vessel steel: Correlation between microstructural evolution and mechanical properties during tempering at 650 °C,” *J. Nucl. Mater.*, vol. 480, pp. 344–354, Nov. 2016, doi: 10.1016/j.jnucmat.2016.08.039.
[28] G. R. Odette, M. J. Alinger, and B. D. Wirth, “Recent Developments in Irradiation-Resistant Steels,” *Annu. Rev. Mater. Res.*, vol. 38, no. 1, pp. 471–503, 2008, doi: 10.1146/annurev.matsci.38.060407.130315.
[29] “Review of Fuel Failures in Water Cooled Reactors, Section 8,” Vienna, NF-T-2.1, 2010.
[30] G. Rossiter, “Understanding and Modelling Fuel Behaviour Under Irradiation,” in *Nuclear Fuel Science and Engineering*, 2012, pp. 396–424.
[31] “Nuclear Power Economics | Nuclear Energy Costs - World Nuclear Association.” https://www.world-nuclear.org/information-library/economic-aspects/economics-of-nuclear-power.aspx (accessed Jul. 03, 2022).

[32] J. R. Harper and R. Garde, “Decommissioning the Los Alamos Molten Plutonium Reactor Experiment (LAMPRE I),” Los Alamos National Lab., NM (USA), LA-9052-MS, Nov. 1981. doi: https://doi.org/10.2172/5617058.
[33] J. Baes, “CHEMISTRY AND THERMODYNAMICS OF MOLTEN SALT REACTOR FUELS.,” *Nucl Met Met Soc AIME 15 617-441969*, Jan. 1969, Accessed: Feb. 28, 2021. [Online]. Available: https://www.osti.gov/biblio/4774915
[34] K. Sridharan and T. R. Allen, “12 - Corrosion in Molten Salts,” in *Molten Salts Chemistry*, F. Lantelme and H. Groult, Eds. Oxford: Elsevier, 2013, pp. 241–267. doi: 10.1016/B978-0-12-398538-5.00012-3.
[35] S. W. Pijanowski and L. S. DeLuca, “Melting Points in the System PuO2-UO 2,” Knolls Atomic Power Lab., Schenectady, N.Y., KAPL-1957, Apr. 1960. Accessed: Feb. 05, 2021. [Online]. Available: https://www.osti.gov/biblio/4115231
[36] T. D. Chikalla, “The Liquidus for the System UO2-PuO 2,” General Electric Co. Hanford Atomic Products Operation, Richland, Wash., HW-69832, Jun. 1961. Accessed: Feb. 05, 2021. [Online]. Available: https://www.osti.gov/biblio/4802605
[37] H. Hausner, “Determination of the melting point of uranium dioxide,” *J. Nucl. Mater.*, vol. 15, no. 3, pp. 179–183, Jan. 1965, doi: 10.1016/0022-3115(65)90178-9.
[38] “MATPRO - A Library of Materials Properties for Light-Water-Reactor Accident Analysis,” Idaho National Engineering and Environmental Laboratory, 20555–0001. [Online]. Available: https://www.nrc.gov/docs/ML0103/ML010330363.pdf
[39] H. Hughes and R. Hargreaves, “AGR fuel pin pellet-clad interaction failure limits and activity release fractions,” Art. no. IWGGCR--8, 1985, Accessed: Feb. 05, 2021. [Online]. Available: http://inis.iaea.org/Search/search.aspx?orig_q=RN:31049627
[40] D. R. Olander, “Light Water Reactor Fuel Design and Performance,” in *Encyclopedia of Materials: Science and Technology*, K. H. J. Buschow, R. W. Cahn, M. C. Flemings, B. Ilschner, E. J. Kramer, S. Mahajan, and P. Veyssière, Eds. Oxford: Elsevier, 2001, pp. 4490–4504. doi: 10.1016/B0-08-043152-6/00787-7.
[41] “Manufacturing Process in Tokai Plant(PWR Fuel) | Mitsubishi Nuclear Fuel Co., Ltd.” http://www.mnf.co.jp/en/business/process.html (accessed Jun. 16, 2021).
[42] R. J. M. Konings, “Thermal Properties of Irradiated UO2 and MOX,” in *Comperhensive Nuclear Materials, Volume 2*, Elsevier, 2012, pp. 439–464.
[43] K. Lassmann, C. T. Walker, J. van de Laar, and F. Lindström, “Modelling the high burnup UO2 structure in LWR fuel,” *J. Nucl. Mater.*, vol. 226, no. 1, pp. 1–8, Oct. 1995, doi: 10.1016/0022-3115(95)00116-6.
[44] M. L. Bleiberg, R. M. Berman, and B. Lustman, in *roc. Symp. on Radiation Damage in Solids and Reactor Ma- terials*, IAEA, Vienna, 1963, 1963, p. 319.
[45] “INSTITUTE FOR TRANSURANIUM ELEMENTS KARLSRUHE: Annual Report 1992: TUAR-92,” p. 252.

[46] V. V. Rondinella and T. Wiss, “The high burn-up structure in nuclear fuel,” *Mater. Today*, vol. 13, no. 12, pp. 24–32, Dec. 2010, doi: 10.1016/S1369-7021(10)70221-2.
[47] J. Spino, D. Papaioannou, and J.-P. Glatz, “Comments on the threshold porosity for fission gas release in high burn-up fuels,” *J. Nucl. Mater.*, vol. 328, no. 1, pp. 67–70, Jun. 2004, doi: 10.1016/j.jnucmat.2004.03.009.
[48] J. Spino, A. D. Stalios, H. Santa Cruz, and D. Baron, “Stereological evolution of the rim structure in PWR-fuels at prolonged irradiation: Dependencies with burn-up and temperature,” *J. Nucl. Mater.*, vol. 354, no. 1, pp. 66–84, Aug. 2006, doi: 10.1016/j.jnucmat.2006.02.095.
[49] K. M, “High burnup RIM project : (III) Properties of rim-structured fuel,” *Proc 2004 Int Mtg LWR Fuel Perform. Orland Fla. USA Sep 19-22 2004*, 2004, Accessed: Jul. 03, 2022. [Online]. Available: https://cir.nii.ac.jp/crid/1571417125863458688
[50] J. Spino, J. Cobos-Sabate, and F. Rousseau, “Room-temperature microindentation behaviour of LWR-fuels, part 1: fuel microhardness,” *J. Nucl. Mater.*, vol. 322, no. 2, pp. 204–216, Nov. 2003, doi: 10.1016/S0022-3115(03)00328-3.
[51] C. Ronchi, M. Sheindlin, D. Staicu, and M. Kinoshita, “Effect of burn-up on the thermal conductivity of uranium dioxide up to 100.000 MWdt−1,” *J. Nucl. Mater.*, vol. 327, no. 1, pp. 58–76, Apr. 2004, doi: 10.1016/j.jnucmat.2004.01.018.
[52] G. L. Beausoleil and F. Cappia, “Separate Effects Testing in TREAT for ATF Fuels,” Idaho National Lab. (INL), Idaho Falls, ID (United States), INL/EXT-19-55404-Rev000, Sep. 2019. Accessed: Jul. 03, 2022. [Online]. Available: https://www.osti.gov/biblio/1607487
[53] F. Garzarolli, R. Manzel, M. Peehs, and H. Stehle, “Observations and hypotheses on pellet-clad interaction failures,” *Kerntechnik*, vol. 20, no. 1, pp. 27–31, 1978.
[54] K. El-Adham, “Fuel failure mechanisms in operating US plants from 1981 to 1986,” *J Nucl Saf.*, vol. 29, no. 4, p. 487, 1988.
[55] B. Cox, “Pellet-clad interaction (PCI) failures of zirconium alloy fuel cladding — A review,” *J. Nucl. Mater.*, vol. 172, no. 3, pp. 249–292, Aug. 1990, doi: 10.1016/0022-3115(90)90282-R.
[56] D. Tomalin, R. Adamson, and R. Gangloff, “Performance of Irradiated Copper and Zirconium Barrier-Modified Zircaloy Cladding Under Simulated Pellet-Cladding Interaction Conditions,” in *Zirconium in the Nuclear Industry*, J. Schemel and T. Papazoglou, Eds. 100 Barr Harbor Drive, PO Box C700, West Conshohocken, PA 19428-2959: ASTM International, 1979, pp. 122-122–23. doi: 10.1520/STP36676S.
[57] K. Sieradzki and R. C. Newman, “Stress-corrosion cracking,” *J. Phys. Chem. Solids*, vol. 48, no. 11, pp. 1101–1113, Jan. 1987, doi: 10.1016/0022-3697(87)90120-X.
[58] H. S. Rosenbaum, J. T. Davies, and J. Q. Pon, “Report GEAP-5100-5,” General Electric Co., 1966.
[59] H. S. Rosenbaum, “Electrochem. Tech. 4,” 1966.
[60] C. Gillen, A. Garner, C. Anghel, and P. Frankel, “Investigating iodine-induced stress corrosion cracking of zirconium alloys using quantitative fractography,” *J.*

Nucl. Mater., vol. 539, p. 152272, Oct. 2020, doi: 10.1016/j.jnucmat.2020.152272.
[61] C. Gillen *et al.*, "Advanced 3D characterisation of iodine induced stress corrosion cracks in zirconium alloys," *Mater. Charact.*, vol. 141, pp. 348–361, Jul. 2018, doi: 10.1016/j.matchar.2018.04.034.
[62] A. Kenich, M. R. Wenman, and R. W. Grimes, "Iodine defect energies and equilibria in ZrO2," *J. Nucl. Mater.*, vol. 511, pp. 390–395, Dec. 2018, doi: 10.1016/j.jnucmat.2018.09.018.
[63] G. A. McRae, C. E. Coleman, and B. W. Leitch, "The first step for delayed hydride cracking in zirconium alloys," *J. Nucl. Mater.*, vol. 396, no. 1, pp. 130–143, Jan. 2010, doi: 10.1016/j.jnucmat.2009.08.019.
[64] E. C. W. Perryman, "Pickering pressure tube cracking experience," *Nucl Energy*, vol. 17, no. 2, pp. 95–105, 1978.
[65] P. A. Platonov, A. V. Ryazantseva, G. P. Saenko, Y. N. Knizhnikov, and V. F. Viktorov, "The study of cause of cracking in zirconium alloy channel tubes," 1988.
[66] K. Edsinger, J. H. Davies, and R. B. Adamson, "Degraded Fuel Cladding Fractography and Fracture Behavior," in *Zirconium in the Nuclear Industry – Twelfth International Symposium*, 2000, pp. 316–339. Accessed: Jul. 03, 2022. [Online]. Available: https://www.astm.org/stp14306s.html
[67] G. Roberts, "The concentration of stress in cladding produced by the expansion of cracked fuel pellets," *Nucl. Eng. Des.*, vol. 47, no. 2, pp. 257–266, May 1978, doi: 10.1016/0029-5493(78)90068-7.
[68] K. Nogita and K. Une, "Formation of Pellet-Cladding Bonding Layer in High Burnup BWR Fuels," *J. Nucl. Sci. Technol.*, vol. 34, no. 7, pp. 679–686, 1997, doi: 10.3327/jnst.34.679.
[69] R. E. Pendlebury, "A 2000 hour test to investigate CAGR fuel pellet/clad bonding," Nuclear Electric, TD/SID/MEM/0274, 1992.
[70] T. A. Haynes, "Finite Element Modelling of Nuclear Fuel performance in Advanced Gas-Cooled Reactors," Imperial College London, 2018.
[71] A. A. Griffith and G. I. Taylor, "The phenomena of rupture and flow in solids," *Philos. Trans. R. Soc. Lond. Ser. Contain. Pap. Math. Phys. Character*, vol. 221, no. 582–593, pp. 163–198, Jan. 1921, doi: 10.1098/rsta.1921.0006.
[72] C. E. Inglis, "Stresses in a Plate Due to the Presence of Cracks and Sharp Corners," *SPIE Milest. Ser.*, vol. 137, pp. 3–17.
[73] T. H. Courtney, *Mechanical Behavior of Materials*. McGraw-Hill, 2000.
[74] C. T. Sun and Z.-H. Jin, *Fracture mechanics*. Waltham, MA: Academic Press, 2012. Accessed: Apr. 08, 2021. [Online]. Available: http://www.myilibrary.com?id=328817
[75] W. Weibull, "A Statistical Distribution Function of Wide Applicability," *ASME J. Appl. Mech.*, Sep. 1951.
[76] A. Bhushan *et al.*, "Weibull Effective Volumes, Surfaces, and Strength Scaling for Cylindrical Flexure Specimens Having Bi-Modularity," *J. Test. Eval.*, vol. 44, Sep. 2016, doi: 10.1520/JTE20150301.

Chapter 2 Literature Review

2.1 Pellet Fracture

Nuclear fission reactors produce energy in the form of high velocity fission products imparting their kinetic energy on their surroundings through collisions. This energy is dispersed throughout the fuel, in the form of atomic vibration, i.e. heat. This heat then flows into the coolant due to the temperature gradient, where it can later be extracted to drive a turbine and produce electricity. The fuel furthest from the coolant (i.e. the centre of the pellets) is therefore hotter (>1000°C) than the fuel closest to the coolant (i.e. the surface of the pellets at around 350-400°C for a PWR). As a PWR pellet is of order of 4 mm in radius the pellets see gradients of 200°C mm^{-1}.

Radial temperature gradients therefore drive differential thermal expansion in the fuel, with the centre expanding more than fuel near the surface [1]. This creates a tensile stress field around the pellet surface, which is being driven to expand further than it would simply due to uniform thermal expansion. Conversely, a compressive stress is applied to the pellet centre. The tensile stress at the surface becomes sufficient to cause fracture even on first reactor startup, and radial cracks grow inwards from the surface towards the pellet centre [2]–[4]. Circumferential cracks separating the central region of the pellet from the outside are believed to occur during cooling [5]. Calling cracks 'radial' or 'circumferential' is a simplification, as the direction the cracks follow is not perfectly radial or circumferential, but it is useful to split cracks into these two categories.

There is some disagreement as to the order in which radial and circumferential cracks occur. In an early simple model, Oguma [6] makes the assumption that a fracturing

pellet splits exactly in half axially, followed by the fragments then fracturing in half axially with increasing linear power rating. The model then goes on to predict that the pellet fractures in the hoop direction (producing radial cracks), before each fragment again splits in half in the same direction. Descriptions with less symmetry show one crack that penetrates through roughly the centre of the pellet, and further cracks then join (see Figure 2-1). When crack faces are in sufficiently intimate contact, and the temperature is high enough (as in a power transient) crack healing can occur. Bridges of material form between the crack faces through thermal diffusion. The effect of crack healing is to modify the final crack pattern to display an uncracked central region, with radial cracks connected by an approximately circular ring of circumferential cracks, which occur on cooldown. It is always worth remembering that even when using real crack patterns the user is only observing the final state of the crack pattern and misinterpretation of when the cracks form is a distinct possibility. Indeed this is a good reason for explicit crack modelling, which can provide insight as to the how, when and why cracks forms in nuclear fuel.

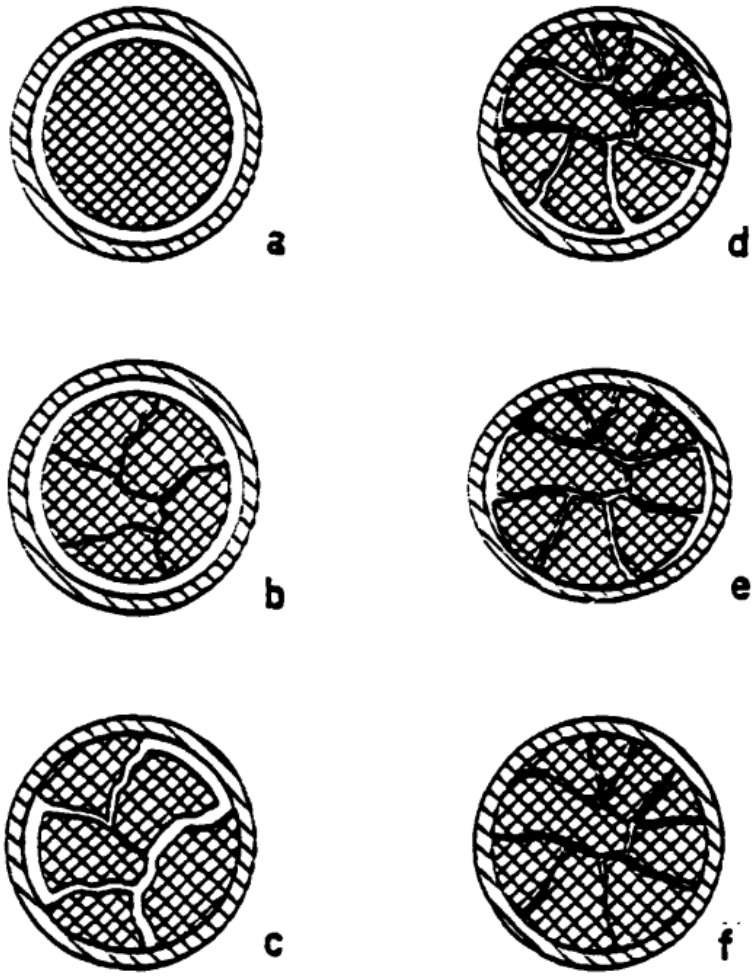

Figure 2-1 A schematic of the process of fuel pellet fracture and relocation. Reproduced from [7].

Recent modelling tends to display a different process of fracture, one where multiple radial cracks initiate and grow simultaneously, restricted by the stress field in the pellet [8]–[11]. Since the hotter regions in the centre are under compressive stress, it follows that the stress in the intermediate region must steadily decrease before inverting. Upon reaching areas of lower stress, radial crack growth becomes less favourable, and growth stops until further increases in temperature create sufficient stress for renewed growth.

Pellet fracture can lead to fragmentation, either in the first ramp up to power, or subsequently on cooling. These fragments are then somewhat free to relocate within the cladding until thermal expansion, fuel swelling and clad creep-down are sufficient to close the clad-fuel gap. Once there is contact between the clad and the fuel, the fragments start to be pushed back together. This is termed relocation accommodation. Since thermal stresses have been released in the form of strains following fracture, the fragments no longer fit together perfectly. This is a source of friction and stress on both the fuel and the clad. Upon cooldown these stresses cause circumferential pellet cracks to initiate from the radial cracks. These circumferential cracks tend to connect into a network of cracks that can act as an impediment to heat flow. Circumferential cracks can also be the result of fuel bonding to the cladding, so that when the fuel contracts, the outer region is held in place, inducing circumferential stresses sufficient to induce fracture.

A quantitative study of the number of radial cracks appearing in LWR fuel rods in various irradiation conditions was performed by Walton and Husser in 1982 [7]. Irradiated pellets were sectioned and photographed for examination to count the number of radial cracks intersecting the surface of the pellet. The irradiation conditions ranged from 1 – 35 GWd tU^{-1} and linear heat rates from below 10 to almost 70 kW m^{-1}. The widths of cracks and final pellet-clad gaps were also measured.

2.2 Pellet-Clad Interaction

Fracturing of fuel, in most cases, is not in itself a safety or economic issue. When cracks at the surface interact with fuel cladding though, there exists the possibility of cladding rupture through pellet-clad interaction (PCI). In order to avoid cladding

rupture, the operation of the plant is restricted in terms of a number of factors related to power and power ramping. This is a significant economic burden on the plant, meaning some generation capacity is lost. During accident conditions power can spike, meaning these restrictions may be involuntarily violated, creating a safety issue.

2.2.1 Causes of PCI

Operationally speaking, PCI is characterised by five factors, all associated with fuel power and ramping [12]:

- Burnup accumulated prior to the power ramp
- Maximum rod/pin power during the power ramp
- Ramp height, i.e. power increment beyond the pre-irradiated power level
- Average power ramp rate
- Dwell time at high power

Only when all five factors are in a critical range simultaneously will a PCI defect occur.

PCI is a complex set of thermal, mechanical, and chemical processes, which can potentially result in brittle fracture of fuel cladding as the result of interaction between localised cladding deformation, resulting from the motion of gaps between pellet fragments, and embrittling fission products [13]. For this reason, PCI is a major limiting factor on the operational envelope of a nuclear reactor, particularly relating to fuel burn up. PCI comes in the form of purely mechanical interactions (PCMI), as well as chemical interactions such as stress-corrosion cracking (SCC).

Cox [14] notes four factors that affect the incidence of PCI failures: sufficient stress; sufficient time; a susceptible material; and the right chemical environment.

2.2.1.1 Sufficient stress

The stress induced in the cladding by the mechanical action of the fuel is of course dictated by the geometry of the fuel, both at the start of life, and in service. The initial clearance between the pellet and cladding; the thermal expansion of the pellet, including any distortion in shape; the fuel-clad coefficient of friction; and the effects of chamfers and grooves on either the pellet or cladding will all be factors in determining the stress in the cladding during service. Fuel pellets typically have a cylindrical shape at the start of life, but thermal expansion does not result in a uniform increase in size while maintaining the same shape. There is a change in shape to a "wheatsheaf" or "hourglass" shape (see Figure 2-2) where the radial expansion is greater at the top and bottom of the pellet. This shape distortion can cause local concentrations of stress and strain at the pellet ends, resulting in ridging or "bambooing" of the cladding (See Figure 2-3). By the time of pellet-clad contact, there are cracks in the surface of the fuel. As the fuel expands and swells, the contact can lock the edges of the cracks into the surface of the clad. Further expansion affects the geometry of these cracks, opening them at the pellet-clad interface, and inducing large local cladding stresses.

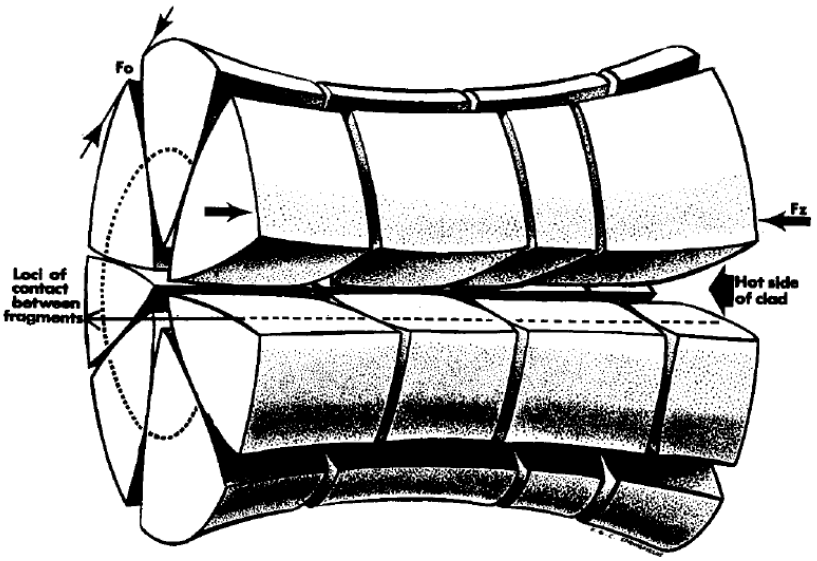

Figure 2-2 Theoretical shape of a UO_2 pellet on-power in cladding (not shown). reproduced from [4].

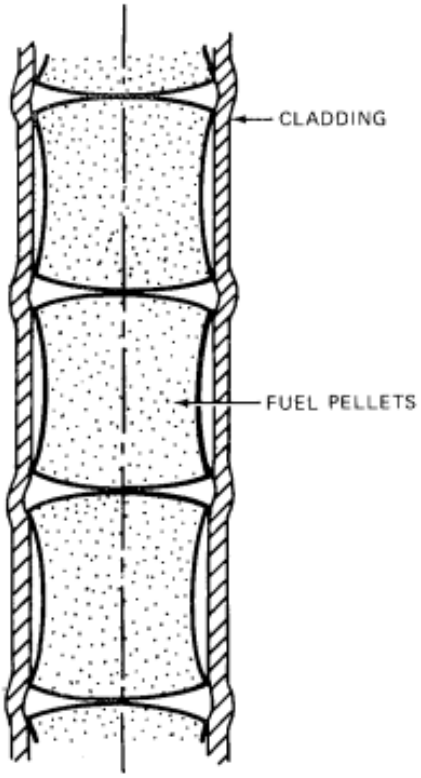

Figure 2-3 Bambooing of LWR fuel. Reproduced from [15].

Power levels affect the stresses induced in cladding by fuel, in that the maximum power level determines overall thermal expansion of the fuel. The rate of power ramping also determines the timescales over which the strain is induced during ramping. Cyclical power histories can also induce additional cracking, affecting the strain induced in the cladding [16].

The coefficient of friction between the clad and the fuel is an important factor in determining the stress induced by the fuel following a power ramp. There is no great consensus in the literature as to exactly what this value is, although values of between 0.7 and 0.9 for bare zirconium alloy cladding, and between 0.15 and 0.3 for CANLUB coatings are typically accepted as sensible, and used in modelling [14].

Stress-raisers may exist in both the fuel and the cladding, and act as initiation sites for larger cracks during operation. In the cladding, a potential cause of such features is the cracking of small, radial surface hydrides [17]. In the fuel, stress raisers may exist in the form of pellet end face chips arising from fuel handling. Large local stresses on the inside of the cladding tend to occur at the location of cladding ridges, pellet chips or cladding defects. Pellet chips also affect the temperature of the cladding. The absence of fuel in the chipped volume can be considered analogous to a massive increase in gap size. This results in significant local cooling of the cladding, relative to other parts of the cladding further from the chip [18]. At the Halden reactor, experiments observing ridge formations and their correlation with PCI failures have been used to validate fuel modelling computer codes [19].

The exact stress required to cause SCC has been the subject of many studies, and is dependent on iodine concentration, power ramp holding time, material and cladding temperature [20].

There is evidence that pellet eccentricity can be a significant cause of azimuthal temperature gradients [21]. Temperature differences between different side of fuel cladding on the order of 100°C, and possibly as high as 350°C are possible during accident conditions in cases of extreme eccentricity. Fuel rod damage is uneven in such cases, meaning the safety margin is effectively reduced [22].

2.2.1.2 Sufficient Time

Knowing the exact time of PCI-induced clad failure in-reactor is often difficult. Often all that is measurable is the time at which fission product presence in the primary circuit is distinguishably larger than the background. The first event after a pinhole failure is ingress of water into the fuel pin, so the time between this event and eventual diffusion of fission products out of the fuel pin can be considerable [23], and can be as much as ten times the initial time to failure. In cases where SCC is a factor, there are time considerations in the rate of diffusion of iodine to the crack tip [24], [25] and due to stress relaxation caused by fuel and cladding creep.

2.2.1.3 Susceptible Material

The fuel and cladding material properties both influence the incidence and rate of PCI failure. Properties of interest include both mechanical and metallurgical properties. Metallurgical properties include texture, and precipitate distribution; alloy composition; the materials resistance to the effects of radiation; and the effects of any protective coatings.

In general, material with higher yield strengths are more susceptible to SCC. This is thought to be because a higher yield strength allows for higher stress intensities to be accrued at crack tips [26]. At the high temperatures an low strain rates associated with nuclear plant operation, grain boundary sliding can occur to relieve this stress [27].

Stresses at crack tips are determined not only by the applied stress in operation, but also by residual stress resulting from manufacture (macroscopic residual stress) and material anisotropy (microscopic residual stress). Zirconium generates intergranular residual stresses in excess of its yield strength during cool down from annealing, due to its anisotropy in thermal expansion [28]. Under irradiation these intergranular stresses constantly evolve and change due to point defect creation, migration, and annihilation.

2.2.1.4 Chemical environment

Iodine has been found to be the most likely cause of the environmental changes which increase the probability of PCI. Similarly, Fe, Al, Zr, and Te iodides have also been shown to induce SCC in zirconium alloys zircaloy [29]–[31]. Iodine-induced cracking can take two forms: transgranular pseudo-cleavage, and grain boundary attack by removal of volatile iodides, with the former being the faster of the two. SCC fractures in iodine environments always contain at least some intergranular features [32].

Cs [33] and Cd are also [34] have also been shown to be capable of cracking zirconium alloys. Both species mixed together has been shown to have a greater effect than either individually [32].

2.2.2 Improving PCI Resistance

The risk of PCI is highest during changes in reactor power, of which the most unavoidable is start-up. In French reactors the ramp-rate at start up is limited to 3%/hr between 15 and 100% core full power [35] so as to minimise the risk of 'stochastic' PCI failures, caused by fuel fragment relocation as a result of fuel handling [36].

The possibility of PCI during at-power transients can be reduced by observing the PCI failure threshold (see Figure 2-4), which governs the degree to which power can safely be increased depending on the current local burnup [36]. Manoeuvring limits were first introduced for light water reactors in 1973 [14].

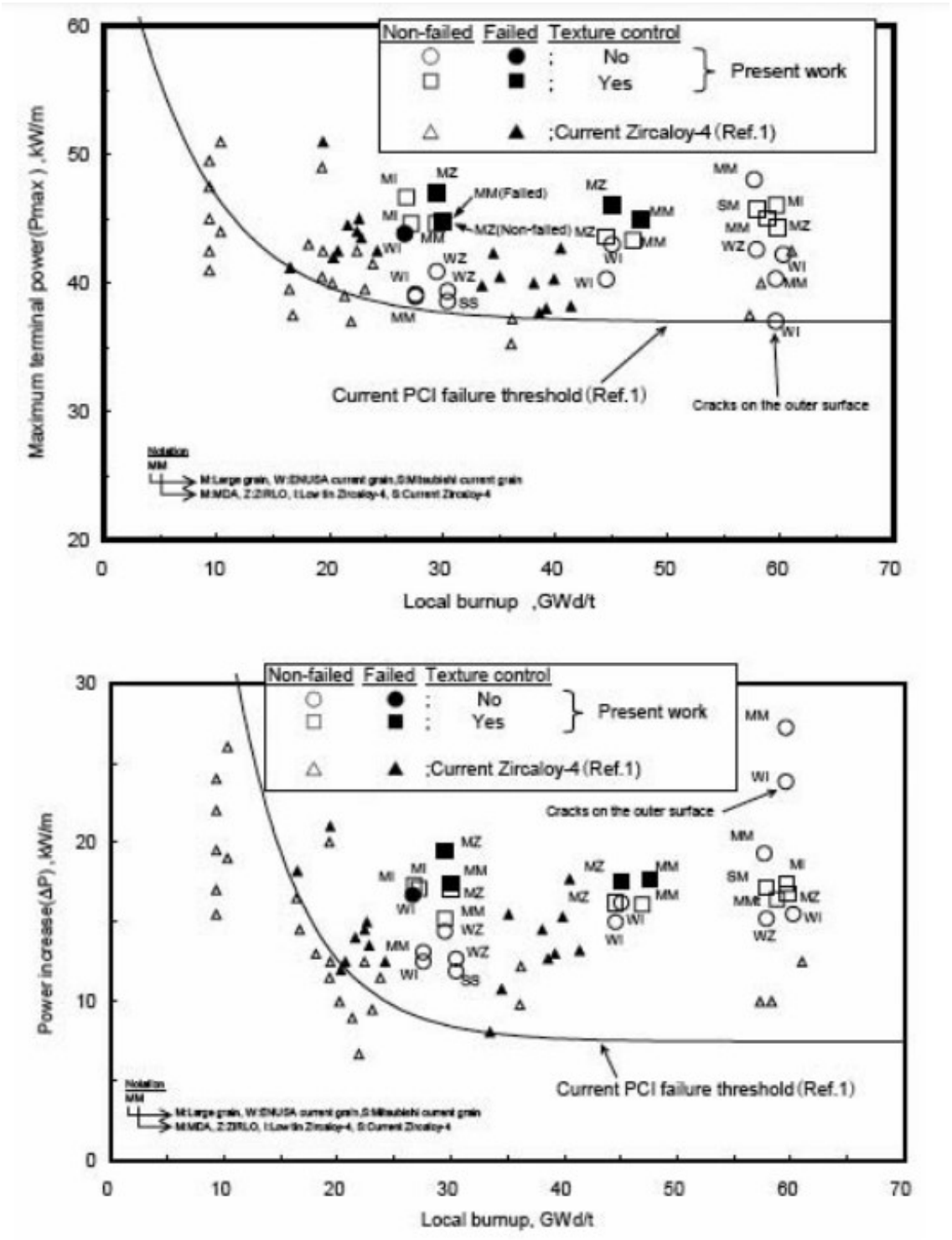

Figure 2-4 PCI threshold governing power transients with respect to local burnup. Reproduced from [37] found in [12].

Load following and frequency control operations can lead to an issue termed “fuel deconditioning” (see Figure 2-5). More specifically, PCI after an extended reduced power operation (ERPO) is also an issue that must be managed by limiting the length of the ERPO. ERPO may be used to manage grid constraints (e.g., not all of the power from the reactor is required by the grid) or technical restraints (e.g., loss of performance of cooling towers [38]. ERPO tends to cause fuel deconditioning as the pellet shrinks in size at lower power, with cladding then creeping down towards the fuel. Upon increasing power the pellet expands again, which can lead to high stresses induced by the pellet on the clad at the tips of the cracks where the fragments may have relocated, producing a stress-raising feature.

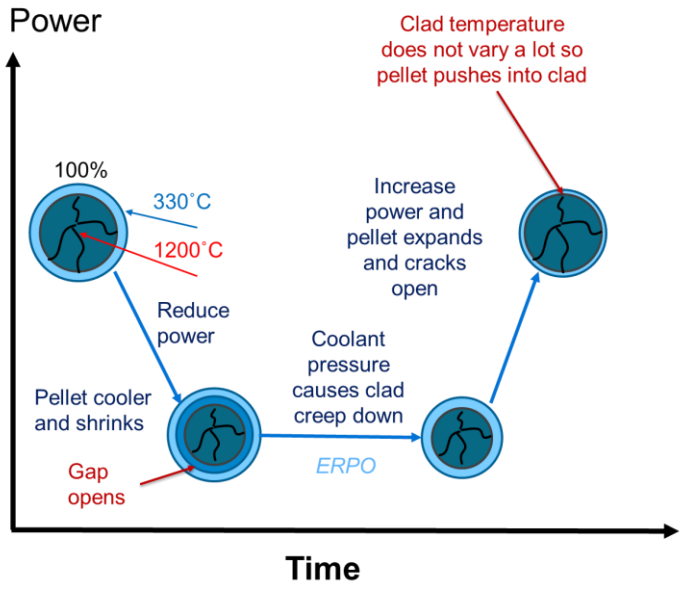

Figure 2-5: a schematic of “fuel deconditioning”. Reproduced from [39].

Although management of operating procedures has proven a very effective way of improving safety with regard to PCI, the limits it places on plant manoeuvrability are seen as onerous by industry [40]. If such operating condition restrictions could be lifted, the competitiveness of nuclear power as a whole could be improved by

extending fuel assemblies' discharge burn-up, and reducing maintenance and fuel cycle costs [5]. The financial impact of the restrictions was estimated in 1995 to be on the order of hundreds of millions of dollars per year in the period between 1981 and 1995 [41]. Not considered in this are the savings from electricity sales that would be lost during long ERPOs. In the future, as nuclear power is integrated into a grid with more intermittent renewables and less baseload fossil fuels plant designs with greater capability for load following would be at an advantage [42].

One proposal for improving PCI resistance of fuel rods is to dope the fuel pellets with Cr_2O_3, Al_2O_3 [43], TiO_2, Nb_2O_5 [44], or phosphorus [45] with the intention of altering grain structure [46], increasing viscoplasticity, and thereby producing a favourable crack pattern in the pellet, improving PCI resistance [5]. Some evidence of this improved PCI resistance was found by Arborelius et. al [43], who found considerably fewer incipient cracks in the fuel liner after ramp testing in (Cr_2O_3- and Al_2O_3-doped) ADOPT fuel as compared to standard UO_2 pellets. Nonon et al. [5] examined pellet crack patterns of chromia-doped pellets compared to those of undoped pellets, and found considerable differences. Peripheral cracks were more numerous in the doped pellets, while the central region was relatively free of cracks, which the authors posit may be due to crack healing, whereby cracked fuel raised to temperatures in the plastic region close the cracks. Nonon et al. [5] propose that this crack pattern difference could be partly responsible for the improvement in PCI resistance they observed. Fullarton et al. [47] used a variety of atomistic modelling techniques to investigate the effects of Cr_2O_3 and Al_2O_3 in UO_2 and MOX fuels, finding that such dopants precipitate $PuCrO_3$ and $PuAlO_3$ upon reaction with Pu_2O_3. The authors posited that the low thermal

conductivity calculated for $PuCrO_3$ could affect heat transfer in the rim of a doped pellet, potentially raising centreline temperatures.

Doping of fuels also affects the rate at which creep occurs in the fuel. Three creep mechanisms are identified as contributing to creep in LRW fuel during service: Nabarro-Herring, Coble, and climb-limited dislocation creep [48]. Nabarro-Herring creep occurs via the bulk diffusion of point defects in response to an applied strain. Because the energy of vacancies is typically lower under compressive stress, vacancies will diffuse from tensile to compressive regions, such that mass is transported away from these regions, causing plastic deformation. Coble creep arises from the diffusion of defects along grain boundaries. Climb-limited dislocation creep occurs at low stresses, where the movement of dislocations is limited by the arrival or emission of defects that enable them to climb over an obstacle. Both Coble and Nabarro-Herring creep are heavily influenced by grain size. Nabarro-Herring creep rate approximately varies with the inverse of the square of grain size, and Coble creep rate varies with the inverse of the cube of grain size. Doped fuel, with larger grain sizes, has a higher propensity to creep, reducing the release of fission gases from the fuel.

Fuel pellets can also be shaped to improve PCI resistance, by chamfering the end faces [14]. Such a shape change reduces the “bamboo ridge” formed by contact between the cladding and the ends of the pellets [49].

Finally, plant design improvements may be made to improve PCI resistance. These consist of fundamental changes such as increasing the number of fuel rods per assembly, which allows for lower linear heat generation rates [12], to more granular

changes such as coatings and liners on the inside of cladding [17]. Boric acid can also be used in the coolant to depress neutron flux globally across the core. This reduces power peaking relative to using control rods, the effect of which varies across the core [50].

2.3 Modelling of fracture

2.3.1 Review of Fracture Modelling Methods

Macroscopic modelling brittle fracture using methods amenable to fuel rod performance modelling is an open area of research. Two popular methods are the extended finite element method (XFEM) and cohesive zone models (CZM). Cohesive zone models rely on surface elements placed between bulk elements, which have failure criteria such that cracks can grow between the bulk elements. This method is inherently mesh-dependent [51]. This mesh dependence can be alleviated by remeshing when crack paths are not known *a priori* at the cost of increased computational expense. Adding surface elements between bulk elements already involves a significant increase in the size of the model for a given mesh refinement, with the number of nodes in a mesh of tetrahedral elements increasing by a factor of 12. If crack paths are known, the mesh can be populated with surface elements only in those regions, but otherwise surface elements must be placed between all bulk elements [52]. This introduces the issue of elastic behaviour being unduly dictated by the properties of the surface elements. XFEM is based on the standard finite element method (FEM), with local enrichment functions with additional degrees of freedom. It was introduced as a technique able to model crack growth without the computational expense inherent in methods using remeshing [53], [54]. XFEM cannot independently predict the nucleation of cracks, instead requiring external criteria. Belytschko and

Black [53] introduced a minimal remeshing FEM for crack growth, that laid the foundation for what is now referred to as XFEM. The method used discontinuous enrichment functions in the presence of cracks, allowing for crack growth arbitrarily aligned to the mesh. Remeshing was not completely done away with, as it was still necessary for severely curved cracks. Moes et al. [54] improved on this by replacing the use of the discontinuous near-tip field away from the crack tip with a Haar function. The Haar function is more straightforward and more readily generalised to nonlinear materials and three dimensions.

Another method of note is the discrete element method (DEM), which dates back to the late 1970s [55]. In DEM models, solids are represented by particles (or nodes) of differing sizes. The interaction of these particles is monitored contact by contact, and their motion is modelled particle by particle. The interactions may be approximated by connections between the particles by elastic one-dimensional elements, i.e. beams [8]. The locations of the nodes may be either regular, such as on a triangular or square mesh, or they may be irregular, which reduces the propensity for crack paths to be dictated by mesh lines as opposed to the underlying stresses [8]. DEM beams are considered broken after a failure criterion, usually force-based, is reached, and from a cascading of these events simulates a fracture propagation. DEM is commonly used in geomechanics [56]–[58] but has also been applied at engineering scale [59], [60].

Phase field modelling of brittle fracture is a method dating to the late 1990s which has been the subject of multiple simultaneous development processes [61]–[64]. The core concept of a phase field model is to model discontinuities such as crack faces by the use of a continuous field variable (the field order parameter) that models sharp

interfaces as a smooth variation between physical phases. In the context of fracture, this transition is between the fully bonded and fully broken phases. Phase field modelling can handle crack initiation, propagation, merging and branching within a single framework. Much of the phase field work in the literature is theoretical, focussed on the implementation of the method rather than applications, but it has been used for modelling hydrogen assisted cracking [65], crack propagation in functionally graded materials [66] and hydraulic fracture [67].

When compared to the purely local traditional continuum mechanics modelling techniques, several of the newer methods for modelling fracture stand out as having non-local features, such as the characteristic length-scale in phase field modelling. Non-local methods have been used to model fracture since the 1980s [68]. Bazant went on to demonstrate that non-locality is not only a desirable, but a necessary property of any model of the elastic response in a material containing distributed defects [69]. More recently, peridynamics [70], (PD, discussed in detail in section 2.3.2), has emerged as a method for modelling brittle fracture amongst other things.

Agwai et al. [71] compared the ability of peridynamics CZM and XFEM to accurately model fracture. In three different models, the predicted crack speed and paths were compared. In brittle glass, PD was able to predict small crack branches that were not seen in either CZM or XFEM but were evident in experiments. A modified XFEM, named the *cracking node method* (XFEM-CNM) by Song and Belytschko [72] over-predicted the presence of these small branches. Only small differences in crack speed were reported between the methods, and all were generally in good agreement with experiment. Dynamic fracture of a polymer was also simulated, with PD again

providing more accurate information about crack branching than CZM or XFEM. There was agreement between the methods in crack speed, although these speeds did not match experiment. In the simulations load was applied much more slowly than in the experiment, though, possibly explaining this difference. Peridynamics was also able to accurately predict crack growth towards weak interfaces in composites.

2.3.2 Peridynamics

Peridynamics (PD) is a non-local continuum mechanics modelling method, introduced by Silling [70]. Its difference from traditional continuum mechanics may best be described by its treatment of Cauchy's four fundamental assumptions in the standard theory:

- The medium described is continuous;
- Internal forces in the medium are contact forces;
- The deformation of the medium is twice continuously differentiable;
- The laws of conservation of mass, and linear and angular momentum apply in the medium.

PD dispenses with the first three of these assumptions, arguing that they are introduced for mathematical convenience, rather than for their ability to practically model reality [73]. It is clear that in real materials these assumptions are not true. Discontinuities and fractures frequently occur in real materials, violating both the first and the third assumptions. Though individual atoms may be considered to interact with each other through contact forces, many atoms together combine into longer-range forces, and it is these forces that continuum mechanics purports to describe.

PD may be considered analogous to molecular dynamics (MD) [74] in that it takes the form of discrete point masses (called material points in PD), the motions of which are determined by a summation of forces applied to each other by their neighbours.

Peridynamics can even be implemented in MD codes [75]. The key difference between the two methods is that, as a continuum method, PD need not be modelling individual atoms, meaning no empirical fitted interatomic potential is needed and bond behaviour can be directly derived. The constants of the governing equations may be tuned to accurately represent the continuum scale behaviour of real materials.

PD may be considered most analogous to MD in its form, but in its use, a comparison to finite element (FE) modelling is more apt. Problems that have traditionally been solved by FE analysis (namely structural analysis and heat transfer) may similarly be solved by PD. PD has proven a particularly useful alternative to FE for modelling materials containing discontinuities [76]. FE is based on partial differential equations, which upon approaching discontinuities in a field contain singularities. The governing equations of PD are integro-differential equations, with no spatial derivatives, meaning no such singularities occur. This means theoretically for a crack, as an example, the stresses at the crack tip should be both finite and convergent. Practically, however, this is still mesh dependent [77], [78].

The horizon, the distance over which material points interact with each other, is one of the defining features of PD. By increasing or decreasing the size of the horizon (or, more accurately, the horizon ratio, m, the ratio of horizon radius to nodal spacing) the degree of non-locality can be controlled. This is one of the primary differences between PD and classical mechanics, in that interactions do not only occur through contact, but over a distance that can be modified. The justification for the idea of having material points interact over finite distance comes in part from the forces between atoms, which extend beyond nearest neighbours. Interactions between

individual atoms decay rapidly with distance between atoms (as r^{-6} of the distance r), but the cumulative effect of molecular forces decays over far longer distances [79]. Another analogy may be drawn between peridynamics horizons and "*characteristic distance*", which controls fracture behaviour such as crack branching, and is dependent on dynamic crack tip stress states [80].

The constitutive equations of the typical bond-based peridynamics formulation are outlined here, based on [81]. The exact numerical implementation of bond-based peridynamics used in this thesis is outlined in Chapter 3. .

Imagine a continuous body $\mathcal{B}$ in a reference configuration. Let $\mathbf{x}$ and $\mathbf{q}$ be distinct points in the body, and let $dV_{\mathbf{x}}$ and $dV_{\mathbf{q}}$ be small volumes containing these points. The force that the material in $dV_{\mathbf{q}}$ exerts on $dV_{\mathbf{x}}$ is denoted by $\mathbf{f}(\mathbf{q},\mathbf{x})dV_{\mathbf{x}}\,dV_{\mathbf{q}}$ where $\mathbf{f}$ is the deformation and material properties through the entire constitutive model, which will be discussed later in this chapter. In dynamic problems, the function $\mathbf{f}$ also depends on time, although in some cases we will shorten the notation by omitting the time variable.

The pairwise force density is required to obey the following antisymmetry relation:

$$\mathbf{f}(\mathbf{x},\mathbf{q}) = -\mathbf{f}(\mathbf{q},\mathbf{x}) \tag{2.1}$$

for any $\mathbf{x}$ and $\mathbf{q}$. This property ensures that linear momentum is conserved in the model. It also can be regarded as a form of Newton's third law. The dimensions of $\mathbf{f}$ are force/volume^2. The vector in the reference configuration that connects x to q is called a *bond*.

Now consider the balance of forces on $dV_{\mathbf{x}}$ in equilibrium. Suppose there is a prescribed *body force density* field $\mathbf{b}(\mathbf{x})$ such that the net external force on $dV_{\mathbf{x}}$ is $\mathbf{b}(\mathbf{x})\, dV_{\mathbf{x}}$. Including interaction with other material particles, the total force on the small volume surrounding $\mathbf{x}$, which is required to vanish in equilibrium, is then

$$\int_{\mathcal{B}} \mathbf{f}(\mathbf{q},\mathbf{x})\, dV_{\mathbf{q}} + \mathbf{b}(\mathbf{x}) dV_{\mathbf{x}} = 0 \tag{2.2}$$

which must hold for every $\mathbf{x}$ in the body (see Figure 2-6). From this, the 3-dimensional peridynamic equilibrium equation follows immediately:

$$\int_{\mathcal{B}} \mathbf{f}(\mathbf{q},\mathbf{x})\, dV_{\mathbf{q}} + \mathbf{b}(\mathbf{x}) = 0 \tag{2.3}$$

which holds for every point $\mathbf{x}$ in the body. The dynamic version of (2.3) is obtained from d'Alembert's principle and is called the peridynamics equation of motion, which has the following form in 3D:

$$\rho(\mathbf{x})\ddot{\mathbf{y}}(\mathbf{x},t) = \int_{\mathcal{B}} \mathbf{f}(\mathbf{q},\mathbf{x},\mathrm{t})\, dV_{\mathbf{q}} + \mathbf{b}(\mathbf{x},\mathrm{t}) \tag{2.4}$$

for all x in the body and all time t, where $\mathbf{y}$ is the deformation map. Here, ρ is the density field and $\ddot{\mathbf{y}}$ is the acceleration field.

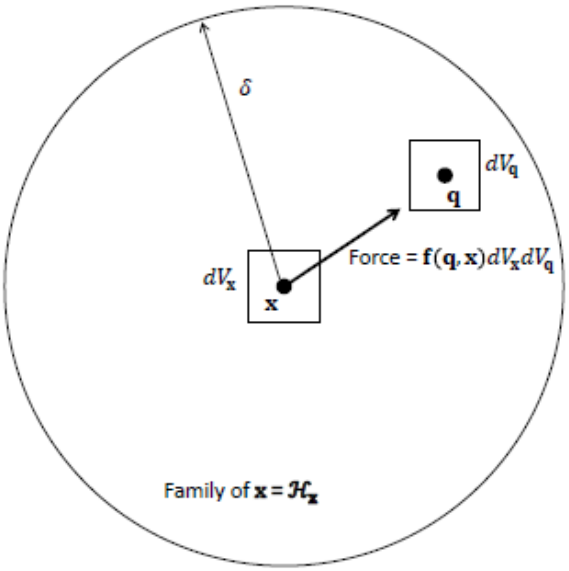

Figure 2-6: Volume element $dV_\mathbf{q}$ exerts a force $\mathbf{f}(\mathbf{q},\mathbf{x})\ dV_x\ dV_q$ on volume element dV_x.* Reproduced *from figure 2.1 [81].

In peridynamics, it is assumed that for a given material, bonds longer than a certain distance δ do not interact directly through the material model. This parameter is the *horizon.* Material within the horizon of $\mathbf{x}$ is called the *family* of $\mathbf{x}$, denoted $\mathcal{H}_\mathbf{x}$. The equation of motion therefore may be written as follows:

$$\rho(\mathbf{x})\ddot{\mathbf{y}}(\mathbf{x},t) = \int_{\mathcal{H}_\mathbf{x}} \mathbf{f}(\mathbf{q},\mathbf{x},\mathrm{t})\, dV_\mathbf{q} + \mathbf{b}(\mathbf{x},\mathrm{t}) \tag{2.5}$$

When working in 2D or 1D, rather than rewrite all the equations, it is convenient to change only the dV that appears in the integral according to the number of dimensions D.

$$dV = h_D \begin{cases} \text{differential volume} & \text{if D} = 3 \\ \text{differential area} & \text{if D} = 2 \\ \text{differential length} & \text{if D} = 1 \end{cases} \tag{2.6}$$

where

$$h_D = \begin{cases} 1 & \text{if D} = 3 \\ \text{plate thickness} & \text{if D} = 2 \\ \text{rod cross} - \text{sectional area} & \text{if D} = 1 \end{cases} \tag{2.7}$$

With this convention, the dimensions of **f** are force/volume^2 and the dimensions of ρ are mass/volume, regardless of D. Geometrically, $\mathcal{H}_{\mathbf{x}}$ is a sphere, disk, or line segment if D = 3, 2, or 1, respectively. $\mathcal{H}_{\mathbf{x}}$ could also be a subset of any of these shapes if **x** is near a boundary. Differentials such as $dV_{\mathbf{q}}$ signify differential volume, area, or length, located at the point **q**.

In bond-based peridynamics, the constitutive model governing the interaction between two material points x and q, is based on the exchange of forces through spring-like interactions.

$$\mathbf{f}(\mathbf{q}, \mathbf{x}) = f(|\mathbf{y}(\mathbf{q}) - \mathbf{y}(\mathbf{x})|, \mathbf{q}, \mathbf{x})\mathbf{M}$$

$$\mathbf{M} = \frac{\mathbf{y}(\mathbf{q}) - \mathbf{y}(\mathbf{x})}{|\mathbf{y}(\mathbf{q}) - \mathbf{y}(\mathbf{x})|} \tag{2.8}$$

Where f is a function, **y**(**x**) is the deformed position of **x** , and **M** is a unit vector in the direction of the deformed bond from to **x** to **q**. An example of a bond-based material is given by

$$\mathbf{f}(\mathbf{q}, \mathbf{x}) = \begin{cases} Ce\mathbf{M}, & \text{if } |\mathbf{q} - \mathbf{x}| \leq \boldsymbol{\delta}, \\ 0 & \text{otherwise} \end{cases} \tag{2.9}$$

Where $\boldsymbol{\delta}$ is the horizon size, C is a constant called the *micromodulus* and e is the *bond extension*, defined by

$$e = |\mathbf{y}(\mathbf{q}) - \mathbf{y}(\mathbf{x})| - |\mathbf{q} - \mathbf{x}| \tag{2.10}$$

The distinguishing feature of bond-based materials is that the force density of each bond $\mathbf{f}(\mathbf{q},\mathbf{x})$ is independent of the rest of the model, and dependent only on the relative displacement of $\mathbf{q}$ and $\mathbf{x}$. Since all of the individual interactions between material points are linear elastic spring-like, the bulk material properties are also elastic. C can be calibrated to produce given bulk material properties. The energy density (energy/volume^2) in each bond is called the *micropotential* and is denoted by w. In the case of the material in (2.10), this is given by

$$w = \frac{Ce^2}{2}. \tag{2.11}$$

The micropotential is related to the bond force density by

$$f = \frac{dw}{de} \quad \text{or} \quad \mathbf{f} = \frac{dw}{d\mathbf{Y}} \tag{2.12}$$

where

$$\mathbf{Y} = \mathbf{y}(\mathbf{q}) - \mathbf{y}(\mathbf{x}). \tag{2.13}$$

Suppose the bulk modulus k of the material to be calibrated to is known. Consider an arbitrary point $\mathbf{x}$ in the interior of the body, far from any boundaries, and prescribe a deformation of the form

$$\mathbf{y}(\mathbf{x}) = (1 + \varepsilon)\mathbf{x} \tag{2.14}$$

where ε is a small constant. The strain energy density W at $\mathbf{x}$ (energy/volume) is related to the micropotential by

$$W = \frac{1}{2}\int_{\mathcal{H}x} w dV_q \tag{2.15}$$

The factor of ½ appears in (2.15) because, for bookkeeping purposes, each endpoint 'owns' only one half of the energy stored in the bond. Combining (2.14) and (2.15) and setting

$$e = \varepsilon\xi\,, \quad \xi = |\mathbf{q} - \mathbf{x}| \tag{2.16}$$

leads to

$$W = \frac{1}{2}\int_{\mathcal{H}x} \frac{Ce^2}{2} dV_\xi = \begin{cases} \pi C\varepsilon^2\delta^5/5 & \text{if } D = 3, \\ \pi h_2 C\varepsilon^2\delta^4/8 & \text{if } D = 2, \\ h_1 C\varepsilon^2\delta^3/6 & \text{if } D = 1, \end{cases} \tag{2.17}$$

To complete the calibration process, we require that the peridynamics value of strain energy density W match the value from standard theory of elasticity:

$$W = \begin{cases} 9k\varepsilon^2/2 & \text{if } D = 3, \\ 2k'\varepsilon^2 & \text{if } D = 2, \\ E\varepsilon^2/2 & \text{if } D = 1, \end{cases} \tag{2.18}$$

Where k is the bulk modulus E is the Young's modulus, and k' is the two-dimensional bulk modulus, whose meaning is as follows. Under biaxial strain ($\varepsilon_{11} = \varepsilon_{22} = \varepsilon$), using the 2D dilatation and bulk modulus θ' and k',

$$\sigma_{11} = \sigma_{22} = k'\theta', \quad \theta' = \varepsilon_{11} + \varepsilon_{22} = 2\varepsilon \tag{2.19}$$

$$k' = \begin{cases} E/2(1-\nu) & \text{plane stress}, \\ E/2(1-\nu-2\nu^2 & \text{plane strain}, \end{cases}$$

where ν is the Poisson ratio. From (2.17) and (2.18), it follows that

$$C = \begin{cases} 18k/\pi\delta^2 & \text{if } D = 3, \\ 12k'/\pi h_2 \delta^4 & \text{if } D = 2, \\ 3E/h_1 d^3 & \text{if } D = 1, \end{cases} \tag{2.20}$$

For more general bond-based material models, in which C depends on the initial bond vector, the same calibration process can be repeated, provided there is only one unknown parameter. For example the choice

$$f = cs, \qquad s = \frac{e}{\xi} \tag{2.21}$$

and the calibration for *c* results in

$$c = \begin{cases} 18k/\pi\delta^4 & \text{if } D = 3, \\ 12k'/\pi h_2 \delta^3 & \text{if } D = 2, \\ 2E/h_1 d^2 & \text{if } D = 1, \end{cases} \tag{2.22}$$

Formulations of PD are broadly split into two categories: bond-based and state-based. State-based peridynamics is not implemented in this thesis, and therefore is not described in detail. State-based peridynamics may be briefly described as an evolution of PD in which the interaction forces need not be equal and opposite, as they do in bond-based PD. In bond-based PD the motion of a material point is governed by pairwise interactions with all material points within its horizon. Pairwise interactions do not allow for the Cauchy violation, since there are not enough degrees of freedom to have all four elastic constants (elastic modulus, *E*, bulk modulus, *K*, modulus of rigidity, *G*, and Poisson's ratio ν) vary independently. In practice this tends to mean a fixed Poisson's ratio, since it is typically more important to choose the elastic modulus. A significant limitation of bond-based peridynamics is that certain material constants (namely Poisson's ratio) are restricted to certain values (⅓ in 2D, ¼ in 3D) by the

assumption that PD forces between two material points must be equal in magnitude and opposite in direction. State-based peridynamics addresses this issue using a mathematical object called a *state.* Using states, information can be stored about a parameter (force, stretch, etc.) of all the PD bonds of a particular material point. This information is then used to determine the motion of a material point, according to the various states of its neighbouring material points within its horizon.

Failure in a bond-based model depends entirely on a critical stretch parameter. After each timestep, the stretch of all PD bonds is compared to a critical stretch value, and if the value is exceeded, the bond is considered failed and loses its ability to carry force. A critical energy release rate for the peridynamics model may be calculated based on the critical stretch, and a relation to Griffith's failure criterion made [82]. Based on this breaking of bonds, cracks naturally emerge. Broken bonds act as stress raisers, since surrounding bonds must now carry more stress in order to make up for the loss of capacity.

Crack growth occurs when bonds break in response to the stress redistributed to them. Typically, this is visualised by displaying the damage (defined as the proportion of bonds that have broken) associated with each material point. Cracks can also be visualised by colour coding broken bonds. The process of cracking occurs on a very short timescale, which may be much shorter than that of the other behaviour of a quasi-static model, so timestep management is very important in this kind of analysis [78]. A rate-dependent material model was introduced by Foster et al. [83] in order to model more plastic fracture. A failure criterion based on the energy required to break all bonds across a unit area was used to fit the behaviour of a PD body to experimentally

collected fracture toughness values. A useful application of this ability to model discontinuities is material fracture, since cracks act as discontinuities in the displacement field. Since that use forms the basis of much of this work, a focus will be placed upon it in this review. It is worth noting, however, that PD has a wide range of other uses. This review attempts to categorise and outline those applications.

2.3.2.1 Material Failure

The use of peridynamics to model material fracture is increasingly common. The first study on dynamic fracture in PD was presented by Silling [84]. More recently, peridynamics has been used to study dynamic fracture in glasses [85], polymers [86], fibre networks [87], concrete structures [88], anisotropic materials [89]–[91], functionally graded materials [92], [93], polycrystalline materials [94], and geomaterials [95]–[98]. Silling et al. [99] developed the theory of crack nucleation in PD. Crack propagation and branching in PD were studied by Ha and Bobaru [100] and Bobaru and Hu [101], with a particular focus on horizon size in the latter study. The effects of adaptive grid refinement on crack propagation in PD were studied by Dipasquale et al. [102].

2.3.2.2 Fracture distributions

Notably, the literature contains relatively few examples of fracture strength distributions modelled in PD. There are examples of arbitrary distributions of either fracture strength or elastic modulus, used to create sufficient asymmetry so as to have preferential sites to nucleate cracks, rather than many sites with equal propensity to crack, due to mesh symmetry [10], [103], [104], and many examples of mesh randomisation used for the same reason [77], [78], [105]. An exploration of a Weibull

distribution of fracture strength was performed by Blanc et al. [106], who showed that explicit modelling of micro-cracks could reproduce a Weibull distribution in PD. Casolo and Diana [107] attempted to recreate Weibull distributions using discretely randomised bond critical stretches, and found a 2-stage fracture process occurred. The first bond typically reached elastic limit at stresses lower than those of the intended Weibull distribution, and eventual fracture occurred at stresses higher than the intended distribution.

Zhang et al. [103] modelled Weibull distributions in peridynamics with the intention of recreating crack patterns found in rock. They found that randomising the critical stretch of peridynamic bonds according to a Weibull distribution they could better recreate the qualitative characteristics of rock fracture surfaces. There is, however, no mention of the quantitative change in strength with or without Weibull, and no mention of size scaling.

A common theme amongst almost all the literature on modelling fracture distributions is a qualitative approach. Crack patterns are recreated with apparently good accuracy, based solely on visual comparison, but the quantitative effect of fracture distributions (e.g. variation of force at failure) does not seem to have been investigated in any depth. There is also little consensus on how to vary the properties of the model, or even which properties to vary, in order to produce the effects of fracture distributions in real materials.

One notable example of an attempt to quantify the process of applying fracture strength distributions in peridynamics is work by Casolo and Diana [107] on 4-point bend

testing of glass beams. The strengths of the peridynamics bonds were discretely randomised according to a Weibull distribution, with a total of 25 "materials" with different critical stretches used in a given simulation. These 25 materials were then assigned randomly to bonds within the mesh. The results were characterised by a 2-stage fracture process, (see Figure 2-7) with an initial partial fracture when the elastic limit was reached in a single bond followed by a second-stage complete fracture.

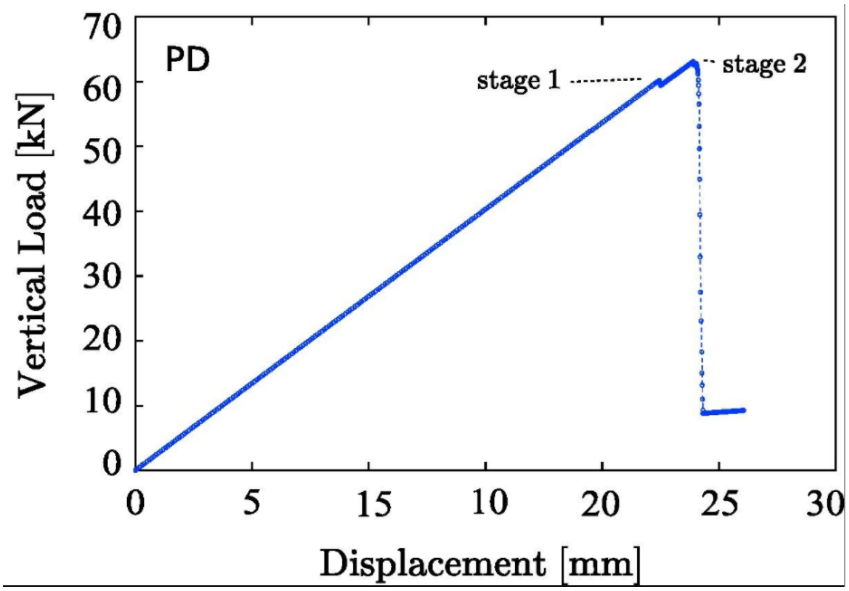

Figure 2-7 An example of the two-stage fracture process in a peridynamics model with Weibull randomisation developed by Casolo and Diana. Reproduced from [107].

The stage 1 fracture occurred at stresses below those of the intended distribution, and the stage 2, complete fracture occurred at stresses higher than those of the intended distribution, with both resultant distributions having higher Weibull moduli than intended (see Figure 2-8).

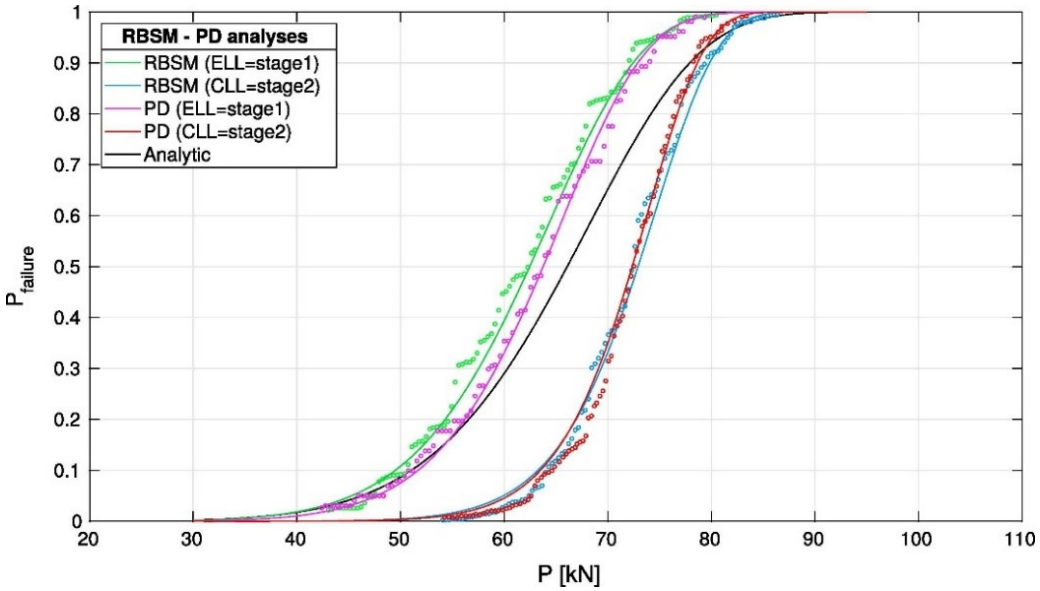

Figure 2-8 Casolo and Diana [107] found that the first stage of fracture in their Weibull-randomised peridynamics model tended to occur at stresses below the intended distribution, with good agreement at the lower tail. The stage 2 fracture conversely occurred at higher stresses, with good agreement at the higher tail of the distribution. In both cases the distribution was considerably less broad than the intended distribution. Reproduced from [107].

2.3.2.3 Peridynamics via Finite Element Modelling

Continuum scale modelling is dominated by the FEM, meaning that FE is thoroughly verified and solvers are optimised, and commercial codes to run it are readily available and widely used in industry. Implementing PD and FE concurrently is therefore a common practice, and one that takes several forms. One of the first examples of performing PD in an FE framework was work by Macek and Silling [108] in which truss elements were used to represent PD bonds in the commercial code Abaqus. The same method was implemented by Beckmann et al. [78] to also make use of the commercial FE code Abaqus, where fracture caused by thermal shock in a bi-material strip was simulated. The truss method was also used by Lall et al. [109] to model shock and vibration. Gerstle at al. [110] developed the micropolar peridynamics model to simulate linear elastic materials with varying Poisson's ratios within an FE framework in order to make use of an implicit solution algorithm. Chen and Gunzburger [111] investigated the convergence behaviour of Galerkin FE methods for discretising a PD

model, and found that in cases with jump discontinuities a local refinement of elements could produce the same convergence behaviour as in problems with smooth solutions. Du et al [112] developed a non-local diffusion method using adaptive FE and PD.

Ni et al. [113] used just the mesh-generation capabilities of an FE code to build irregular PD meshes and used them to simulate fracture in quasi-brittle solids. Combining FE with PD is also common for problems where only part of the model is intended to fracture, whether in the form of contact between multiple bodies, some in PD and some in FE [114], [115], or in the form of a single integrated PD-FE body [116]–[119].

2.4 Fuel Pellet Fracture and PCI Modelling

The nature of fuel pellet fracture lends itself to simulation and modelling, due to the obvious difficulties of observing the processes in situ. Models can, however, be compared to post-irradiation examination (PIE) images, offering an avenue for validation. Fuel pellet fracture is a complex process, and no model that exists in the literature could really be called anything approaching 'complete'. Each makes assumptions about various parts of the process, either explicitly or by omission.

Before computing power and methods were sufficient to explicitly model fuel pellet crack patterns, analytical models of fuel cracking were the only option, and are still commonplace. More recently, "smeared" cracking models, where cracks are included implicitly as changes in material properties (i.e. reduced materials stiffness), have been used. The first explicit cracking models included crack initiation sites determined *a priori*. More recently, the focus shifted to modelling the process of fracture, including

random nucleation, using a variety of methods, although smeared models are still used, especially where cracking is only part of the modelled system.

2.4.1 Analytical Modelling

Oguma [6] attempted to model the closure of the gap between clad and pellets, and verify this against out-of-pile experiment. Cracking in a transverse plane through the midpoint of the pellet was modelled, using an assumption of brittle behaviour based on the restriction that the maximum temperature remained below 1200°C, since ductile-to-brittle transition temperatures for UO_2 are around 1200 ˚C – 1400 ˚C. Fracture strength was defined as 80 MPa, the lower bound of typical UO_2 brittle fracture strengths for fuel pellets, since the 2D analysis used was known to produce lower stresses than the full 3D system.

Stresses were obtained by calculating the temperature fields across a pellet, and thereby the corresponding thermal expansion. When the stress reached the fracture strength a crack was determined to have appeared, and a portion of the stress relaxed. Figure 2-9 shows the predicted crack pattern as the pellet is ramped to a power of 40 kW m^{-1}. This cracking model was used to predict the increase in size of the pellet, from which a gap closure model could be inferred.

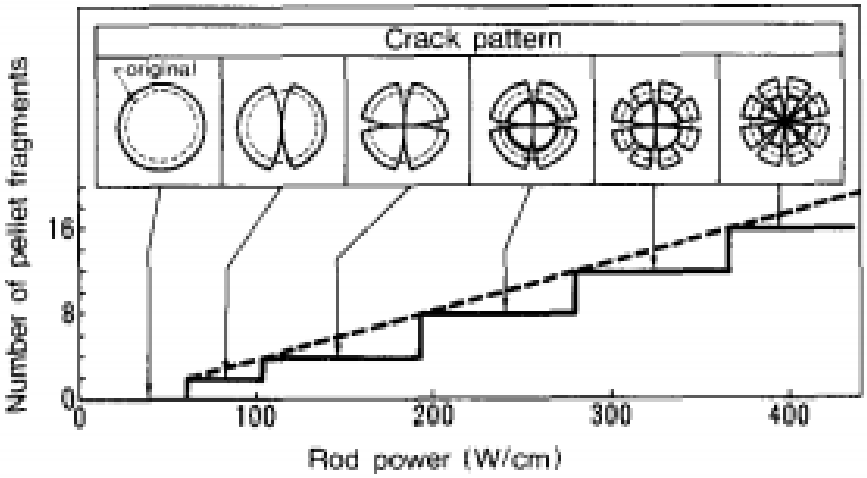

Figure 2-9 Analytically predicted crack pattern during rise to power, as calculated by Oguma. Reproduced from [6].

This linear increase in the number of pellet fragments with increasing power was compared to an experiment, where a UO_2 annulus was heated by a central tungsten element [120]. The relationship between cracking (this time determined as number of cracks) and power was again determined to be linear. The onset of cracking occurred earlier than predicted analytically, which was attributed to the steeper radial temperature gradient of the experimental setup as compared to the analytical model.

2.4.2 Smeared Models

The explicit modelling of nuclear fuel pellet cracking is an unsolved challenge, and likely to remain so for the foreseeable future, as it requires methods beyond traditional continuum mechanics. In the meantime, significant progress can be made on modelling of fuel pellet behaviour using 'smeared' cracking models which maintain the assumptions of classical continuum mechanics. Smeared crack models are the method currently used most often in the majority of 1D fuel performance computer codes.

This can be done by avoiding the discontinuities inherent in cracking by "smearing" the effect of the crack across the whole pellet. First, a method of determining the

number of cracks must be formulated, then mechanical properties of the model can be altered to produce the intended material behaviour. For example, Jankus and Weeks [121] determined a fracture criterion based on an analytical model

$$\sigma_{\mathrm{f}} = 15000 + 3.7\, T_{\mathrm{k}} \tag{2.1}$$

where σ_{f} is the ultimate tensile stress in kg cm^{-2}, and T_{k} is the temperature in K. The elastic modulus and Poisson's ratio were modified each time the fracture stress was breached in order to describe the deformation of a cracking fuel pellet.

$$E^n = \frac{2}{3}E, \quad \text{and} \quad \nu^n = \frac{1}{2}\nu \tag{2.2}$$

The second method for including cracks in a smeared manner is to model 'crack strains', the dimensions of the cracks as fractions of the corresponding pellet volume in the stress-strain relations. By this method, when rupture stress is exceeded, crack strains are included in the constitutive equations [122].

BISON [123] is a fuel performance code built in the Multiphysics Object-Oriented Simulation Environment (MOOSE). MOOSE is a FE-based framework offering parallel solution of systems of coupled non-linear partial differential equations [124]. Two approaches are available to model fracture in BISON: an empirical relocation model and a smeared cracking model. The empirical relocation model alters the pellet diameter according to burnup. The smeared model simulates cracking by adjusting the elastic constants at material points [124], [125].

FRAPCON [126] is a FORTRAN 90 code that calculates the steady-state response of light-water reactor fuel rods during long-term burnup. As a 1.5-D code, FRAPCON

considers radial fuel cracking in the aggregate only. Fracture is accounted for by a change in fuel-cladding gap size and fuel diameter with regards to gap conductance and fuel interaction with cladding.

2.4.3 Explicit Models

Typically, in 2-D or 3-D fuel performance codes, crack patterns In 1993 Caillot et al. [127] used FEM to model the mechanical effects of fuel pellet thermal expansion on cladding, verified against irradiation experiment. In the simulation fracture patterns were applied *a priori*, and remained constant throughout. In 1995 Bernaudat [128] calculated fuel rod diameter changes due to thermal expansion with good accuracy by including pellet fragment relocation and accommodation, as well as crack healing. In 2001 Brochard et al. [129] modelled contact forces between a fuel pellet and the clad in a segment of the fuel pellet that contained a crack face. BISON has been used to model PCMI in the event of cracking [124], but limitations inherent to FEM restrict the modelling of crack growth.

Williamson and Knoll [130] modelled cracking of a PWR pellet in 3-D using the cohesive zones model. This work captured the interactions between transverse and radial cracks, but suffered from a lack of capability to model stochastic crack nucleation and growth, with crack paths determined *a priori* by the cohesive zone locations.

Huang et al. [8] were among the first to explicitly model fuel fracture patterns, by using DEM.The results showed radial cracking on the upward power ramp (see Figure 2-10), and circumferential cracking on the downward power ramp. Comparison is made to analytical methods such as Oguma's [6] to show that the linear increase in crack

number as a function of increase in power seen in the results is to be expected. The pattern of cracking is notably different to that predicted by Oguma, with not circumferential cracks growing during heat-up. Notably, this work predicts widespread microcracking, not seen in other methods. The length of the cracks is not discussed in great detail by the authors but would be an interesting comparison metric between methods. It would appear that in this work, the depth of the crack is controlled by the shape of the stress field (i.e. the point at which the radial stress begins to turn compressive, closer to the centre) rather than its magnitude. The microcracking may be acting as a means of supressing further large cracks from nucleating, by dissipating that strain energy which could otherwise be dissipated by a large crack.

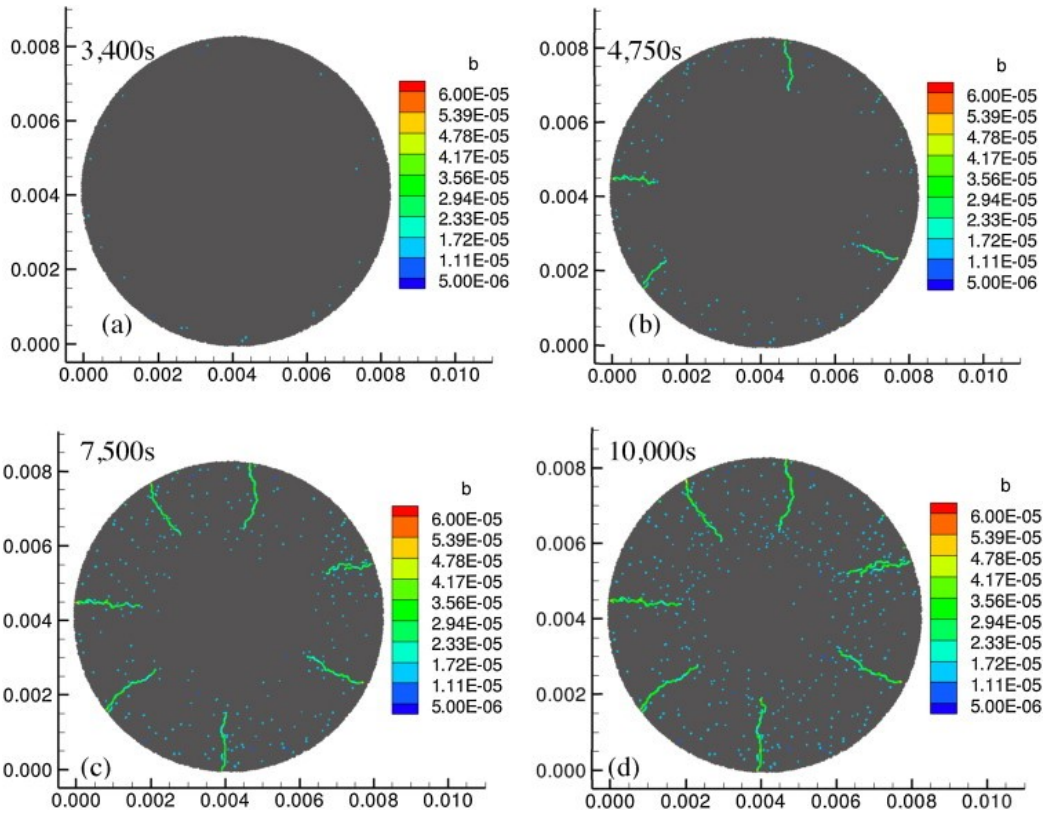

Figure 2-10 A model of a PWR pellet by Huang et. al. [8] showed cracks nucleating at different times across a 10,000s ramp to 25kW m^{-1}. There is also considerable microcracking across the pellet. Colour corresponds to gap size. Reproduced from [8].

Mella and Wenman [75] used a LAMMPS implementation of PD to model annular Advanced Gas-cooled Reactor (AGR) fuel pellets. This model was unusual in that it simulated a pellet in 3-dimensions, allowing it to accurately capture features such as the mid-height pellet crack. When ramped to powers of 10 and 15 W g^{-1}, there was good agreement with AGR PIE data with regard to the mean number of cracks observed on both the inner and outer surfaces of the fuel pellets. It was observed that the Y-shaped cracks that arose within the pellet (see Figure 2-11) were the coalescence of two cracks that nucleated at the pellet outer surface, and one crack which nucleated at the pellet inner surface, as opposed to an alternative explanation of this final crack pattern whereby the crack nucleated at the inner surface before branching. This work perhaps showed for the first time the insight available from explicit crack models not available from PIE alone and why they are worth pursuing.

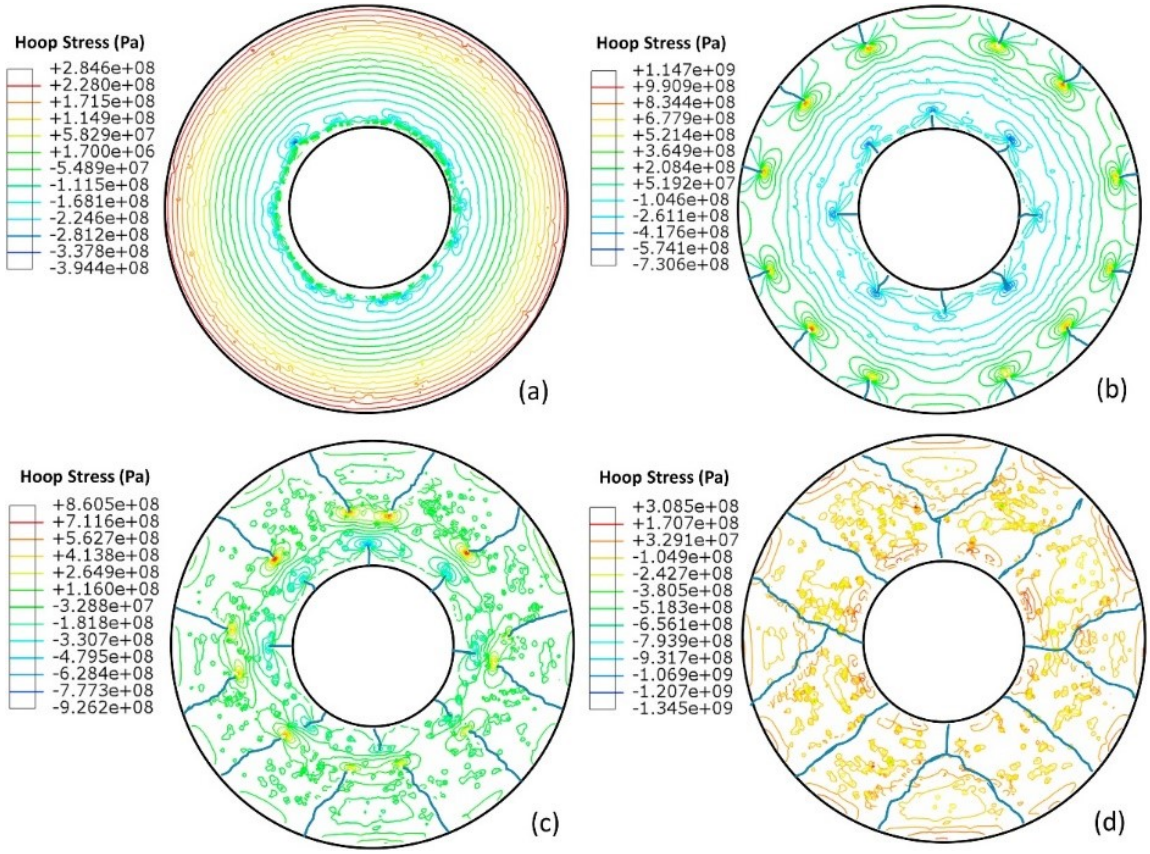

Figure 2-11 In the peridynamics model by Mella and Wenman [75] of an AGR fuel pellet, evidence was found that cracks initiate on both the inner and outer annulus surfaces. Reproduced from [75].

It was also found that, like the crack number data from PIE, a Weibull distribution could reasonably be plotted for the number of cracks on the outer surface of the pellet. The distribution itself is a good match to the PIE data (see Figure 2-12) although there is more evidence of the possibility of very large numbers of cracks (>15) in the PIE data, and the peridynamics data is strongly centred around its mean value. It is notable that this variation in the number of pellet cracks arose not from intentional variation in the material properties of the model, such as elastic modulus or fracture stress, but from the same numerical rounding effects that allow nucleation of single cracks.

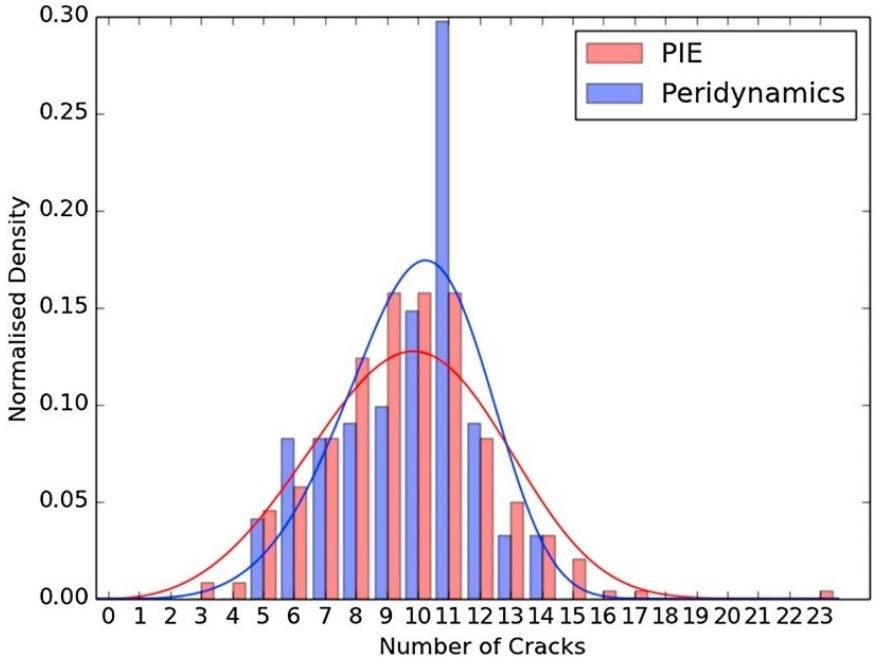

Figure 2-12 Mella and Wenman[75] compared the number of cracks in their AGR pellet model to a Weibull distribution representing crack numbers observed in PIE, and found a good degree of similarity, although the peridynamics model did not produce very low or high crack numbers in the same quantity as the PIE data. Reproduced from [75].

Wang et al. [9] also modelled fuel fracture using PD, with particular focus on the effect of ramp rate. Pellets were ramped to powers ranging from 10-45 kW m^{-1} over 5 s, held at power for 5 s, and then ramped down to zero power over 5 s. The pellets cracked in a hierarchical manner, where some cracks grow much longer than others, in a roughly alternating manner, suggesting that the longer cracks are dominant, and growing at the expense of the others. For each power case, the cracks were categorised as short (<30% radius length), medium (30% – 50% radius length) or long (>50% radius length) in order to quantitatively investigate the effect of peak radial power level on the hierarchical characteristics of macroscopic crack lengths in fuel pellets. This allowed the increase in the number of cracks associated with higher power levels to be described more precisely. The total number of cracks is a useful metric for understanding the fracture of a pellet, but longer cracks are more likely to act as initiation points for circumferential cracks on a ramp down. For this reason, it is useful

to know if additional cracking at higher powers is associated with an increase in long cracks. As shown in {figure}, long cracks make up roughly one third of all cracks at most power levels. Notable exceptions to this are: 0-10 kW m^{-1}, where little cracking of any kind occurs; and 45 kW m^{-1}, where the number of long cracks is lower than that seen at 40 kW m^{-1}. This reduction is almost certainly a statistical anomaly, and it can reasonably be said that the number of long cracks is proportional to the total number of cracks. The proportion of the cracks made up of medium-length cracks varies from ~16% to ~32%, with no obvious trend relative to power level. This can be attributed to the arbitrary nature of the definitions for short, medium, and long cracks.

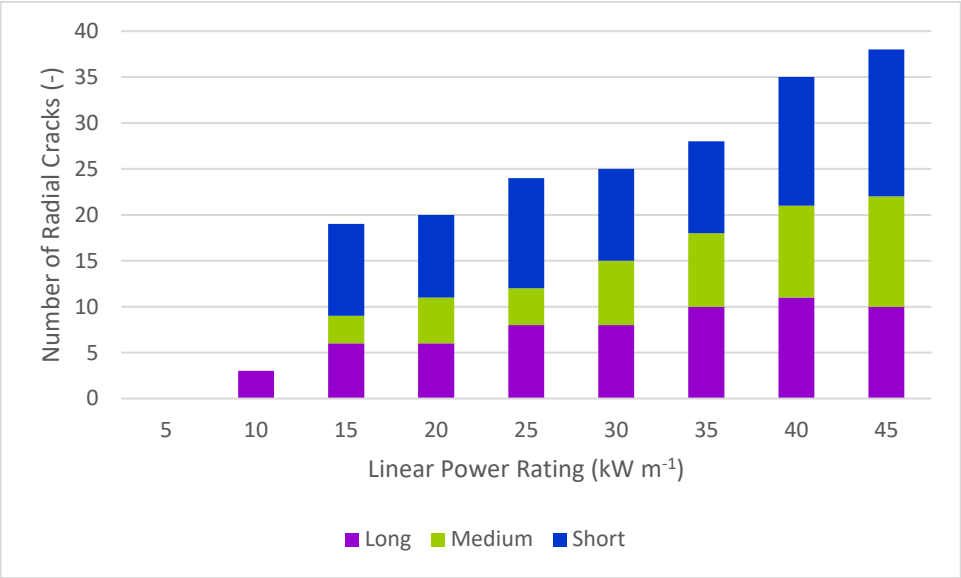

Figure 2-13: Number of radial cracks originating at the pellet surface at each power level in the work of Wang et al. {}. Cracks are characterised as short (<30% radius length), medium (30% – 50% radius length) or long (>50% radius length).

Oterkus and Madenci [10] included oxygen diffusion as an additional factor in their PD model of fuel fracture. The model was of a pellet taken instantaneously to 2 x 10^8 W m^{-3} (roughly equivalent to 10 kW m^{-1}) and allowed to equilibrate over 4.5 s before ramping down to 0 W m^{-3} over 4.5 s. Oxygen diffusion has the effect of raising the

centreline temperature by around 80 K, significantly altering the stress profile. The resulting crack patterns showed multiple cracks initiating simultaneously and growing in approximately straight lines toward the centre of the pellet during heat-up before circumferential crack growth and coalescence on the ramp down (see Figure 2-14). Adjacent cracks often have significantly different lengths, displaying the hierarchical crack growth also shown by Wang et al. [9]. The fuel temperature difference induced by modelling of oxygen diffusion is notable in that it produces faster crack growth. In the pellet where oxygen diffusion is considered, the overall number of radial cracks is increased from 10 to 13. This increase came in the form of extra short cracks initiated during the initial heat-up phase. Faster crack growth rate was also observed.

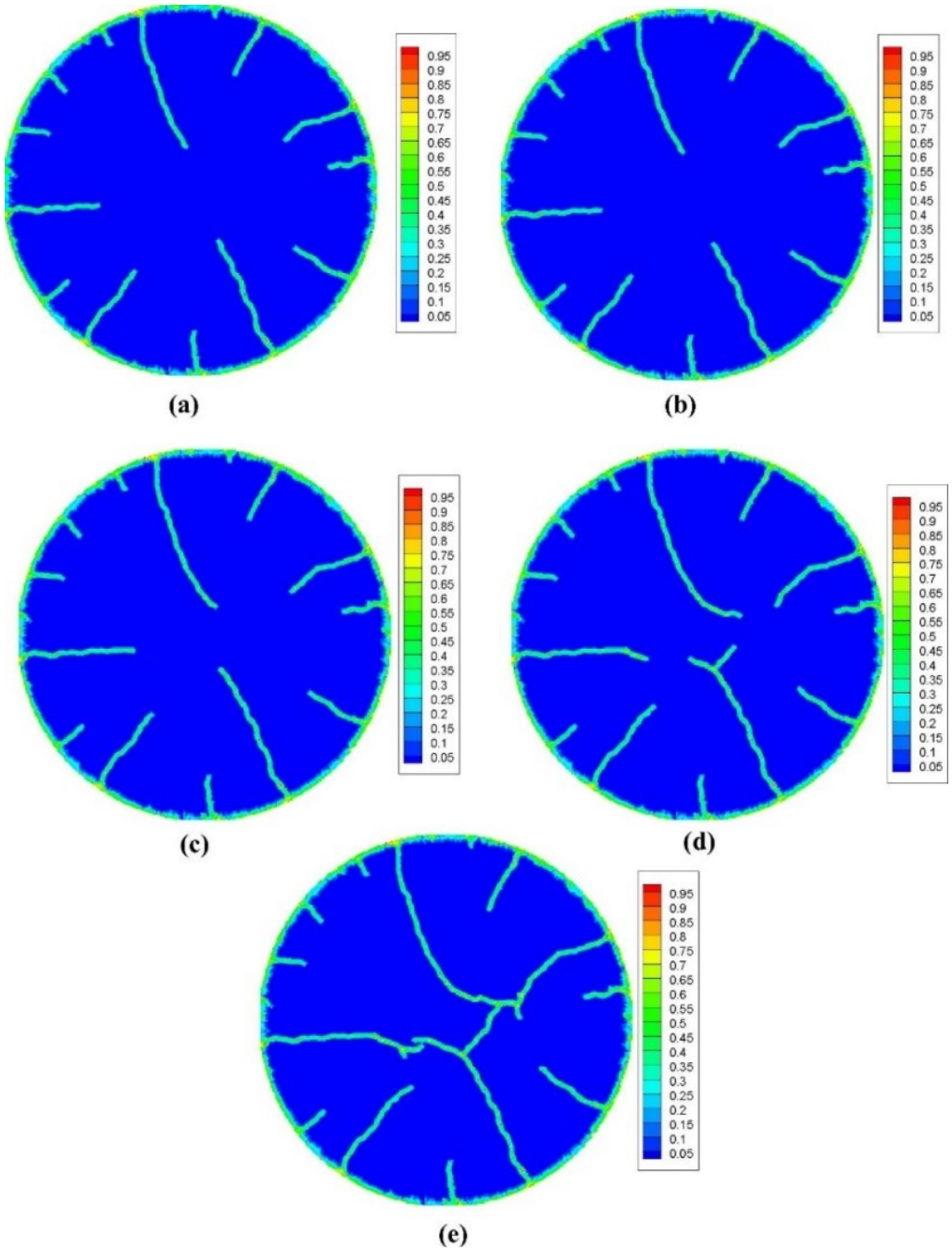

Figure 2-14 Damage (proportion of bonds connnected to material point broken) plots from a PD model of a PWR pellet by Oterkus and Madenci (Figure 17 [10]) having been equilibrated at ~10 kW $m^{-1}$for 4.5s, on a linear power down-ramp to 0 W m^{-1} over 4.5s (a) t = 5.4s (b) t = 6.3s (c) t = 7.2 s (d) t = 8.1 s and (e) t=9s. Reproduced from [10].

Jiang et al. [11] implemented the XFEM in the MOOSE framework and BISON fuel performance code in order to model fuel pellet fracture. The model nucleates cracks without *a priori* nucleation sites, thanks partly to the randomisation of the fracture

criterion. The method is benchmarked against the non-nuclear test case of a rectangular plate with an inclined crack. Crack patterns of a simulated pellet, ramped to 25 kW m^{-1}, show reasonable crack patterns, with 6 visible cracks of varying lengths, and many much smaller cracks. The effect of critical stress intensity factor (SIF) is shown. With critical SIF of 2 MPa $m^{1/2}$ the cracks are exceptionally curved (see Figure 2-15) and extend around the centre of the pellet. Increasing the critical SIF to 4 MPa $m^{1/2}$ produces much straighter, shorter cracks, although notably does not decrease the number of visible cracks. The lack of crack coalescence and branching is particularly noticeable in the lower critical SIF case, where the cracks are quite unrealistic in appearance, and may have benefitted from 'spending' some of their capacity for growth on branching rather than extending. Crack branching and, in particular, coalescence are vital processes in modelling fuel pellet fracture, and that this model appears to use an arbitrary increase in critical SIF to produce a pattern where coalescence would not be expected is worrisome. In the initial case with lower critical SIF, cracks pass close to each other, but do not coalesce.

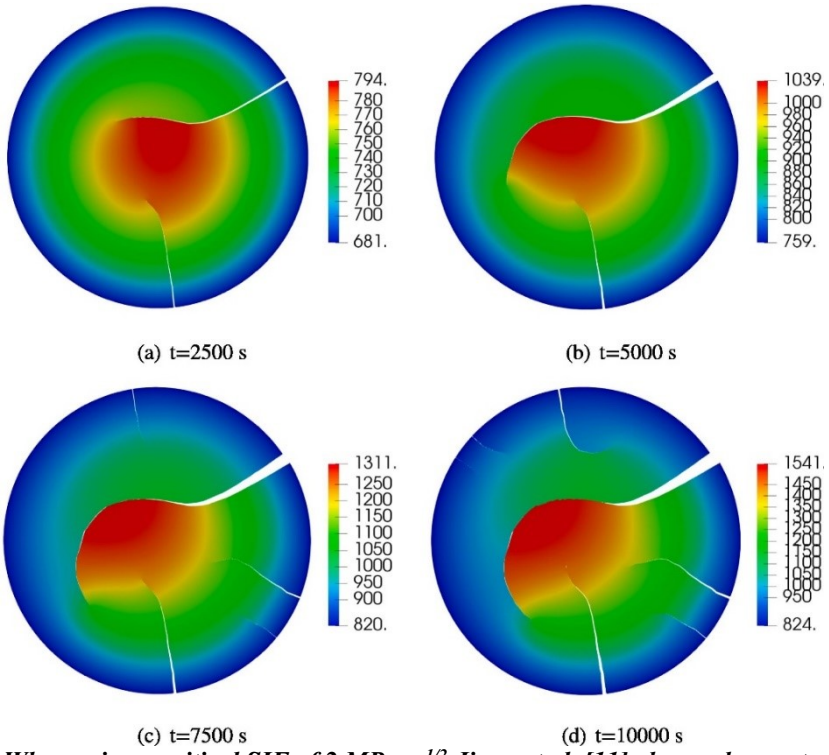

Figure 2-15 When using a critical SIF of 2 MPa $m^{1/2}$ Jiang et al. [11] observed curvature in their PWR pellet crack patterns modelled using XFEM. Colour correspons to temperature in Kelvin. Reproduced from [11].

A recent phase field model by Li and Shirvan [131] coupled the effects of oxygen diffusion, heat conduction, mechanical deformation and fracture. The UO_2 pellet was ramped to power over ~3 days to mimic a real fuel pin power history (see Figure 2-16).

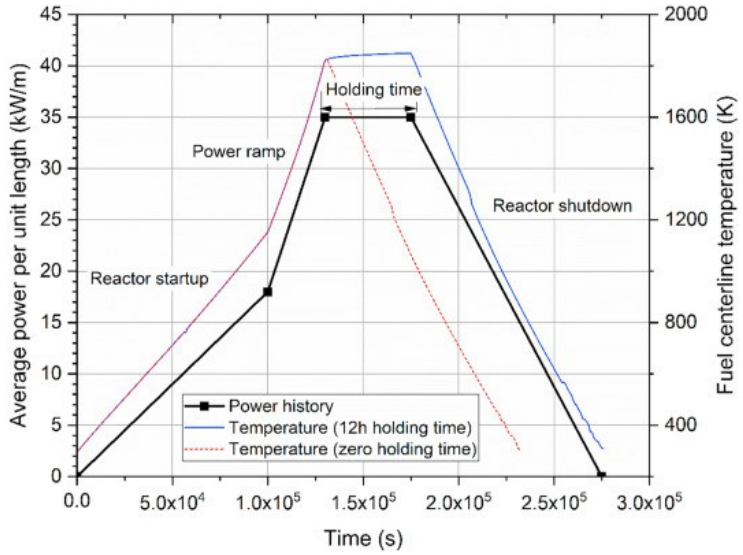

Figure 2-16 The power history modelled by Li and Shirvan [131] in a phase field model of a PWR fuel pellet. Reproduced from [131].

Notable in the Li and Shirvan model [131] is that the radial cracks all nucleate in the earliest stage of the power ramp up (see Figure 2-17), before growing hierarchically over the rest of the ramp up. There is no additional stage of crack nucleation until circumferential cracks form upon the power ramp down.

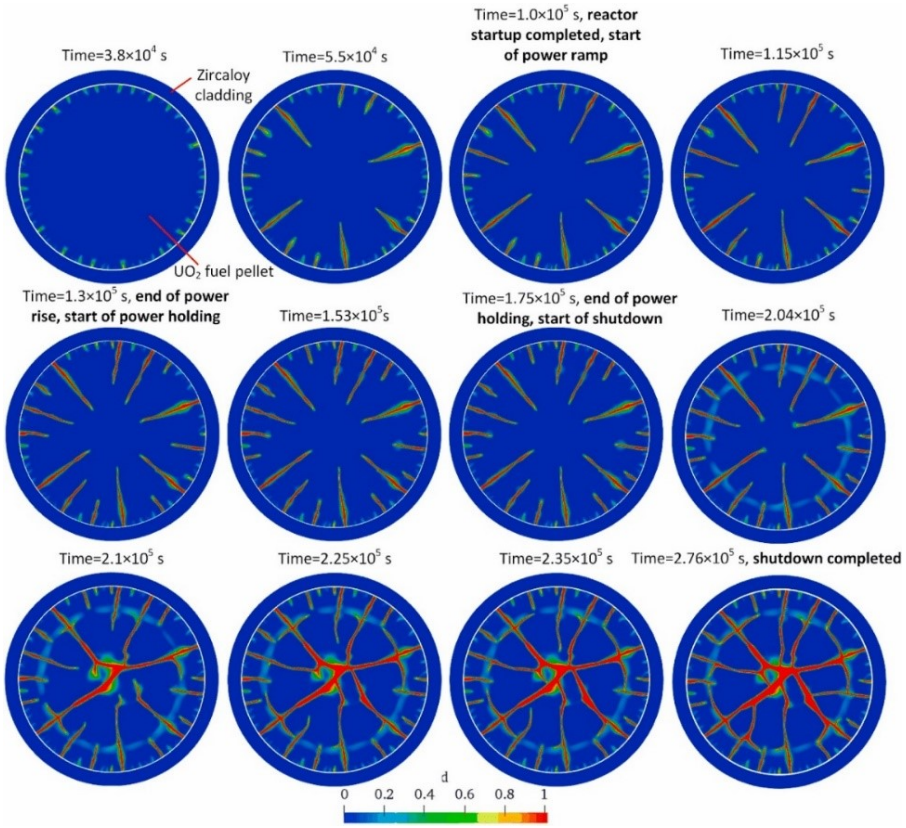

Figure 2-17 In the phase field model, where colour denotes the damage parameter, by Li and Shirvan [131] many cracks nucleate in the first stage of the simulation ($t < 3.8 \times 10^4$ s) before growing hierarchically. Little crack growth is observed in the holding period, before circumferential cracking and crack coalesence occur in the shutdown stage. Reproduced from [131].

2.5 Summary

How best to model brittle fracture is an open question, with many competing proposed methods including the XFEM [53], [54], [132], the phase field method [62]–[64], the DEM [55], CZM [51] and PD [70]. Methods for modelling fracture in continuum-scale engineering problems are numerous, with no one dominant method emerging. For this

reason, it is necessary (and desirable) that research is carried out on all of these methods. In order to limit the scope of this thesis, only PD is considered in depth.

A fundamental part of brittle fracture is the statistical distribution of fracture strengths in brittle materials [133] stemming from randomness in flaw sizes in the material, and the dependence of brittle fracture strength on the size of a critical flaw [82]. This phenomenon is largely neglected in the literature on modelling of brittle fracture. Randomisation is often applied to fracture criteria, material properties or the mesh [10], [103], [104] with the intent of introducing heterogeneity in the model, but much less often is this randomisation analysed or applied directly in such a way as to match experimentally observed behaviour [107].

The phenomenon of PCI is an area of ongoing investigation in the nuclear industry [2], [5], [14], [23], [40], and there is considerable influence on the failure conditions for PCI from cracking in the pellet. PCI is currently managed largely by restrictions on plant operating conditions, which come at the cost of reduced load factors (due to power ramp rate limits) and reduced flexibility in load following. There is suggestion in the literature that altering the fracture behaviour of fuel pellets could alleviate some of the risk associated with PCI.

Explicit modelling of fuel pellet fracture patterns is a relatively new phenomenon compared to analytical [6] and smeared [121] modelling methods. While qualitative analysis of modelled PWR pellet fracture patterns relative to post-irradiation examination images is common [10], [11], [98], [104], it is less common to see a quantitative comparison of the number of radial cracks between models [8], [104]. It

was also noted that no formalised method has been published to date to implement a measured '*engineering*' Weibull distribution for a material and implement it accurately into these fracture models for brittle materials. This would be of great use for engineering models in general in many fields not just nuclear fuel modelling.

With this in mind, the aims of this work are as such:

- Investigate the suitability of peridynamics as a method for modelling distributions of fracture strength (in the form of Weibull distributions) in the context of brittle fracture of ceramics.
- Formulate a method for accurately recreating a Weibull distribution in one-dimensional and two-dimensional peridynamics.
- Construct a thermo-mechanical model of a PWR fuel pellet in-service.
- Determine the effects of varying Weibull modulus on the qualitative and quantitative aspects of crack nucleation and growth in a low-burnup PWR fuel pellet. Compare these findings to quantitative and qualitative data in observed PIE, and make an estimation of the Weibull properties of PWR fuel.

The following chapter outlines the methodology used to construct peridynamics models in one dimension (investigated in Chapter 4), and in two dimensions (investigated in Chapter 5 and utilised for PWR pellet models in Chapter 6). Also included are considerations of the use of different estimators for probability of failure when calculating Weibull parameters, and a simple benchmarking exercise to ensure the two-dimensional peridynamics model produces accurate elastic behaviour.

2.6 References

[1] T. Helfer, P. Garcia, J. Ricaud, D. Pancq, and C. Struzik, "Modelling the Effect of Oxide Fuel Fracturing on the Mechanical Behaviour of Fuel Rods," in *Pellet-Clad Interaction in Water Reactor Fuels Transactions, Aix-en-Provence.*, 2004, pp. 367–77.

[2] N. Marchal, C. Campos, and C. Garnier, "Finite element simulation of Pellet-Cladding Interaction (PCI) in nuclear fuel rods," *Comput. Mater. Sci.*, vol. 45, no. 3, pp. 821–826, 2009, doi: 10.1016/j.commatsci.2008.10.015.

[3] J. H. Gittus, "Theoretical analysis of the strains produced in nuclear fuel cladding tubes by the expansion of cracked cylindrical fuel pellets," *Nucl. Eng. Des.*, vol. 18, no. 1, pp. 69–82, Jan. 1972, doi: 10.1016/0029-5493(72)90037-4.

[4] J. H. Gittus, D. A. Howl, and H. Hughes, "Theoretical Analysis of Cladding Stresses and Strains Produced by Expansion of Cracked Fuel Pellets," *Nucl. Technol.*, vol. 9, no. 1, pp. 40–46, Jul. 1970.

[5] C. Nonon *et al.*, "PCI BEHAVIOUR OF CHROMIUM OXIDE-DOPED FUEL," Aix-en-Provence, Mar. 2004.

[6] M. Oguma, "Cracking and relocation behavior of nuclear fuel pellets during rise to power," *Nucl. Eng. Des.*, vol. 76, no. 1, pp. 35–45, Oct. 1983, doi: 10.1016/0029-5493(83)90045-6.

[7] L. A. Walton and D. L. Husser, "Fuel pellet fracture and relocation," Art. no. IWGFPT--13, 1983, Accessed: Nov. 03, 2020. [Online]. Available: http://inis.iaea.org/Search/search.aspx?orig_q=RN:17006978

[8] H. Huang, B. Spencer, and J. Hales, "Discrete element method for simulation of early-life thermal fracturing behavior in ceramic nuclear fuel pellets," *Nucl. Eng. Des.*, vol. 278, pp. 515–528, Oct. 2014, doi: 10.1016/j.nucengdes.2014.05.049.

[9] Y. Wang, X. Zhou, and M. Kou, "Peridynamic investigation on thermal fracturing behavior of ceramic nuclear fuel pellets under power cycles," *Ceram. Int.*, vol. 44, no. 10, pp. 11512–11542, Jul. 2018, doi: 10.1016/j.ceramint.2018.03.214.

[10] S. Oterkus and E. Madenci, "Peridynamic modeling of fuel pellet cracking," *Eng. Fract. Mech.*, vol. 176, pp. 23–37, May 2017, doi: 10.1016/j.engfracmech.2017.02.014.

[11] W. Jiang, B. W. Spencer, and J. E. Dolbow, "Ceramic nuclear fuel fracture modeling with the extended finite element method," *Eng. Fract. Mech.*, p. 106713, Oct. 2019, doi: 10.1016/j.engfracmech.2019.106713.

[12] "Review of Fuel Failures in Water Cooled Reactors," Feb. 28, 2019. https://www.iaea.org/publications/8259/review-of-fuel-failures-in-water-cooled-reactors (accessed Sep. 03, 2020).

[13] B. Chen, P. E. J. Flewitt, D. J. Smith, and C. P. Jones, "An improved method to identify grain boundary creep cavitation in 316H austenitic stainless steel," *Ultramicroscopy*, vol. 111, no. 5, pp. 309–313, Apr. 2011, doi: 10.1016/j.ultramic.2011.01.013.

[14] B. Cox, "Pellet-clad interaction (PCI) failures of zirconium alloy fuel cladding — A review," *J. Nucl. Mater.*, vol. 172, no. 3, pp. 249–292, Aug. 1990, doi: 10.1016/0022-3115(90)90282-R.

[15] D. R. Olander, “Fundamental aspects of nuclear reactor fuel elements,” California Univ., Berkeley (USA). Dept. of Nuclear Engineering, TID-26711-P1, Jan. 1976. doi: 10.2172/7343826.
[16] D. G. Hardy and A. S. Bain, presented at the Topical Meeting on Water Reactor Fuel Performance, St Charles, Illinois, May 1977.
[17] B. Cox, “Proc. 4th Int. Symp. on Zirconium in the Nuclear Industry,” *ASTM-STP 681*, p. 306, 1978.
[18] J. R. Berretta, R. B. Suman, D. P. Faria, P. A. Rodi, and C. Giovedi, “Analysis of pellet cladding mechanical interaction using computational simulation,” presented at the INAC 2017: International Nuclear Atlantic Conference, Brazil, 2017.
[19] M. ICHIKAWA, “Studies of LWR Fuel Performance Under Power Ramping and Power Cycling Utilizing Inpile Measurement and Fuel Modeling,” *Proc. Int. Top. Meet. LWR Fuel Perform. 1988*, pp. 253–266, 1988.
[20] J. T. A. Roberts *et al.*, “A Stress Corrosion Cracking Model for Pellet-Cladding Interaction Failures in Light-Water Reactor Fuel Rods,” *Zircon. Nucl. Ind.*, Jan. 1979, doi: 10.1520/STP36686S.
[21] P. M. Jones, F. Casadei, and H. Laval, “Modelling of azimuthal effects arising from interaction between clad deformation and heat transfer under LB LOCA conditions,” *Nucl. Eng. Des.*, vol. 79, no. 3, pp. 267–276, Jun. 1984, doi: 10.1016/0029-5493(84)90041-4.
[22] S. YANAGIHARA, S. SHIOZAWA, and S. SAITO, “Effect of Fuel Pellet Eccentricity with Cladding on Fuel Rod Thermal Behavior under Reactivity Initiated Accident Condition,” *J. Nucl. Sci. Technol.*, vol. 19, no. 6, pp. 469–481, Jun. 1982, doi: 10.1080/18811248.1982.9734170.
[23] H. Mogard, D. A. Howl, and M. Grounes, “The international TRANS-RAMP II fuel project - A study of the effects of rapid power ramping on the PCI resistance of PWR fuel,” *Proc Top. Meet. LWR Fuel Perform.*, pp. 232–244, 1988.
[24] M. Saidy, W. H. Hocking, J. F. Mouris, P. Garcia, G. Carlot, and B. Pasquet, “Thermal diffusion of iodine in UO2 and UO2+x,” *J. Nucl. Mater.*, vol. 372, no. 2, pp. 405–415, Jan. 2008, doi: 10.1016/j.jnucmat.2007.03.272.
[25] W. H. Hocking, R. A. Verrall, and I. J. Muir, “Migration behaviour of iodine in nuclear fuel,” *J. Nucl. Mater.*, vol. 294, no. 1, pp. 45–52, Apr. 2001, doi: 10.1016/S0022-3115(01)00447-0.
[26] D. G. Hardy and A. S. Bain, in *Proc. 3rd. Int. Conf. on Zirconium in the Nuclear Industry, ASTM-STP 633*, Quebec City, Aug. 1976, p. 98.
[27] A. Bhaduri, *Mechanical Properties and Working of Metals and Alloys*. Accessed: Jul. 03, 2022. [Online]. Available: https://link.springer.com/book/10.1007/978-981-10-7209-3
[28] E. Tenckhoff, *Deformation Mechanisms, Texture, and Anisotropy in Zirconium and Zircaloy*. ASTM International, 1988.
[29] D. Cubicciotti, S. M. Howard, and R. L. Jones, “The formation of iodine-induced stress corrosion cracks in zircaloys,” *J. Nucl. Mater.*, vol. 78, no. 1, pp. 2–16, Nov. 1978, doi: 10.1016/0022-3115(78)90498-1.
[30] P. Hofmann and J. Spino, “Chemical interactions between simulated fission products and zircaloy-4 at elevated temperatures, including influence on ductility

and time-to-failure," *J. Nucl. Mater.*, vol. 102, no. 1, pp. 117–134, Nov. 1981, doi: 10.1016/0022-3115(81)90552-3.
[31] S. SHIMADA, T. MATSUURA, and M. NAGAI, "Stress Corrosion Cracking of Zircaloy-2 by Metal Iodides," *J. Nucl. Sci. Technol.*, vol. 20, no. 7, pp. 593–602, Jul. 1983, doi: 10.1080/18811248.1983.9733436.
[32] B. Cox, B. A. Surette, and J. C. Wood, in *Proc. Conf. on Environmental Degradation of Engineering Materials in Aggressive Environments, Virginia Polytechnic Institute and State University, Blacksburg, VA*, 1981, p. 193.
[33] K. Une, "Influences of cesium and cesium oxide on iodine stress corrosion cracking of Zircaloy-2 in out-of-pile and in-pile conditions," *J. Nucl. Mater.*, vol. 87, no. 1, pp. 207–210, Nov. 1979, doi: 10.1016/0022-3115(79)90142-9.
[34] W. T. Grubb, "Cadmium metal embrittlement of Zircaloy-2," *Nature*, vol. 265, no. 5589, Art. no. 5589, Jan. 1977, doi: 10.1038/265036a0.
[35] S. Beguin, "PCI-RELATED CONSTRAINTS ON EDF PWRS AND ASSOCIATED CHALLENGES," in *Pellet-clad Interaction in Water Reactor Fuels*, Aix-en-Provence, France, Mar. 2004, pp. 54-.
[36] P. Permezel, P. Pupier, and N. Wackel, "PCMI Limits on French PWR," 1994.
[37] Y. TSUKUDA, "Performance of advanced fuel materials for high burnup," *ENS TOPFUEL 03 Wurzburg Ger. March 16-19 2003*, 2003, Accessed: Feb. 07, 2021. [Online]. Available: https://ci.nii.ac.jp/naid/10017955762/
[38] A. Peakman, B. Merk, and K. Hesketh, "The Potential of Pressurised Water Reactors to Provide Flexible Response in Future Electricity Grids," *Energies*, vol. 13, no. 4, p. 941, Feb. 2020, doi: 10.3390/en13040941.
[39] M. R. Wenman, "Nuclear Materials."
[40] S. Beguin, "PCI-related Constraints on EDF PWRs and Associated Challenges," Aix-en-Provence, Mar. 2004, pp. 53–58.
[41] D. G. Franklin, "Economic Impact of Nuclear Core Materials Limitations," *Nucl. Technol.*, vol. 55, no. 3, pp. 607–616, Dec. 1981, doi: 10.13182/NT81-A32806.
[42] R. Loisel, V. Alexeeva, A. Zucker, and D. Shropshire, "Load-following with nuclear power: Market effects and welfare implications," *Prog. Nucl. Energy*, vol. 109, pp. 280–292, Nov. 2018, doi: 10.1016/j.pnucene.2018.08.011.
[43] J. ARBORELIUS *et al.*, "Advanced Doped UO2 Pellets in LWR Applications," *J. Nucl. Sci. Technol.*, vol. 43, no. 9, pp. 967–976, Sep. 2006, doi: 10.1080/18811248.2006.9711184.
[44] G. Marsh, G. A. Wood, and C. P. Perkins, "Niobia-doped UO_2 fuel manufacturing experience at British nuclear fuels Ltd," Art. no. IAEA-TECDOC--1036, 1998, Accessed: Apr. 22, 2021. [Online]. Available: http://inis.iaea.org/Search/search.aspx?orig_q=RN:29054743
[45] K. Sik Kim, K. Woo Song, J. Ho Yang, and Y. Ho Jung, "Effect of Sintering Gas on the Grain Size of UO2 Pellets Derived from Different Powder Routes," Brussles, Belgium, 2003.
[46] V. Peres *et al.*, "High temperature chromium volatilization from Cr2O3 powder and Cr2O3-doped UO2 pellets in reducing atmospheres," *J. Nucl. Mater.*, vol. 423, no. 1, pp. 93–101, Apr. 2012, doi: 10.1016/j.jnucmat.2012.01.001.
[47] M. L. Fullarton *et al.*, "Structure, properties and formation of PuCrO 3 and PuAlO 3 of relevance to doped nuclear fuels," *J. Mater. Chem. A*, vol. 1, no. 46, pp. 14633–14640, 2013, doi: 10.1039/C3TA12782F.

[48] K. A. Gamble and M. W. D. Cooper, “Multiscale Modeling of Cr2O3-doped UO2 Creep and Fracture,” Idaho National Lab. (INL), Idaho Falls, ID (United States), INL/EXT-21-64733-Rev000, Sep. 2021. doi: 10.2172/1826371.
[49] R. Jayaraj and C. Ganguly, “Recent Developments in Design and Manufacture of Uranium Dioxide Fuel Pellets for PHWRs in India.,” Oct. 2003.
[50] C. Cossé, E.-D.-D.-C. Flamanville, F. Jolivel, and M. Berger, “ENRICHED BORIC ACID AS AN OPTIMIZED NEUTRON ABSORBER IN THE EPR PRIMARY COOLANT,” p. 25.
[51] P. A. Klein, J. W. Foulk, E. P. Chen, S. A. Wimmer, and H. J. Gao, “Physics-based modeling of brittle fracture: cohesive formulations and the application of meshfree methods,” *Theor. Appl. Fract. Mech.*, vol. 37, no. 1, pp. 99–166, Dec. 2001, doi: 10.1016/S0167-8442(01)00091-X.
[52] X.-P. Xu and A. Needleman, “Numerical simulations of fast crack growth in brittle solids,” *J. Mech. Phys. Solids*, vol. 42, no. 9, pp. 1397–1434, Sep. 1994, doi: 10.1016/0022-5096(94)90003-5.
[53] T. Belytschko and T. Black, “Elastic crack growth in finite elements with minimal remeshing,” *Int J Numer Methods Eng*, vol. 45, no. 5, pp. 601–620, 1999.
[54] N. Moes, J. E. Dolbow, and T. Belytschko, “A finite element method for crack growth without remeshing,” *Int J Numer Methods Eng*, vol. 46, no. 1, pp. 131–150, 1999.
[55] P. A. Cundall and O. D. L. Strack, “A discrete numerical model for granular assemblies,” *Géotechnique*, vol. 29, no. 1, pp. 47–65, Mar. 1979, doi: 10.1680/geot.1979.29.1.47.
[56] C. O’Sullivan, “Particle-Based Discrete Element Modeling: Geomechanics Perspective,” *Int. J. Geomech.*, vol. 11, no. 6, pp. 449–464, Dec. 2011, doi: 10.1061/(ASCE)GM.1943-5622.0000024.
[57] “Simulation of tensile crack generation by three-dimensional dynamic shear rupture propagation during an earthquake - Dalguer - 2003 - Journal of Geophysical Research: Solid Earth - Wiley Online Library.” https://agupubs.onlinelibrary.wiley.com/doi/full/10.1029/2001JB001738 (accessed Apr. 25, 2021).
[58] P. A. Cundall, “A discontinuous future for numerical modelling in geomechanics?,” *Proc. Inst. Civ. Eng. - Geotech. Eng.*, vol. 149, no. 1, pp. 41–47, Jan. 2001, doi: 10.1680/geng.2001.149.1.41.
[59] C. L. Martin, L. C. R. Schneider, L. Olmos, and D. Bouvard, “Discrete element modeling of metallic powder sintering,” *Scr. Mater.*, vol. 55, no. 5, pp. 425–428, Sep. 2006, doi: 10.1016/j.scriptamat.2006.05.017.
[60] Y. Tan, D. Yang, and Y. Sheng, “Discrete element method (DEM) modeling of fracture and damage in the machining process of polycrystalline SiC,” *J. Eur. Ceram. Soc.*, vol. 29, no. 6, pp. 1029–1037, Apr. 2009, doi: 10.1016/j.jeurceramsoc.2008.07.060.
[61] I. S. Aranson, V. A. Kalatsky, and V. M. Vinokur, “Continuum Field Description of Crack Propagation,” *Phys. Rev. Lett.*, vol. 85, no. 1, pp. 118–121, Jul. 2000, doi: 10.1103/PhysRevLett.85.118.

[62] A. Karma, D. A. Kessler, and H. Levine, “Phase-Field Model of Mode III Dynamic Fracture,” *Phys. Rev. Lett.*, vol. 87, no. 4, p. 045501, Jul. 2001, doi: 10.1103/PhysRevLett.87.045501.
[63] L. O. Eastgate, J. P. Sethna, M. Rauscher, T. Cretegny, C.-S. Chen, and C. R. Myers, “Fracture in mode I using a conserved phase-field model,” *Phys. Rev. E*, vol. 65, no. 3, p. 036117, Feb. 2002, doi: 10.1103/PhysRevE.65.036117.
[64] H. Henry and H. Levine, “Dynamic Instabilities of Fracture under Biaxial Strain Using a Phase Field Model,” *Phys. Rev. Lett.*, vol. 93, no. 10, p. 105504, Sep. 2004, doi: 10.1103/PhysRevLett.93.105504.
[65] E. Martínez-Pañeda, A. Golahmar, and C. F. Niordson, “A phase field formulation for hydrogen assisted cracking,” *Comput. Methods Appl. Mech. Eng.*, vol. 342, pp. 742–761, Dec. 2018, doi: 10.1016/j.cma.2018.07.021.
[66] Hirshikesh, S. Natarajan, R. K. Annabattula, and E. Martínez-Pañeda, “Phase field modelling of crack propagation in functionally graded materials,” *Compos. Part B Eng.*, vol. 169, pp. 239–248, Jul. 2019, doi: 10.1016/j.compositesb.2019.04.003.
[67] Z. A. Wilson and C. M. Landis, “Phase-field modeling of hydraulic fracture,” *J. Mech. Phys. Solids*, vol. 96, pp. 264–290, Nov. 2016, doi: 10.1016/j.jmps.2016.07.019.
[68] Z. P. Bazant, T. Belytschko, and T.-P. Chang, “Continuum Theory for Strain-Softening,” *J. Eng. Mech.*, vol. 110, no. 12, Dec. 1984, doi: http://dx.doi.org/10.1061/(ASCE)0733-9399(1984)110:12(1666)#sthash.jUnutTYx.dpuf.
[69] Z. P. Bazant, “Why Continuum Damage is Nonlocal: Micromechanics Arguments,” *J. Eng. Mech.*, vol. 117, no. 5, May 1991, doi: http://dx.doi.org/10.1061/(ASCE)0733-9399(1991)117:5(1070).
[70] S. A. Silling, “Reformulation of elasticity theory for discontinuities and long-range forces,” *J. Mech. Phys. Solids*, vol. 48, no. 1, pp. 175–209, Jan. 2000, doi: 10.1016/S0022-5096(99)00029-0.
[71] A. Agwai, I. Guven, and E. Madenci, “Predicting crack propagation with peridynamics: a comparative study,” *Int. J. Fract.*, vol. 171, no. 1, p. 65, Oct. 2011, doi: 10.1007/s10704-011-9628-4.
[72] J.-H. Song and T. Belytschko, “Cracking node method for dynamic fracture with finite elements,” *Int J Numer Methods Eng*, vol. 77, no. 3, pp. 360–385, 2009.
[73] S. A. Silling, “Why Peridynamics?,” in *The Handbook of Peridynamic Modelling*, 2016.
[74] P. Seleson and M. L. Parks, “Links between Peridynamic and Atomistic Models,” in *Handbook of Peridynamic Modelling*, CRC Press, 2017, pp. 179–197.
[75] R. Mella and M. R. Wenman, “Modelling explicit fracture of nuclear fuel pellets using peridynamics,” *J. Nucl. Mater.*, vol. 467, Part 1, pp. 58–67, Dec. 2015, doi: 10.1016/j.jnucmat.2015.08.037.
[76] A. Javili, R. Morasata, E. Oterkus, and S. Oterkus, “Peridynamics review:,” *Math. Mech. Solids*, Oct. 2018, doi: 10.1177/1081286518803411.
[77] S. F. Henke and S. Shanbhag, “Mesh sensitivity in peridynamic simulations,” *Comput. Phys. Commun.*, vol. 185, no. 1, pp. 181–193, Jan. 2014, doi: 10.1016/j.cpc.2013.09.010.

[78] R. Beckmann, R. Mella, and M. R. Wenman, “Mesh and timestep sensitivity of fracture from thermal strains using peridynamics implemented in Abaqus,” *Comput. Methods Appl. Mech. Eng.*, vol. 263, pp. 71–80, Aug. 2013, doi: 10.1016/j.cma.2013.05.001.
[79] J. N. Israelachvili, *Intermolecular and Surface Forces*, 1st ed. 1992.
[80] M. Ramulu, A. S. Kobayashi, B. S. J. Kang, and D. B. Barker, “Further studies on dynamic crack branching,” *Exp. Mech.*, vol. 23, no. 4, pp. 431–437, Dec. 1983, doi: 10.1007/BF02330060.
[81] S. A. Silling, “Introduction to Peridynamics,” in *Handbook of peridynamic modellling*, 2016.
[82] A. A. Griffith, “The Phenomena of Rupture and Flow in Solids,” *Philos. Trans. R. Soc. Lond. Ser. Contain. Pap. Math. Phys. Character*, vol. 221, pp. 163–198, 1921.
[83] J. T. Foster, S. A. Silling, and W. Chen, “AN ENERGY BASED FAILURE CRITERION FOR USE WITH PERIDYNAMIC STATES,” *Int. J. Multiscale Comput. Eng.*, vol. 9, no. 6, 2011, doi: 10.1615/IntJMultCompEng.2011002407.
[84] S. A. Silling, “- Dynamic fracture modeling with a meshfree peridynamic code,” in *Computational Fluid and Solid Mechanics 2003*, K. J. Bathe, Ed. Oxford: Elsevier Science Ltd, 2003, pp. 641–644. doi: 10.1016/B978-008044046-0.50157-3.
[85] B. Kilic and E. Madenci, “Prediction of crack paths in a quenched glass plate by using peridynamic theory,” *Int. J. Fract.*, vol. 156, no. 2, pp. 165–177, Apr. 2009, doi: 10.1007/s10704-009-9355-2.
[86] J. Lee and J.-W. Hong, “Dynamic crack branching and curving in brittle polymers,” *Int. J. Solids Struct.*, vol. 100–101, pp. 332–340, Dec. 2016, doi: 10.1016/j.ijsolstr.2016.09.002.
[87] F. Bobaru, “Influence of van der Waals forces on increasing the strength and toughness in dynamic fracture of nanofibre networks: a peridynamic approach,” *Model. Simul. Mater. Sci. Eng.*, vol. 15, no. 5, pp. 397–417, Jun. 2007, doi: 10.1088/0965-0393/15/5/002.
[88] D. Huang, G. Lu, and Y. Liu, “Nonlocal Peridynamic Modeling and Simulation on Crack Propagation in Concrete Structures,” *Mathematical Problems in Engineering*, 2015. https://www.hindawi.com/journals/mpe/2015/858723/ (accessed Apr. 09, 2020).
[89] W. Hu, Y. D. Ha, and F. Bobaru, “Peridynamic model for dynamic fracture in unidirectional fiber-reinforced composites,” *Comput. Methods Appl. Mech. Eng.*, vol. 217–220, pp. 247–261, Apr. 2012, doi: 10.1016/j.cma.2012.01.016.
[90] M. Ghajari, L. Iannucci, and P. Curtis, “A peridynamic material model for the analysis of dynamic crack propagation in orthotropic media,” *Comput. Methods Appl. Mech. Eng.*, vol. 276, pp. 431–452, Jul. 2014, doi: 10.1016/j.cma.2014.04.002.
[91] G. Zhang, Q. Le, A. Loghin, A. Subramaniyan, and F. Bobaru, “Validation of a peridynamic model for fatigue cracking,” *Eng. Fract. Mech.*, vol. 162, pp. 76–94, Aug. 2016, doi: 10.1016/j.engfracmech.2016.05.008.
[92] Z. Cheng, G. Zhang, Y. Wang, and F. Bobaru, “A peridynamic model for dynamic fracture in functionally graded materials,” *Compos. Struct.*, vol. 133, pp. 529–546, Dec. 2015, doi: 10.1016/j.compstruct.2015.07.047.

[93] Z. Chen, S. Niazi, G. Zhang, and F. Bobaru, “Peridynamic Functionally Graded and Porous Materials: Modeling Fracture and Damage,” in *Handbook of Nonlocal Continuum Mechanics for Materials and Structures*, G. Z. Voyiadjis, Ed. Cham: Springer International Publishing, 2017, pp. 1–35. doi: 10.1007/978-3-319-22977-5_36-1.
[94] D. De Meo, N. Zhu, and E. Oterkus, “Peridynamic Modeling of Granular Fracture in Polycrystalline Materials,” *J. Eng. Mater. Technol.*, vol. 138, no. 4, Oct. 2016, doi: 10.1115/1.4033634.
[95] J. Lee, Y. D. Ha, and J.-W. Hong, “Crack coalescence morphology in rock-like material under compression,” *Int. J. Fract.*, vol. 203, no. 1, pp. 211–236, Jan. 2017, doi: 10.1007/s10704-016-0138-2.
[96] Y. D. Ha, J. Lee, and J.-W. Hong, “Fracturing patterns of rock-like materials in compression captured with peridynamics,” *Eng. Fract. Mech.*, vol. 144, pp. 176–193, Aug. 2015, doi: 10.1016/j.engfracmech.2015.06.064.
[97] Y. Wang, X. Zhou, and X. Xu, “Numerical simulation of propagation and coalescence of flaws in rock materials under compressive loads using the extended non-ordinary state-based peridynamics,” *Eng. Fract. Mech.*, vol. 163, pp. 248–273, Sep. 2016, doi: 10.1016/j.engfracmech.2016.06.013.
[98] D. Huang, G. Lu, and P. Qiao, “An improved peridynamic approach for quasi-static elastic deformation and brittle fracture analysis,” *Int. J. Mech. Sci.*, vol. 94–95, pp. 111–122, May 2015, doi: 10.1016/j.ijmecsci.2015.02.018.
[99] S. A. Silling, O. Weckner, E. Askari, and F. Bobaru, “Crack nucleation in a peridynamic solid,” *Int. J. Fract.*, vol. 162, no. 1, pp. 219–227, Mar. 2010, doi: 10.1007/s10704-010-9447-z.
[100] Y. D. Ha and F. Bobaru, “Studies of dynamic crack propagation and crack branching with peridynamics,” *Int. J. Fract.*, vol. 162, no. 1–2, pp. 229–244, Jan. 2010, doi: 10.1007/s10704-010-9442-4.
[101] F. Bobaru and W. Hu, “The Meaning, Selection, and Use of the Peridynamic Horizon and its Relation to Crack Branching in Brittle Materials,” *Int. J. Fract.*, vol. 176, no. 2, pp. 215–222, Aug. 2012, doi: 10.1007/s10704-012-9725-z.
[102] D. Dipasquale, M. Zaccariotto, and U. Galvanetto, “Crack propagation with adaptive grid refinement in 2D peridynamics,” *Int. J. Fract.*, vol. 190, no. 1, pp. 1–22, Nov. 2014, doi: 10.1007/s10704-014-9970-4.
[103] Y. Zhang, H. Deng, J. Deng, C. Liu, and S. Yu, “Peridynamic simulation of crack propagation of non-homogeneous brittle rock-like materials,” *Theor. Appl. Fract. Mech.*, vol. 106, p. 102438, Apr. 2020, doi: 10.1016/j.tafmec.2019.102438.
[104] Y. Wang, X. Zhou, and Y. Shou, “The modeling of crack propagation and coalescence in rocks under uniaxial compression using the novel conjugated bond-based peridynamics,” *Int. J. Mech. Sci.*, vol. 128–129, pp. 614–643, Aug. 2017, doi: 10.1016/j.ijmecsci.2017.05.019.
[105] S. Nayak, R. Ravinder, N. M. A. Krishnan, and S. Das, “A Peridynamics-Based Micromechanical Modeling Approach for Random Heterogeneous Structural Materials,” *Materials*, vol. 13, no. 6, Art. no. 6, Jan. 2020, doi: 10.3390/ma13061298.
[106] N. Blanc, X. Frank, C. Mayer-Laigle, F. Radjaï, and J.-Y. Delenne, “Peridynamics simulation of the comminution of particles containing

microcraks," *EPJ Web Conf.*, vol. 140, p. 07018, 2017, doi: 10.1051/epjconf/201714007018.
[107] S. Casolo and V. Diana, "Modelling laminated glass beam failure via stochastic rigid body-spring model and bond-based peridynamics," *Eng. Fract. Mech.*, vol. 190, pp. 331–346, Mar. 2018, doi: 10.1016/j.engfracmech.2017.12.028.
[108] R. W. Macek and S. A. Silling, "Peridynamics via finite element analysis," *Finite Elem. Anal. Des.*, vol. 43, no. 15, pp. 1169–1178, Nov. 2007, doi: 10.1016/j.finel.2007.08.012.
[109] P. Lall, S. Shantaram, and D. Panchagade, "Peridynamic-models using finite elements for shock and vibration reliability of leadfree electronics," in *2010 12th IEEE Intersociety Conference on Thermal and Thermomechanical Phenomena in Electronic Systems*, Jun. 2010, pp. 1–12. doi: 10.1109/ITHERM.2010.5501274.
[110] W. Gerstle, N. Sau, and S. Silling, "Peridynamic modeling of concrete structures," *Nucl. Eng. Des.*, vol. 237, no. 12, pp. 1250–1258, Jul. 2007, doi: 10.1016/j.nucengdes.2006.10.002.
[111] X. Chen and M. Gunzburger, "Continuous and discontinuous finite element methods for a peridynamics model of mechanics," *Comput. Methods Appl. Mech. Eng.*, vol. 200, no. 9–12, pp. 1237–1250, Feb. 2011, doi: 10.1016/j.cma.2010.10.014.
[112] Q. Du, L. Tian, and X. Zhao, "A Convergent Adaptive Finite Element Algorithm for Nonlocal Diffusion and Peridynamic Models," *SIAM J. Numer. Anal.*, vol. 51, no. 2, pp. 1211–1234, Jan. 2013, doi: 10.1137/120871638.
[113] T. Ni, Q. Zhu, L.-Y. Zhao, and P.-F. Li, "Peridynamic simulation of fracture in quasi brittle solids using irregular finite element mesh," *Eng. Fract. Mech.*, vol. 188, pp. 320–343, Feb. 2018, doi: 10.1016/j.engfracmech.2017.08.028.
[114] D. J. Littlewood, "Simulation of Dynamic Fracture Using Peridynamics, Finite Element Modeling, and Contact," Apr. 2012, pp. 209–217. doi: 10.1115/IMECE2010-40621.
[115] J. Lee, W. Liu, and J.-W. Hong, "Impact fracture analysis enhanced by contact of peridynamic and finite element formulations," *Int. J. Impact Eng.*, vol. 87, pp. 108–119, Jan. 2016, doi: 10.1016/j.ijimpeng.2015.06.012.
[116] W. Liu and J.-W. Hong, "A coupling approach of discretized peridynamics with finite element method," *Comput. Methods Appl. Mech. Eng.*, vol. 245–246, pp. 163–175, Oct. 2012, doi: 10.1016/j.cma.2012.07.006.
[117] B. Kilic and E. Madenci, "Coupling of peridynamic theory and the finite element method," *J. Mech. Mater. Struct.*, vol. 5, no. 5, pp. 707–733, Dec. 2010, doi: 10.2140/jomms.2010.5.707.
[118] E. Oterkus, E. Madenci, O. Weckner, S. Silling, P. Bogert, and A. Tessler, "Combined finite element and peridynamic analyses for predicting failure in a stiffened composite curved panel with a central slot," *Compos. Struct.*, vol. 94, no. 3, pp. 839–850, Feb. 2012, doi: 10.1016/j.compstruct.2011.07.019.
[119] Y. H. Bie, X. Y. Cui, and Z. C. Li, "A coupling approach of state-based peridynamics with node-based smoothed finite element method," *Comput. Methods Appl. Mech. Eng.*, vol. 331, pp. 675–700, Apr. 2018, doi: 10.1016/j.cma.2017.11.022.

[120] K. Ito, Y. Wakashima, and M. Oguma, “Pellet compliance model based on out-of-pile simulation,” *Nucl. Eng. Des.*, vol. 56, no. 1, pp. 117–122, Feb. 1980, doi: 10.1016/0029-5493(80)90175-2.
[121] V. Z. Jankus and R. W. Weeks, “LIFE-II - A computer analysis of fast-reactor fuel-element behavior as a function of reactor operating history,” *Nucl. Eng. Des.*, vol. 18, no. 1, pp. 83–96, 1972, doi: 10.1016/0029-5493(72)90038-6.
[122] G. Rossiter, “Understanding and Modelling Fuel Behaviour Under Irradiation,” in *Nuclear Fuel Science and Engineering*, 2012, pp. 396–424.
[123] C. Newman, G. Hansen, and D. Gaston, “Three dimensional coupled simulation of thermomechanics, heat, and oxygen diffusion in UO2 nuclear fuel rods,” *J. Nucl. Mater.*, vol. 392, no. 1, pp. 6–15, 2009, doi: 10.1016/j.jnucmat.2009.03.035.
[124] R. L. Williamson *et al.*, “Multidimensional multiphysics simulation of nuclear fuel behavior,” *J. Nucl. Mater.*, vol. 423, no. 1, pp. 149–163, Apr. 2012, doi: 10.1016/j.jnucmat.2012.01.012.
[125] T. Barani, D. Pizzocri, G. Pastore, L. Luzzi, and J. D. Hales, “Isotropic softening model for fuel cracking in BISON,” *Nucl. Eng. Des.*, vol. 342, pp. 257–263, Feb. 2019, doi: 10.1016/j.nucengdes.2018.12.005.
[126] K. Geelhood, W. Luscher, P. Raynaud, and I. Porter, *FRAPCON-4.0: A Computer Code for the Calculation of Steady-State, Thermal-Mechanical Behavior of Oxide Fuel Rods for High Burnup*. 2015.
[127] L. Caillot, C. Lemaignan, and B. Linet, “Pellet clad interaction in PWR fuel: analytical irradiation experiment and finite element modelling,” CEA Centre d’Etudes de Grenoble, CEA-CONF--11796, 1993. Accessed: Aug. 25, 2020. [Online]. Available: http://inis.iaea.org/Search/search.aspx?orig_q=RN:25074098
[128] C. Bernaudat, “Mechanical behaviour modelling of fractured nuclear fuel pellets,” *Nucl. Eng. Des.*, vol. 156, no. 3, pp. 373–381, Jun. 1995, doi: 10.1016/0029-5493(94)00962-X.
[129] J. Brochard *et al.*, “Modelling of Pellet Cladding Interaction in PWR fuel,” p. 8, 2001.
[130] R. L. Williamson and D. A. Knoll, “Simulating Dynamic Fracture in Oxide Fuel Pellets Using Cohesive Zone Models,” p. 10.
[131] W. Li and K. Shirvan, “Multiphysics phase-field modeling of quasi-static cracking in urania ceramic nuclear fuel,” *Ceram. Int.*, vol. 47, no. 1, pp. 793–810, Jan. 2021, doi: 10.1016/j.ceramint.2020.08.191.
[132] N. Sukumar, N. Moës, B. Moran, and T. Belytschko, “Extended finite element method for three-dimensional crack modelling,” *Int. J. Numer. Methods Eng.*, vol. 48, no. 11, pp. 1549–1570, Aug. 2000, doi: 10.1002/1097-0207(20000820)48:11<1549::AID-NME955>3.0.CO;2-A.
[133] W. Weibull, “A Statistical Distribution Function of Wide Applicability,” *ASME J. Appl. Mech.*, Sep. 1951.

Chapter 3 Methodology

In order to model fracture distributions in peridynamics for nuclear applications, it is necessary to first establish the validity of such techniques in more general cases. With that in mind, this section will outline the method used to construct one-dimensional and two-dimensional peridynamics implementations in Matlab and Abaqus respectively.

Section 3.1 outlines the method used to construct a one-dimensional peridynamics model of a tensile test, and Section 3.1.1 the Matlab code used to implement it. Section 3.2 outlines the methodology of a two-dimensional peridynamics model and Section 3.2.3 outlines the implementation of the method in Abaqus, using one-dimensional truss elements as bonds, and a combination of nodes and assigned mass for material points. The elastic behaviour of this two-dimensional model is benchmarked against finite element (FE) modelling in Section 3.2.5. Section 3.3 is a discussion of Weibull probability of failure estimators, and their biases and variances relative to each other and sample size.

3.1 One-dimensional Peridynamics

In one-dimensional bond-based peridynamics, an object is described by an array of N+1 material points, each representing a point on a one-dimensional object of length, L. Each consecutive pair of which represents a section of constant length, R (see Figure 3-1). In this way, the inter-material point spacing R is given by

$$R = \frac{L}{N} \tag{3.1}$$

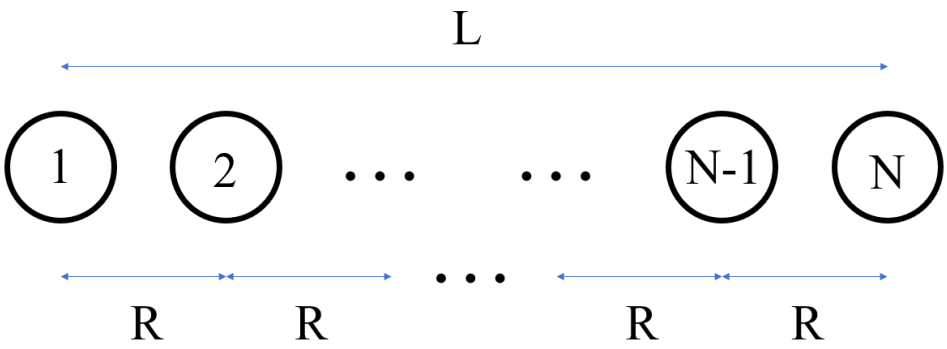

Figure 3-1 : Schematic of 1-D peridynamics material points, showing the number of material points, N, the total length of the object, L, and the inter-material point spacing, R.

The material points interact with each other by means of linear elastic bonds (shown in Figure 3-2), with each material point interacting with up to $2m$ others, where m is the ratio of, the horizon, H the maximum distance over which two material points can interact and the spacing, R, between material points. In a one-dimensional model with constant spacing between the material points, m is taken to always be an integer in this work.

$$m \equiv int\left(\frac{H}{R}\right) \tag{3.2}$$

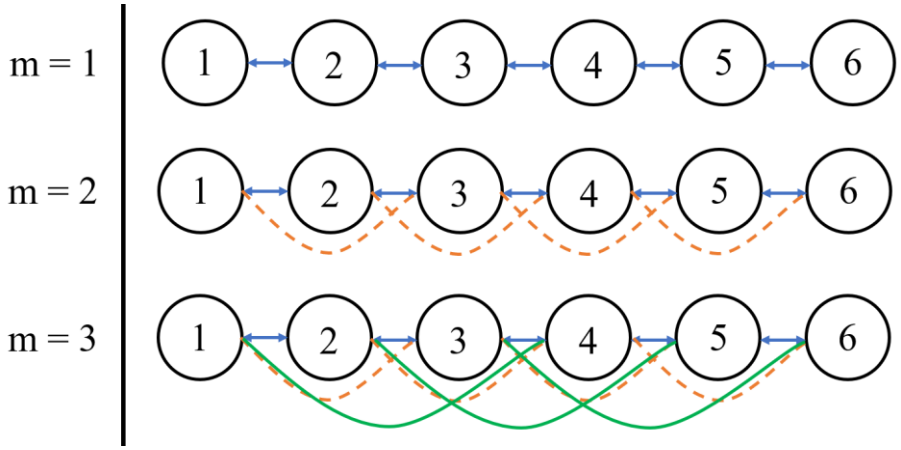

Figure 3-2: a schematic of three 1-dimensional peridynamics body with six material points, denoted by number, In each case, the bonds are denoted by coloured lines, with lines of the same colour and style being the same length.

Bond-based peridynamics is characterised by the pairwise interactions, termed bonds between material points. The behaviour of these bonds is dependent on their stretch, s. The stretch, s_{ij}, of a bond connecting two material points i and j with initial separation l_{ij}, and relative displacement η_{ij} is given by [1]

$$s_{ij} = \frac{|\eta_{ij}|}{|l_{ij}|} \tag{3.3}$$

Where relative displacement η_{ij} is defined as the distance between the two current positions of the material points x'_i and x'_j minus the distance between their original positions x_i and x_j.

$$\eta_{ij} = (x'_j - x'_i) - (x_j - x_i) \tag{3.4}$$

The micromodulus c_{ij} determines the force response of the bond to elongation, such that

$$|f_{ij}| = c_{ij} s_{ij} \tag{3.5}$$

Combining (3.2) and (3.5) the total force acting from the left on a material point F_j^L is

$$F_j^L = \sum_{i=1}^{m} c_{ij}\, s_{ij} \tag{3.6}$$

In the case that all bonds have equal micromodulus, c_0

$$F_j^L = \sum_{i=1}^{m} c_0\, s_{ij} \tag{3.7}$$

A homogeneous strain ε on the object would cause a uniform increase Δ in the distance between neighbouring material points. The increase in distance between a material point and another which was originally a distance nR, away will be now equal to $n\Delta$. Hence the total force acting on a material point by material points to its left may be written as

$$F_j^L = \sum_{i=1}^{m} c_0 \frac{\eta_{ij}}{l_{ij}} = \sum_{i-1}^{m} c_0 \frac{\varepsilon l_{ij}}{l_{ij}} \tag{3.8}$$

Or

$$F_j^L = mc_0\varepsilon \tag{3.9}$$

The force from the left is also equal to the elastic modulus of the global body, E, multiplied by the strain ε and cross sectional area of the specimen, A . Equating with (3.9) gives

$$mc_0\varepsilon = E\varepsilon A \tag{3.10}$$

And therefore the micromodulus of the bonds c_0 can be defined simply by the global elastic modulus E, the global cross-sectional area A, and the horizon ratio m.

$$c_0 = \frac{EA}{m} \tag{3.11}$$

The area of individual bonds A_0 is assigned such that the cross-sectional area of all bonds bridging a given gap between two material points is equal to the cross sectional area of the overall model, A. The number of bonds in each gap is equal to the horizon ratio m

$$A_0 = \frac{A}{m} \tag{3.12}$$

Bond-based peridynamics is well established to have the limitation that material points close to the edges of the mesh attach to fewer material points than those in the bulk. An artificial reduction in stiffness therefore occurs, since there are fewer bonds to carry the stress. This limitation was dealt with by reducing the horizon ratio of the material points close to the edges, such that they took on a higher micro-modulus c_0 as dictated by (3.11).

The horizon ratio to the left m_L and right m_R of a material point with number position a are defined as the maximum of the global horizon size m and the distance to the end of the sample in each direction:

$$m_L = \max\left[(a-1), m\right] \tag{3.13}$$

$$m_R = \max\left[((N+1)-a), m\right]. \tag{3.14}$$

3.1.1 MATLAB Implementation

This section describes the implementation of the framework outlined in Section 3.1. The model is built on the assumption that some data on the properties of a material have been collected experimentally. These data are, namely, the Weibull modulus, β, and the characteristic strength $\sigma_{0,sample}$. The volume of the sample used to gather this data V_{sample} must also be input. The purpose of the peridynamics model is to reproduce the behaviour of such a material.

Mesh refinement is controlled by selection of N+1, the number of material points in the model, with N representing the number of inter-material point separations. The value of N+1, along with the length of the specimen L, controls the inter-material point spacing R.

In order to place the model under load, the 1st material point is fixed in position

$$x_1 = 0 \tag{3.15}$$

and the N+1th node starts at position L, the length of the sample away from the origin, and is steadily moved away from the origin to increase the strain in the sample

$$x_{N+1} = L \qquad x'_{N+1} = L + \delta \tag{3.16}$$

where δ is the displacement of the N+1th node, and steadily increases. The size of the increase in δ with each step is controlled by the user. The simulation ends when either $\delta = \delta_{max}$ the maximum displacement defined by the user, or stress in the sample is detected to be zero, denoting a full fracture has occurred.

In each step, the equilibrium positions of the material points are found by solving for nodal displacement equations such that the forces acting on either side of each material point sum to zero, with the exception of the two points at either end, the displacements of which are defined by the boundary conditions in (3.15) and (3.16). This is stated more formally by (3.17).

$$a \in [2, N]: \sum_{i=-m_L}^{m_R} F_{a,i} = 0 \tag{3.17}$$

Where the force acting on the material point *a* from the right F_{a-i}^{R} is

$$F_{a-i}^{R} = \left(\frac{(x_{a+i} - x_a) - iR}{iR}\right)k = \left(\frac{c_{m_R}}{iR}\right)x_{a+i} - \left(\frac{c_{m_R}}{iR}\right)x_a - c_{m_R} \tag{3.18}$$

and the force from the left F_{a-i}^{L} is

$$F_{a-i}^{L} = \left(\frac{(x_a - x_{a-i}) - iR}{iR}\right)c = \left(\frac{c_{m_L}}{iR}\right)x_{a-i} - \left(\frac{c_{m_L}}{iR}\right)x_{a-1} - c_{m_L} \tag{3.19}$$

where c_{m_L} and c_{mR} are the relevant micromoduli given the horizon in the left and right directions respectively. Note the micromodulus is defined according to the horizon ratio, since this is variable in the bonds close to the edges of the mesh. The value of *c* is still determined by (3.11), using the correct *m* value as determined by (3.13) and (3.14). Similarly the area A_i of a bond *i* varies according to horizon ratio *m*.

Equilibrium can be found by creating a matrix containing both the boundary conditions as well as the equilibrium equations defined by $[M].[x_i] = [RHS_i]$.

The *x* co-ordinates of all nodes can be found be solving the matrix, which was assembled bond by bond, for every material point from 1 to *N*+1 using (3.15) and (3.16) for the 1st and *N*+1th material points respectively, and (3.17)-(3.19)for all material points in between.

For every increment of displacement, the coordinates of each node are determined by solving the N+1 equations. A stress can then be attributed to each bond by multiplying its strain by the elastic modulus of the material. If this value is greater than the value assigned as spring strength, the stiffness of the bond is reduced to zero.

3.2 Two-dimensional Peridynamics

The peridynamics models in this work use a square-based mesh and follow the theoretical framework outlined by Le and Bobaru [2]. To ensure that the overall peridynamics body has the same elastic modulus as the material being modelled, a conversion must be performed between the stiffness of the bonds, and the intended stiffness of the material. The stiffness of the bonds is commonly referred to as the micromodulus c_{2D}, which defines the relationship between the force F applied to a bond, and the stretch s it undergoes.

$$F = c_{2D}s \tag{3.20}$$

The stretch s is defined as

$$s = \frac{l_{deformed} - l_{undeformed}}{l_{undeformed}} \tag{3.21}$$

where l is the length of a bond. This is equivalent to strain.

Le and Bobaru [2] provide the relationship between the two-dimensional micro-modulus c_{2D} and the material stiffness E using the plate thickness τ, the inter-material point spacing δ and Poisson's ratio ν.

$$c_{2D} = \frac{12E}{\pi\tau\delta^3(1+\nu)} \tag{3.22}$$

A correction factor is required near the edges of the mesh. At the edges, peridynamics meshes have fewer bonds than in the bulk, because some longer bonds do not exist because of the lack of material points to connect to. This reduction in bonds produces an unphysical reduction in macro-level stiffness of the meshed component. In order to correct for this, Le and Bobaru [2] introduced and adjustment factor Ω_{ij} based on the ratio of the volume of a complete horizon, *Vmax* and the volume of two material points *i* and *j* (V_i and V_j respectively) which are connected by a given bond.

$$\Omega_{ij} \equiv \frac{2V_{max}}{V_i + V_j} \tag{3.23}$$

The implementation of the micromodulus and edge correction factor in the Abaqus peridynamics framework is outlined in Section 3.2.3.1.

3.2.1 Bond failure

Fracture in two-dimensional peridynamics is caused by cascading bond failure. When a bond fails, its stress is redistributed into the bonds around it, causing some of them to fail, and so on. Bonds in this formulation were considered to break above a certain strain, above which a damage parameter ϕ is permanently applied. If the strain ε at a given time t' is less than the assigned fracture strain $\varepsilon_{failure}$ and has been since the start of the simulation, then the bond is considered unbroken, and the damage parameter remains at zero. Otherwise, when the failure stress is exceeded by a bond, the damage parameter is set to 0.999, signifying a broken bond for the rest of the simulation.

$$\phi \begin{cases} = 0, & \text{if } \varepsilon(t') < \varepsilon_{failure} \quad \forall 0 \leq t' \\ = 0.999 & \text{otherwise} \end{cases} \tag{3.24}$$

The damage parameter ϕ was not assigned to 1, so as to preserve a small amount of the stiffness of the bonds. The value 0.999 was selected so as to be as close to 1 as possible without allowing fragments which became entirely separated from fixed nodes to move freely, which would needlessly increase computational expense. The remaining stiffness in the bonds was 0.1% of the original stiffness, and the effect of this on the model behaviour was considered low enough to be neglected.

This stiffness degradation was implemented in Abaqus through the ductile damage model, and is shown schematically in Figure 3-3. In order to define this stress-strain response in Abaqus, four values are needed:

- σ_0: The stress at which failure occurs.
- ε_1 & σ_1: Arbitrary stress and strain values > σ_0 and ε_0, but with the same ratio. This ensures that while undergoing the very small amount of plastic strain, the elastic modulus of the bond remains the same.
- δ: an arbitrarily small value (we used 1.0×10^{-15}) defining the amount of plastic damage that is required to totally damage the bond. The size of this value is greatly exaggerated in Figure 3-3.

These values are input to Abaqus using the `*PLASTIC` keyword.

When in compression, the user defined field subroutine sets a field variable such that the fracture strain is equal to 10^{10}, and fracture does not occur.

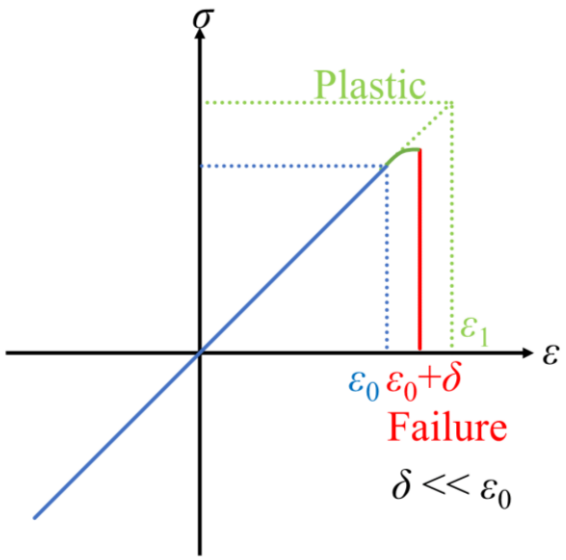

Figure 3-3 A schematic of the stress-strain graph of the ductile damage model. Reproduced from [3]

3.2.2 Inertial Response

Inertia is an important phenomenon in fracture. The motion of material either side of a crack can contribute to the stresses at the crack tip. Traditionally in peridynamics, mass is assigned to material points, and bonds are massless, acting only to transmit force. Abaqus requires that truss elements are assigned a density, and setting it too low can lead to instabilities. For this reason, 1% of the mass of the overall Abaqus model is shared between all bonds, and the remaining 99% is assigned to the material points through the means of the `*MASS` keyword. Assigning mass to material points is a simple matter of determining 99% of the mass of the object to be modelled, and dividing by the number of material points present in the model. Mass is assigned to the bonds through density, so it is important to note that the bonds are actually truss elements with length l_i and cross-sectional area A_{truss}. From this, a volume can be calculated for all n bonds. Determining the correct truss density ρ_{truss} is then a simple matter of dividing the intended mass of the bonds (equivalent to 1% of the mass of the object m_{object}) by this volume.

$$\rho_{truss} \approx \frac{0.01 m_{object}}{\sum_{i=1}^{n} (l_i)\, A_{truss}} \tag{3.25}$$

It is important to note that this cross-section and volume do not represent the cross-section and volume of the overall model. It is simply a requirement of Abaqus to assign this cross-section.

3.2.3 Abaqus Implementation

The two-dimensional implementation of peridynamics is performed using Abaqus, a commercial finite element (FE) code. Bonds are represented by one-dimensional linear elastic truss elements, and material points by nodes. This setup allows the use of some advanced features of Abaqus, such as variable time incrementation, but also necessitated some consideration as to how these best to recreate the properties of a material. For example, in classical peridynamics, bonds are purely one-dimensional, and so have no cross-sectional area. In Abaqus, it is required to define the cross-sectional area of truss elements. The difference in nomenclature between Abaqus and peridynamics is is outlined in Figure 3-4.

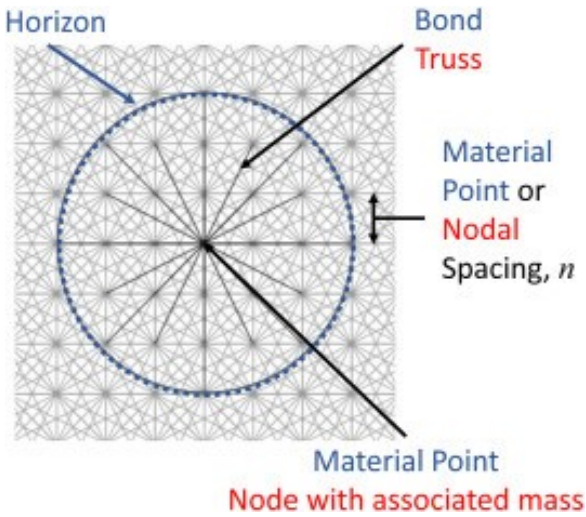

Figure 3-4 A schematic of a peridynamics mesh, showing the different nomenclature for peridynamics (blue) and Abaqus (red). Reproduced from Figure 1, [4].

3.2.3.1 Elastic Behaviour

The elastic behaviour of the truss elements is controlled by their elastic modulus E_{Truss}, which is the ratio of the induced stress σ, to a given strain ε

$$E_{Truss} = \frac{\sigma}{\varepsilon} \tag{3.26}$$

Where ε_{Truss} is defined as the ratio of the extension of the truss, η_{Truss}, to the original length of the truss, l_{Truss}

$$\varepsilon_{Truss} = \frac{\eta_{Truss}}{l_{Truss}} \tag{3.27}$$

and is therefore equivalent to the peridynamic stretch s.

$$\varepsilon_{Truss} = s \tag{3.28}$$

Typically in peridynamics, bonds are one dimensional, but Abaqus requires that the truss elements used to represent them are assigned a cross-sectional area for the purposes of calculating stress. The stress in the truss element is given by the force exerted on the truss, F, divided by its cross sectional area, A_{truss}

$$\sigma_{Truss} = \frac{F}{A_{truss}}. \tag{3.29}$$

The area of the truss is set to the product of plate thickness τ and the material point spacing d.

$$A_{truss} = \tau\, d \tag{3.30}$$

The plate thickness is set equal to the material point spacing such that

$$A_{truss} = d^2 \tag{3.31}$$

Substituting (3.26) into (3.29) and rearranging gives:

$$F = E_{truss} A \varepsilon \tag{3.32}$$

And comparing with (3.20) yields

$$E_{truss} = \frac{c}{A} \tag{3.33}$$

Given the equivalence between s and ε_{Truss} outlined in (3.28). A correction factor, λ for converting macroscopic material elastic modulus to truss elastic modulus can therefore be defined by the ratio of the stiffness in the trusses, E_{truss}, to the stiffness of the material, E_{mat}.

$$\lambda \equiv \frac{E_{truss}}{E_{mat}} \tag{3.34}$$

Such that:

$$\lambda = \frac{12}{\pi \tau \delta^3 (1 + \upsilon)} \tag{3.35}$$

The correction factor as described in (3.35) is in SI units. The Abaqus models in this work were defined according to mm units, so the correction factor is defined in these terms in (3.36) in which m is the horizon ratio.

$$\lambda = \frac{12}{\pi A \tau m^3 (1+\upsilon)} \tag{3.36}$$

The surface stiffness correction factor for a bond connecting material points i and j was implemented in this peridynamics framework by counting the number of bonds connected to each material point, N_i and N_j and assigning bonds an approximation correction factor Ω_{ij}. This approximation is based on the ratio of the average number of bonds connected to material points i and j to the maximum number of bonds connected to any material point N_{max}.

$$\Omega_{ij} = \frac{2V_{max}}{(V_i + V_j)} \approx \frac{2N_{max}}{N_i + N_j} \tag{3.37}$$

These factors are applied in Abaqus through the means of field variables. In a user defined field subroutine, each truss element is assigned a field variable equal to the product of λ_{ij} and Ω_{ij}. In the Abaqus input file, the materials elastic behaviour is defined by the `*ELASTIC` keyword. Using dependencies, the elastic modulus of the truss elements is set to appropriate values. The efficacy of these correction factors in recreating intended elastic properties is assessed in Section 3.2.5.

3.2.4 Abaqus Input Files

The Abaqus input files were written with the use of a FORTRAN preprocessor and the *INCLUDE keyword. In this way, the FORTRAN code wrote text files that were then introduced to the simulation via the Abaqus input file. This section will outline the files included in this way, and the method by which they were created.

The fundamental elements of the peridynamics mesh are the bonds and material points, and so these are defined first in the Abaqus input files by way of the *NODE and *Element keywords. The peridynamics mesh was written using a preprocessor, written in FORTRAN, in which the user first defined the size of the space in which the mesh would exist, before setting an inter-material point spacing. A two-dimensional matrix is then written with the *x* co-ordinates, *y* co-ordinates and Abaqus node label of each material point, with locations set according to a square mesh filling the defined space. Material points were then removed from this mesh in order to form the shape desired for the simulation. The revised list is then passed to the *NODE keyword in the Abaqus input file.

```
*NODE, Nset=ALL
**Node Number,  x coordinate,    y coordinate
100000001,      0.1,             0
100000002,      0.2,             0
100000003,      0.3,             0
…               …                …
```

Bonds are inserted into the mesh by iteratively checking the distance between each combination of material points. In the case that the distance is less than the horizon size, the label of the two Abaqus nodes and a label for the Abaqus truss element are written to a list. In order to avoid doubly connecting pairs of material points, a bond is only inserted if the second node label is greater than the first. This process occurs only in the pre-processor, bonds are not added during the simulation.

```
*ELEMENT, type=T2D2T Elset=allTrusses
**Element Number,  Node Label i  Node Label j
200000001,         100000001,    100000002
200000002,         100000001,    100000003
200000003,         100000002,    100000003
…                  …             …
```

Mass is assigned to nodes by way the creation of a set of mass elements, using the *ELEMENT keyword. This is followed by a two column list consisting of a label for each mass element, and the label for the node to which it is to be attached.

```
*ELEMENT, type=MASS elset=mass_elements
**Mass Element Number,   Truss Element Number
200000001,               100000001,
200000002,               100000002,
200000003,               100000002,
…                        …
```

The *MASS keyword is then used to assign the correct amount of mass to each mass element, as determined by the method in Section 3.2.2.

```
*ELEMENT, type=MASS elset=mass_elements
**Mass per node,
1.0E-10,            0
```

Cross-sectional area is assigned to the trusses via the *SOLID SECTION keyword, requiring the name of the element set for the truss elements, and the name of the material. Beneath this is the cross-sectional area of the elements, followed by the number of integration points through the layer, set to 0.

```
*Solid Section, elset=allTrusses, material=Material-1
**Cross sectional area in mm2,  Number  of  integration  points
                                through layer
0.10000,                        0
```

Element and node sets may now be defined. The nature of these will depend on the exact nature of the simulation to be performed. Some examples would include the set of nodes to which a displacement boundary condition or force are to be applied to; the set of trusses to be used in heat conduction; or the set of nodes to which a heat flux is to be applied to. This requires the name to be applied to the set, the name of the appropriate instance, and the list of nodes or elements within the set.

The material is then defined using the *MATERIAL keyword, and the name of the material. The *CONDUCTIVITY and *SPECIFIC HEAT keywords are not used in the work in this thesis, but Abaqus requires that values are defined for these variables. The fracture of the bonds is in part controlled by the *DAMAGE INITIATION and *DAMAGE EVOLUTION keywords.

*DAMAGE INITIATION defines the amount of plastic deformation required to occur before strength degradation begins to take place. It is necessary to define the damage as ductile in order to make use of Abaqus' implicit time integration but the equivalent plastic strain at damage initiation was set to 10^{-15} in order to closely recreate a perfectly brittle stress strain curve. The remaining variables required by Abaqus, namely the stress triaxiality and strain rate were set to zero.

```
*Damage Initiation, criterion=DUCTILE
**Plastic       Stress          Strain Rate
Strain          Triaxiality,
1.0E-15,        0.,             0.
```

*DAMAGE EVOLUTION describes the process of increasing the damage variable (which then influences the stiffness of the trusses) with increasing strain. Displacement was used as the property controlling the degradation, and a table is used to define the degree of degradation and the plastic strains at which they occur.

```
*Damage Evolution, type=DISPLACEMENT, Softening=Tabular
**Damage Variable,   Plastic Strain
0.0,                 1.0e-15,
0.9999,              1e-14
0.99991,             1
```

The *ELASTIC keyword defines the stifness and poisson's ratio of the trusses, and their variation with temperature and field variables. On each line, an elastic modulus, a Poisson's ratio, a temperature and any field variables are defined. These values are defined at each integration point by the use-defined field subroutine, written in FORTRAN, then used to calculate the elastic properties of the trusses at any temperature or value of the field variables, via linear interpolation between the points defined. Field variable 1 is set to the product of the λ_{ij} and Ω_{ij} elastic modulus correction factors for each truss.

```
*Elastic, Dependencies =2
**Elastic          Poissons  Temperature,  FV1,           FV2
Modulus,           Ratio,
190000,            0.33333,  500,          0,             0
184000,            0.33333,  750,          0,             0
0.190000,          0.33333,  500,          0.0000000001,  0
0.184000,          0.33333,  750,          0.0000000001,  0
190000,            0.33333,  500,          1,             0
184000,            0.33333,  750,          1,             0
1900000000000000,  0.33333,  500,          10000000000,   0
1840000000000000,  0.33333,  750,          10000000000,   0
```

Similarly, the *PLASTIC keyword is used to define the stress at which the trusses will undergo plastic strain, triggering the ductile damage model defined by the *DAMAGE INITIATION and *DAMAGE EVOLUTION keywords. In this case, the variables defined are the stress, the plastic strain at this stress, the temperature and any field variables. The stress at onset of plastic strain is then linearly interpolated for any values of field variables and temperature not defined in this table. Field variable 2 is set to the product of field variable 1 and the failure strain passed to the subroutine.

```
*Plastic, Dependencies =2
```

```
**Yield Stress,     Plastic   Temperature,  FV   FV2
                    Strain                  1,
190000,             0.33333,  500,          0,   0
209000,             0.33333,  750,          0,   0
0.190000,           0.33333,  500,          0,   0.0000000001
0.209000,           0.33333,  750,          0,   0.0000000001
190000,             0.33333,  500,          0,   1
209000,             0.33333,  750,          0,   1
1900000000000000,   0.33333,  500,          0,   10000000000
2090000000000000,   0.33333,  750,          0,   10000000000
```

The User-Defined Field subroutine is also used to prevent failure of bonds in compression. The stress in each truss element is checked at the start of each increment, and in the case that the stress is negative (i.e. compressive) the strength of the bond is set arbitrarily higher (increased by a factor of 10^{10}) via state variable 2.

Thermal expansion is performed by comparing the starting temperature of the truss elements to the current average temperature of the nodes at either end of each truss element, and multiplying by the coefficient of thermal expansion.

Field variable 1 is set to the product of the λ_{ij} and Ω_{ij} elastic modulus correction factors. Field variable 2 is set to the product of field variable 1 and the failure strain passed to the model by the user using the mesh pre-processor. Coupled with the definition in the `*MATERIAL` keyword, this defines the failure stress of a truss element.

3.2.5 Benchmarking

Although the two-dimensional implementation of peridynamics in Abaqus is based on a theoretical footing taken from the literature [2], [5], [6], an investigation of its effectiveness in recreating simple elastic properties in a tensile test was deemed necessary, for completeness. For this section, a two-dimensional model of a tensile test was completed in both FE and peridynamics, and the results compared.

A rectangular peridynamics model with dimensions 10 mm x 2 mm; elastic modulus 180 GPa, and capacity for bond failure removed was subjected to an external strain. The material points on the right end were moved 0.15 mm over 9 s, inducing a strain of 1.5 x 10^{-4}. The material points at the left end were fixed in the *x* direction, and a line of material points making up the mid-line in the direction parallel to the strain were fixed in the *y* direction to constrain the model. The force *F* required to induce the strain was recorded in the form of the sum of the reaction forces on each node where the strain was induced. This was converted to a stress by dividing by this force the cross-sectional area of the plate allowing for the change in area induced by the strain.

$$\sigma = \frac{F}{A_{plate}(1-\varepsilon_y)^2} \tag{3.38}$$

Where A_{plate} is the original cross-sectional area of the specimen, and ε_y is the strain the direction perpendicular to the load.

This was performed for a variety of mesh spacings between 0.04 mm and 0.125 mm and horizon ratios between 2 and 4. The mesh spacings chosen were a selection of those that would result in an integer number of material points in a model of this size. The horizon ratios used were a selection of those which result in an increase in the number of bonds used in a unit cell of a bulk peridynamics material point. For example, $m = \sqrt{10}$ was used because this results in 31 bonds attached to each material point in the bulk, whereas using a horizon ratio $\sqrt{8} < m < \sqrt{10}$ would result in only 27. The resulting effective stiffness of these meshes is summarised in Table 3-1.

Table 3-1 The stifnesses in (GPa) observed in peridynamics bodies when using different horizon ratio and inter-material point spacings, with an intended value of 180 GPa

		Inter-Material Point Spacing					
		0.0400	0.0500	0.0625	0.0800	0.1000	0.1250
Horizon Ratio	2	235	235	236	237	240	242
	$\sqrt{8}$	153	153	153	155	156	157
	3	193	191	196	196	199	201
	$\sqrt{10}$	247	248	249	251	251	253
	4	180	179	181	182	183	184

When varying the mesh refinement with a consistent horizon ratio, the effective stiffness is kept reasonably constant, although there is a weak trend of increasing stiffness with decreasing refinement. The same cannot be said for varying horizon ratio with consistent mesh spacing. If only the integer values of *m* are included, there is a trend of decreasing effective stiffness with increasing horizon size. There is some evidence that the stiffness is converging on 180 GPa, but that is not clear without further increasing the horizon ratio. Increasing the size of the horizon massively increases the number of bonds in the simulation, and there is a limit on the size of the matrix able to be manipulated by the currently used software architecture that would have been violated by increasing the horizon size to 6.

Looking at the non-integer values, large variation can be seen between $m = \sqrt{8}$, $m = 3$, and $m = \sqrt{10}$. This can be attributed to a mesh discretisation effect. The number of bonds attached to a bulk material point varies with horizon ratio in a discrete manner, and the elastic modulus correction factor λ varies continuously with horizon ratio. The manner in which these two parameters vary with horizon ratio is displayed graphically in Figure 3-5. In the case of $\sqrt{8} \leq m \leq \sqrt{10}$, this disconnect leads to significant

changes in the number of bonds being corrected for by only a small change in λ, (see (3.35)) and therefore there is variation in the global stiffness.

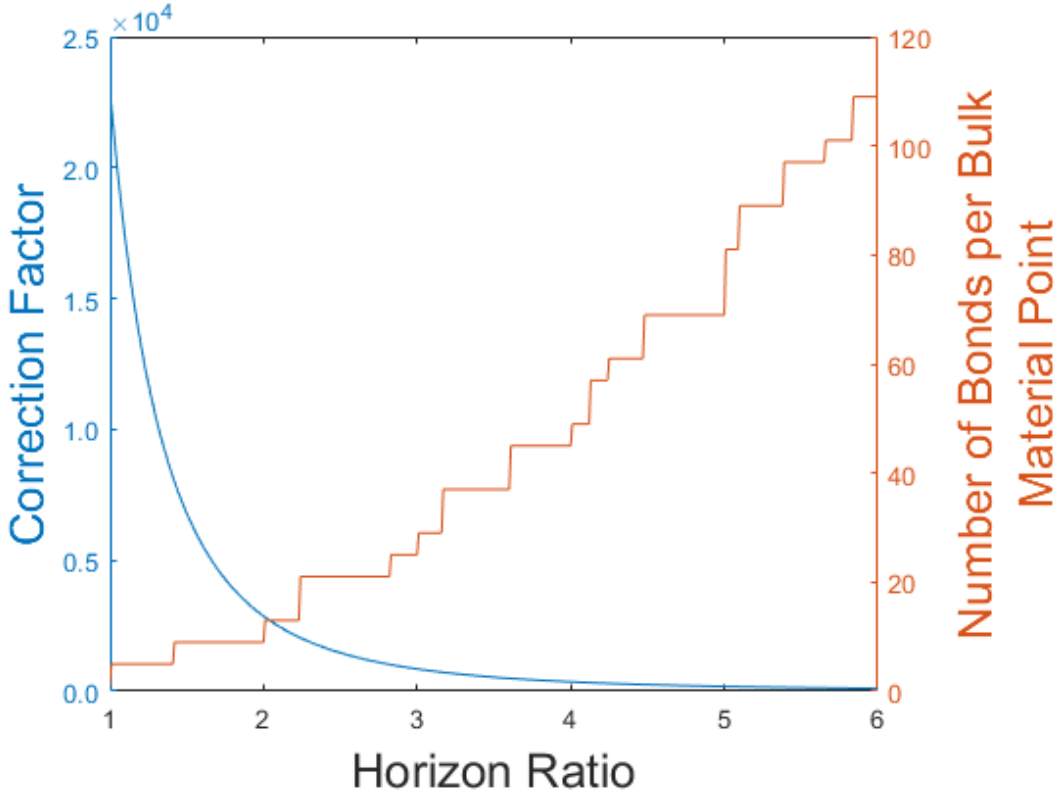

Figure 3-5 A comparison of the continuously varying correction factor, λ, and the discretely varying number of bonds per bulk material point

This leads to the notion that the most appropriate non-integer horizon ratio values to use are not in fact those that lead to the smallest error of the nature described in the previous paragraph. To test which horizon ratios may be most appropriate, the benchmarking test was re-run using a consistent mesh spacing of 0.08mm, and a variety of horizon ratios. The horizon ratios chosen were all of the square roots of integers between 9 and 16 inclusive, as well as $m = 5$. Horizon ratios $m < 3$ were excluded on the basis that such small horizons were established to be inaccurate in the first instance. These results are summarised in Table 3-2. The effective Poisson's ratio was measured as the ratio of strain in the load direction to the strain normal to the

loading direction, both across the entire specimen at the respective midpoints of the specimen. The Poisson's ratio is intended to be 1/3 since the model is in plane stress.

Table 3-2 The variation in Poisson's ratio and stiffness observed in peridynamic bodies with horizon ratios between 3 and 5.

Horizon Ratio	Poisson's Ratio	Stiffness (GPa)
3	0.341	195
$\sqrt{10}$	0.305	251
$\sqrt{11}$	0.304	221
$\sqrt{12}$	0.299	153
$\sqrt{13}$	0.389	158
$\sqrt{14}$	0.389	142
$\sqrt{15}$	0.389	127
4	0.346	189
5	0.334	191

There is a clear trend that effective stiffness increases when horizon ratio is increased so as to increase the number of bonds connected to a bulk material point ($m = 3, \sqrt{10}, \sqrt{13}, 4$) and decreasing with increasing horizon ratio in the absence of increasing bond numbers. There must be a value for $\sqrt{11} < m < \sqrt{12}$ which produces a reasonable global stiffness, but its use would be on shaky theoretical grounds, especially in the absence of an analytical method for finding it. For this reason, and given that the integer values all produce a reasonable match to the effective stiffness of the FE model of plane stress, (185 GPa) these are the values used for the Weibull experiments.

With the variation of elastic behaviour with varying mesh parameters considered, the model was tested for a variety of meshes on its fracture properties. When varying mesh parameters, the model underwent fracture exactly at a prescribed fracture strain to within 3 significant figures. It was therefore determined that the method is insensitive

to mesh variation with regards to fracture strain when a single fracture strain (i.e. no Weibull randomisation) is used.

3.3 Estimating Probability of Failure

The two-parameter Weibull cumulative probability distribution equation [7] for the probability of failure, P_f, of an object under a given stress, σ, is given by (3.39) , in which β is the Weibull modulus, and σ_0 the characteristic stress:

$$P_f = \exp\ -\left(\frac{\sigma}{\sigma_0}\right)^{\beta} \tag{3.39}$$

In chapters 4 and 5, the ability of the model to reproduce a Weibull distribution is determined by estimating the parameters β and σ_0 of Weibull distributions based on the fracture of the models. To do this, the fracture strengths of a sample of N models are ranked, and the probability of failure P_f is estimated for each rank, i. There are a number of possible ways to estimate the probability of failure based on a data points rank. Four such estimators noted by Bergman [8]

$$P_f^I = \frac{i}{\mathrm{N}+1} \tag{3.40}$$

$$P_f^{II} = \frac{i-0.5}{\mathrm{N}} \tag{3.41}$$

were both used by Trustrum and Jayalitika [9] to calculate probabilities of failure. (3.40) is termed the mean rank value [10] and (3.41) gives the average of the

probabilities of failure given by the empirical density function before and after discontinuous jump at σ_i. Other estimators discussed in [10] and later in [8] are

$$P_f^{III} = \frac{i - 0.3}{\mathrm{N} + 0.4} \tag{3.42}$$

$$P_f^{IV} = \frac{i - 3/8}{\mathrm{N} + 1/4} \tag{3.43}$$

Both [8] and [10] mention that equations (3.42) and are useful for exceptionally small sample sizes, of around 6. For sample sizes of less than 50, each of the estimators show a slight bias in both Weibull modulus β and characteristic stress σ_0 [8]. Equation (3.40) gives a greater bias in β than (3.41), with no significant difference in variance, so the latter is preferred by both [9] and [11].

These four methods were tested for their bias in β and σ_0 as well as their standard deviation at a variety of sample sizes, by generating 4000 samples of different sizes using each different estimator, and comparing the output Weibull parameters. (3.43) performs best in reducing Weibull modulus bias, and (3.40) the worst, with (3.41) and (3.42) showing opposite biases of similar magnitude (see Figure 3-6). Figure 3-7 shows that the biases in characteristic strength are all overestimates, with all but (3.40) performing similarly, with around 0.1%-0.2% bias depending on sample size. Figure 3-8 and Figure 3-9 show that the standard deviation in output Weibull modulus and characteristic strength decrease with increasing sample size, with only small differences between estimators.

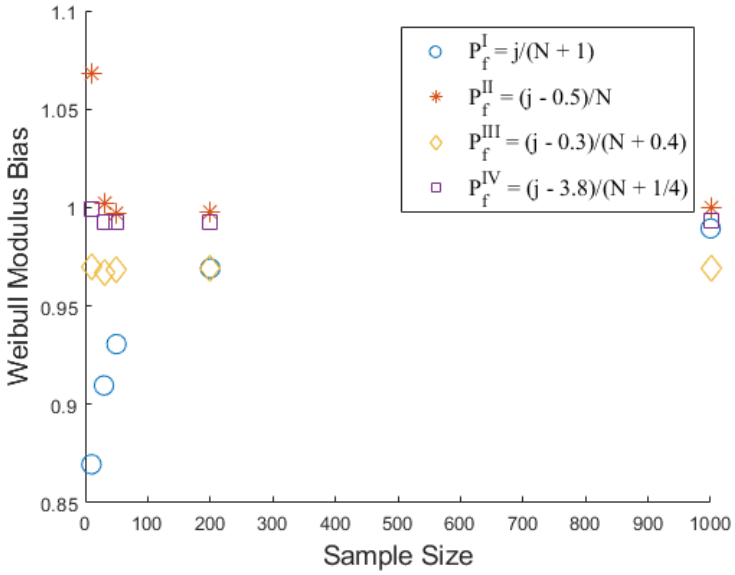

Figure 3-6 The Weibull modulus biases for each probability of failure estimator from equations (3.40-3.43) with relation to sample size, for a Weibull modulus of 6.

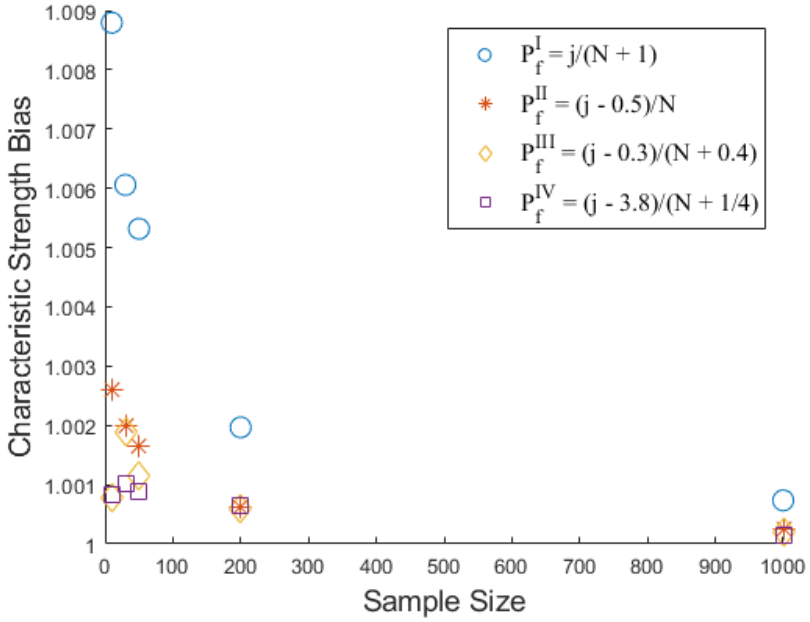

Figure 3-7 The Characteristic Strength biases for each probability of failure estimator from equations (3.40-3.43) with relation to sample size, for a Weibull modulus of 6.

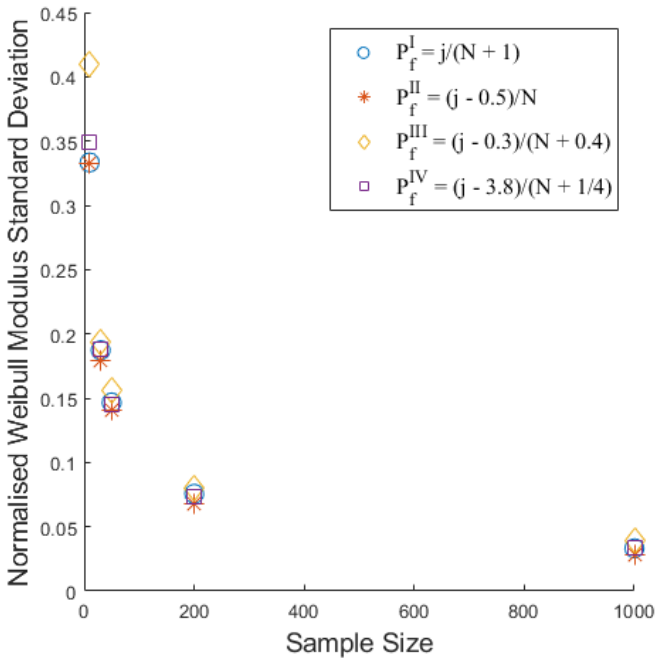

Figure 3-8 The standard deviation in Weibull modulus for each probability of failure estimator from equations (3.40-3.43) with relation to sample size, for a Weibull modulus of 6. The values are normalised according to the biases shown in Figure 3-6

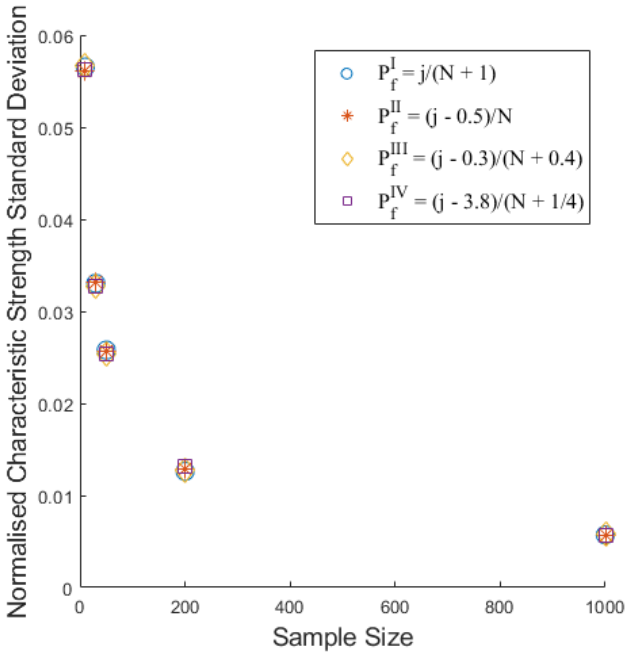

Figure 3-9 The standard deviation in Weibull modulus for each probability of failure estimator from equations (3.40-3.43) with relation to sample size, for a Weibull modulus of 6. The values are normalised according to the biases shown in Figure 3-7

Biases and variation in characteristic stress have been shown to be much smaller than those in Weibull modulus, so were neglected for the purposes of selecting an estimator

for this work. (3.43) showed almost zero bias, but came with the drawback of a slightly larger standard deviation. Since bias can be easily corrected for, but variation can not, (3.41) was chosen as the estimator for probability of failure in this work.

can re-arranged so that the equation now takes the form $y = mx + c$:

$$ln\left(ln\left(\frac{1}{1-P_f}\right)\right) = \beta\big(ln(\sigma)\big) - \beta\big(ln(\sigma_0)\big) \tag{3.44}$$

Plotting ln (ln $\left(\frac{1}{1-P_f}\right)$) against ln ($\sigma$) and performing a least-squares regression was used to determine the Weibull parameters produced by the model.

3.4 Summary

This chapter has outlined the theoretical framework under which the experiments described in chapters 4, 5 and 6 were performed, and establishes that this framework reproduces simple elastic behaviour.

3.5 References

[1] R. W. Macek and S. A. Silling, "Peridynamics via finite element analysis," *Finite Elem. Anal. Des.*, vol. 43, no. 15, pp. 1169–1178, Nov. 2007, doi: 10.1016/j.finel.2007.08.012.

[2] Q. V. Le and F. Bobaru, "Surface corrections for peridynamic models in elasticity and fracture," *Comput. Mech.*, vol. 61, no. 4, pp. 499–518, Apr. 2018, doi: 10.1007/s00466-017-1469-1.

[3] L. D. Jones, L. J. Vandeperre, T. A. Haynes, and M. R. Wenman, "Modelling of Weibull Distributions in Brittle Solids Using 2-Dimensional Peridynamics," *Procedia Struct. Integr.*, vol. 28, pp. 1856–1874, Jan. 2020, doi: 10.1016/j.prostr.2020.11.009.

[4] T. A. Haynes, D. Shepherd, and M. R. Wenman, "Preliminary modelling of crack nucleation and propagation in SiC/SiC accident-tolerant fuel during routine operational transients using peridynamics," *J. Nucl. Mater.*, vol. 540, p. 152369, Nov. 2020, doi: 10.1016/j.jnucmat.2020.152369.

[5] Y. D. Ha and F. Bobaru, “Studies of dynamic crack propagation and crack branching with peridynamics,” *Int. J. Fract.*, vol. 162, no. 1–2, pp. 229–244, Jan. 2010, doi: 10.1007/s10704-010-9442-4.
[6] S. A. Silling, “Introduction to Peridynamics,” in *Handbook of peridynamic modellling*, 2016.
[7] W. Weibull, “A Statistical Distribution Function of Wide Applicability,” *ASME J. Appl. Mech.*, Sep. 1951.
[8] B. Bergman, “On the estimation of the Weibull modulus,” *J. Mater. Sci. Lett.*, vol. 3, no. 8, pp. 689–692, Aug. 1984, doi: 10.1007/BF00719924.
[9] K. Trustrum and A. D. S. Jayalitika, *J Mater Sci*, no. 14, p. 1080, 1979.
[10] K. C. Kapur and L. R. Lamberson, “Reliability in engineering design,” *N. Y. John Wiley Sons Inc 1977 605 P*, 1977, Accessed: Mar. 09, 2021. [Online]. Available: http://adsabs.harvard.edu/abs/1977nyjw.book.....K
[11] C. A. Johnson, in *Fracture mechanics of Ceramics, Vol. 5, edited by R.C. Brandt, D. P. H. hasselman and F. F. Lange*, New York: Plenum Press, 1983, pp. 365–86.

Chapter 4 Weibull distributions Modelled in One-Dimensional Peridynamics

4.1 Introduction

The goal of this thesis is to outline a peridynamics model showing the effects of fracture strength distributions in nuclear fuel. In order to achieve that, it must first be shown that peridynamics is capable of modelling such distributions accurately. This chapter describes the problems with naively applying fracture strength distributions in peridynamics, and outlines a method for doing so accurately in one-dimension. Work using this methodology was previously published in May 2020 [1].

4.2 Methodology

One-dimensional peridynamics was implemented in MATLAB using the methodology outlined in Section 3.1. This section will describe the various attempts to recreate Weibull distributions using that framework. A total of seven implementations of Weibull distributions in one-dimensional peridynamics are shown in this work. The method for each is laid out in this section.

4.3 Cases 1-3: The Naïve Cases

Before any discussion of the correct way to implement a Weibull distribution of fracture strength in peridynamics can take place, it is important to show that the previous intuitive manner in which fracture distributions have been implemented in some work in the literature [2] is inaccurate. Case one is the simplest possible implementation of a Weibull distribution in peridynamics. The horizon ratio is set to $m = 1$, and the fracture stress of each of the bonds is randomised according to the exact Weibull parameters of the intended Weibull distribution for the whole part modelled.

To achieve this, a random number is generated between zero and one for each bond, and this value is used for that bonds probability of failure. A method for determining the bonds fracture stress based on this probability of failure value can be found in section 4.3.3.

Case two keeps the small horizon ratio, but scales the characteristic stress of the bonds in order to account for the difference in size between them and the overall part to be modelled. More information on how this scaling is calculated can be found in section 1.2.1.1. Case three tests this scaling method further, by increasing the horizon ratio to $m = 3$, a typical value used in the peridynamics literature [3]. Case 3 is the closest representation of the randomisation in the form of non-Weibull distributions in [2] and to the Weibull distributions implemented in by Casolo and Diana in [4].

4.3.1 Cases 4-7: Localisation of Failure Methods

Cases 4-7 seek to implement Weibull distributions in one-dimensional peridynamics by using the material points as the entities for which fracture stress is randomised. Since material points do not themselves undergo stress, cases 4-7 explore some possible methods of determining fracture stress for bonds, based on the random probability of failure assigned to the material points around them (see Figure 4-1). The method outlined in 0 is used to calculate a fracture stress based on this. All cases 4-7 use the size scaling method outlined in section 1.2.1.1.

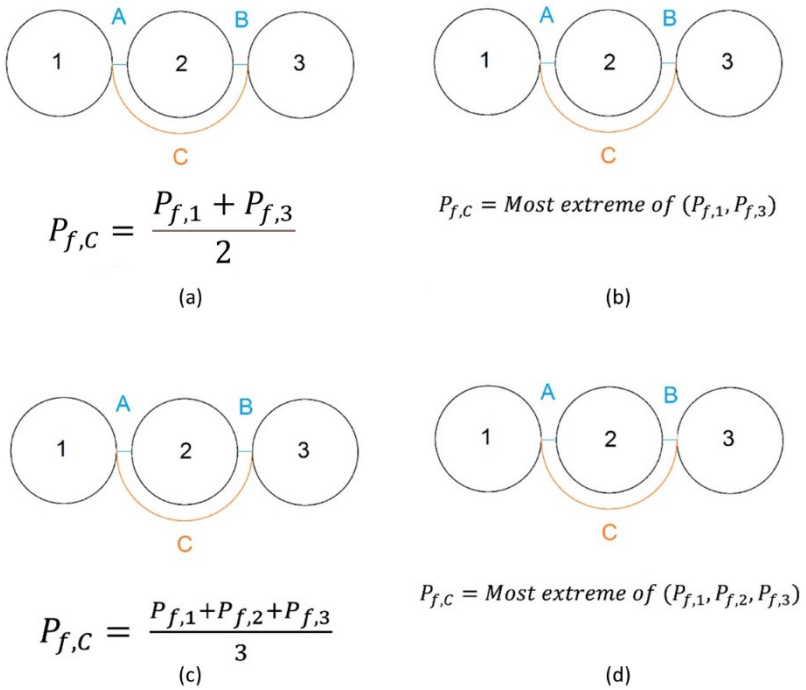

Figure 4-1 shows schematics of the various methods used to calculate bond probability of failure values based on those of the material points around them. Values 1, 2, and 3 are randomly assigned based upon the desired input Weibull distribution, and then A, B, and C are calculated based on them. The method of calculating C is shown in the equation to highlight the differences in the methods. (a) shows case 4; (b) shows case 5; (c) shows case 6; (d) shows case 7. Reproduced from figure 3 [1]

Case four uses the most basic information available with regards to a given bond in this scenario: the probability of failure values for each of the material points that make up the ends of the bond. These two values are averaged, and the resulting value is used as the probability of failure for that bond. Case 5 similarly uses an average value of the relevant material points, but includes any material point that is overlapped by the bond in question. The relevant material points to a bond connecting material point *i* to material point *j* are any which satisfy

$$x_i \leq x_{mp} \leq x_j \tag{4.1}$$

where x_i is the location along the one-dimensional model of the left-most material point connected by the bond, x_j is the location of the right-most material point connected by

the bond, and x_{mp} is the location of a third material point. More than one additional material point can be considered relevant to a given bond, depending on the bonds length. The number of relevant material points is one greater than the length of the bond in terms of R, the material point spacing.

Case 6 uses only the material points making up the ends of the bond, but instead of averaging the probabilities of failure, takes the most extreme of the two values for the bond. The "extremeness" φ of a value is defined by

$$\varphi = \left|0.5 - P_f\right| \tag{4.2}$$

meaning that the bonds tend to take on values of probability of failure either close to one, representing material that has a low fracture stress due to the presence of a large flaw, or a probability of failure close to zero, representing near flawless material.

Case 7 combines the material point selection method of case 5 with the probability of failure calculation method of case 6. Bonds take the most extreme probability of failure value of any material point they connect, and any material points in between.

4.3.2 Size Scaling

The randomness of fracture strengths described by Weibull distributions stem from the random size and orientation of the critical flaw within specimens of the material. Since smaller specimens have less volume in which to contain a large flaw, the probability of containing such a flaw is lower, and their fracture strength is, on average higher. Peridynamic bonds are by definition much smaller than the overall model which they make up, and so the characteristic fracture stress of the bonds must be higher than the characteristic stress of the overall specimen being modelled.

The manner of this increase can be derived from the two parameter Weibull distribution considering the failure stresses of the links in a chain

$$P_{link,F} = 1 - exp\left(-\left[\frac{\sigma}{\sigma_{0,link}}\right]^{\beta}\right). \tag{4.3}$$

The probability that an object will fail, P_F, is related to the probability that it will survive, P_S, by (4.4)

$$P_S = 1 - P_F \tag{4.4}$$

The probability that a single link in chain will survive, $P_{link,S}$, is found by substituting (4.3) into (4.4) to give (4.5):

$$P_{link,S} = 1 - \left[1 - e^{-\left(\sigma/\sigma_{link,0}\right)^{\beta}}\right] = e^{-\left(\sigma/\sigma_{link,0}\right)^{\beta}}. \tag{4.5}$$

A chain of N such links will only survive if all of the N links in the chain survive. The probability that the chain survives, $P_{chain,S,}$ is therefore given by (4.6):

$$P_{chain,S} = \left(P_{link,S}\right)^{N} \tag{4.6}$$

and substituting (4.5) into (4.6) gives:

$$P_{chain,S} = \left(e^{-\left(\sigma/\sigma_{link,0}\right)^{\beta}}\right)^{N} = e^{-N\left(\sigma/\sigma_{link,0}\right)^{\beta}} = e^{-\left(N^{(1/\beta)}\sigma/\sigma_{link,0}\right)^{\beta}}. \tag{4.7}$$

Using (4.4) and (4.7) gives the probability that the chain will fail, $P_{chain,F}$

$$P_{chain,F} = 1 - e^{-\left(N^{(1/\beta)}\sigma/\sigma_{link,0}\right)^{\beta}}. \tag{4.8}$$

Requiring that the probability of the failure of the chain will take the same functional form as (4.3), and making the assumption that the shape factor is an extrinsic material property and therefore invariant gives (4.9).

$$P_{chain,F} = 1 - e^{-\left(\sigma/\sigma_{chain,0}\right)^{\beta}} \tag{4.9}$$

Comparing (4.8) and (4.9) and equating the exponents enables the characteristic stress of the chain, $\sigma_{chain,0}$, to be determined as follows:

$$\sigma/\sigma_{chain,0} = N^{(1/\beta)}\sigma/\sigma_{link,0}$$

$$\sigma_{chain,0} = \frac{\sigma_{link,0}}{N^{(1/\beta)}} = \left(\frac{1}{N}\right)^{1/\beta}\sigma_{link,0}. \tag{4.10}$$

A peridynamics body with horizon ratio $m > 1$ is not a perfect analogy to a chain, since there are overlapping "links" the number of links in the chain N must be replaced with the ratio of between the volume of a peridynamics bond V_{bond} and the volume of the overall model V_{model}:

$$\sigma_{chain,0} = \left(\frac{V_{model}}{V_{bond}}\right)^{1/\beta}\sigma_{link,0}. \tag{4.11}$$

4.3.3 Calculating Fracture Stress From Probability of Failure

In all cases, it is necessary to be able to convert a probability of failure value into a fracture stress, so a derivation of that calculation is included here.

$$P_f = 1 - exp\left(-\left[\frac{\sigma}{\sigma_0}\right]^{\beta}\right) \tag{4.12}$$

Knowing that the inverse of the probability of failure P_f is the probability of survival P_s

$$P_s = 1 - P_f \tag{4.13}$$

We can write

$$P_s = exp\left(-\left[\frac{\sigma}{\sigma_0}\right]^{\beta}\right) \tag{4.14}$$

And taking the natural logarithm of both sides yields (4.15)

$$\ln(P_s) = -\left[\frac{\sigma}{\sigma_0}\right]^{\beta} \tag{4.15}$$

Taking the additive inverse of both sides

$$\ln\left(\frac{1}{P_s}\right) = \left[\frac{\sigma}{\sigma_0}\right]^{\beta} \tag{4.16}$$

Before raising each side to the power of $1/\beta$

$$\left[\ln\left(\frac{1}{P_s}\right)\right]^{\frac{1}{\beta}} = \left[\frac{\sigma}{\sigma_0}\right] \tag{4.17}$$

And finally multiplying both sides by the characteristic stress σ_0

$$\sigma = \sigma_0\left[\ln\left(\frac{1}{P_s}\right)\right]^{\frac{1}{\beta}} \tag{4.18}$$

4.3.4 Modelling Strategy

To test the models ability to recreate a given Weibull distribution, a framework of a one-dimensional model of a tensile test was constructed, with each model described by the following variables:

- The number of material points, N, and their spacing, R to describe the length of the model.
- Weibull parameters: shape parameter (or modulus), β, and characteristic strength, $\sigma_{0,sample.}$ These values define the Weibull distribution for the sample that the model is intended to recreate, i.e. obtained by testing a large number of samples.
- Probability of failure, P_f, values randomly assigned to each bond, with a uniform distribution, 0-1.
- Non-Weibull properties of the object such as its cross sectional area A_{sample} and elastic modulus, E.
- The horizon ratio, m, defined as the ratio between horizon size and material point spacing.

The values for variable that were kept consistent between cases are given in Table 4-1. This model was placed under tensile stress by moving the material point at one end in explicit increments, while keeping the material point at the other end fixed in place. Extension was increased until fracture was detected. The stress was recorded at the time of failure of the first bond, and of the overall model.

Table 4-1 Variables used in one-dimensional peridynamics simulations of tensile tests and the values which were kept consistent.

Variable	Symbol	Value	Unit
Number of Material Points per Model	N	100	N/A
Spacing Between Material Points	R	0.1	mm
Characteristic Stress of the Overall Model	$\sigma_{0,sample}$	1000	MPa
Weibull Modulus of the Overall Model	β_{sample}	6.00	N/A
Elastic Modulus	E	150	GPa
Cross Sectional Area of the Sample	A_{sample}	2	mm^2

4.4 Results

4.4.1 Cases 1-3: The 'Naïve' Cases

Case 1 (see Figure 4-2) produced data with a good fit to a Weibull curve, ($R^2 = 0.998$) but the parameters were inaccurate relative to the intended distribution. The characteristic stress (466 MPa) is, as expected, much lower than the intended 1000 MPa. The Weibull modulus was however, very accurate at 5.90 compared to the intended 6.00.

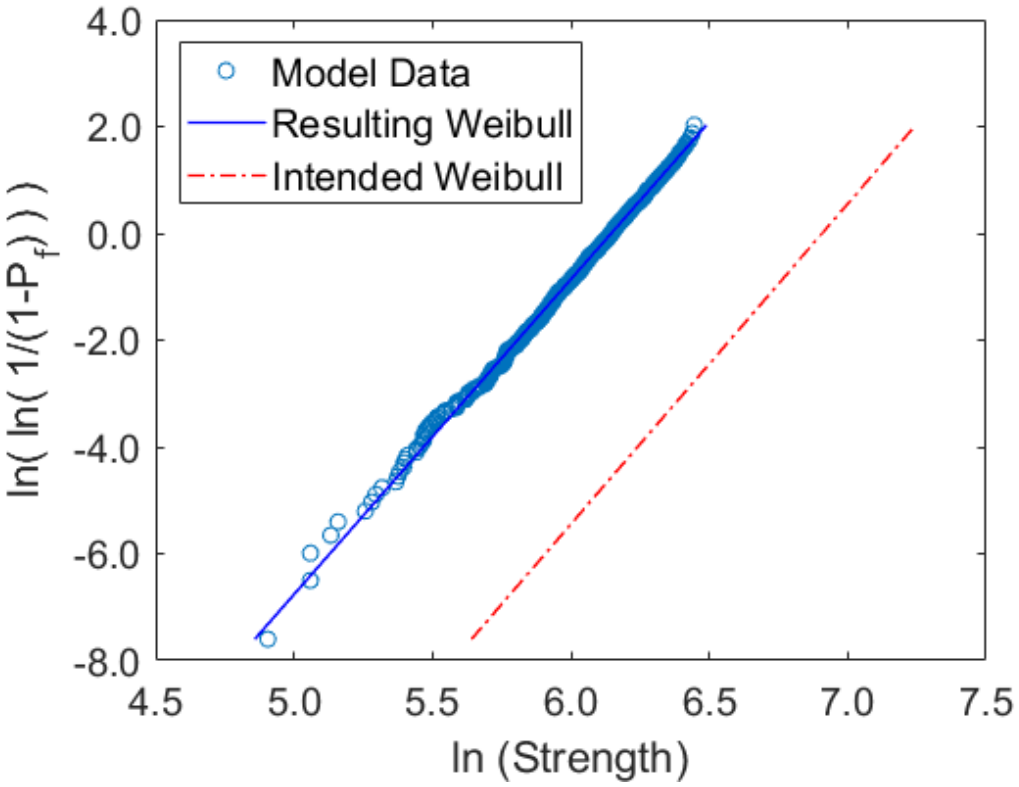

Figure 4-2 The Weibull plot of case 1, a local model of a tensile test with horizon ratio m = 1, making no use of size scaling to adjust the strength of bonds relative to the intended strength of the part to be modelled. Shown are the results of the simulations, the line of best fit, and the target Weibull plot.

Case 2 (see Figure 4-3) fit very accurately to the intended Weibull distribution, with around 1% error in the Weibull modulus, and less than 2% error on the critical stress. The data itself fit very well to the Weibull distribution defined by these parameters, with a R^2 value of 0.996.

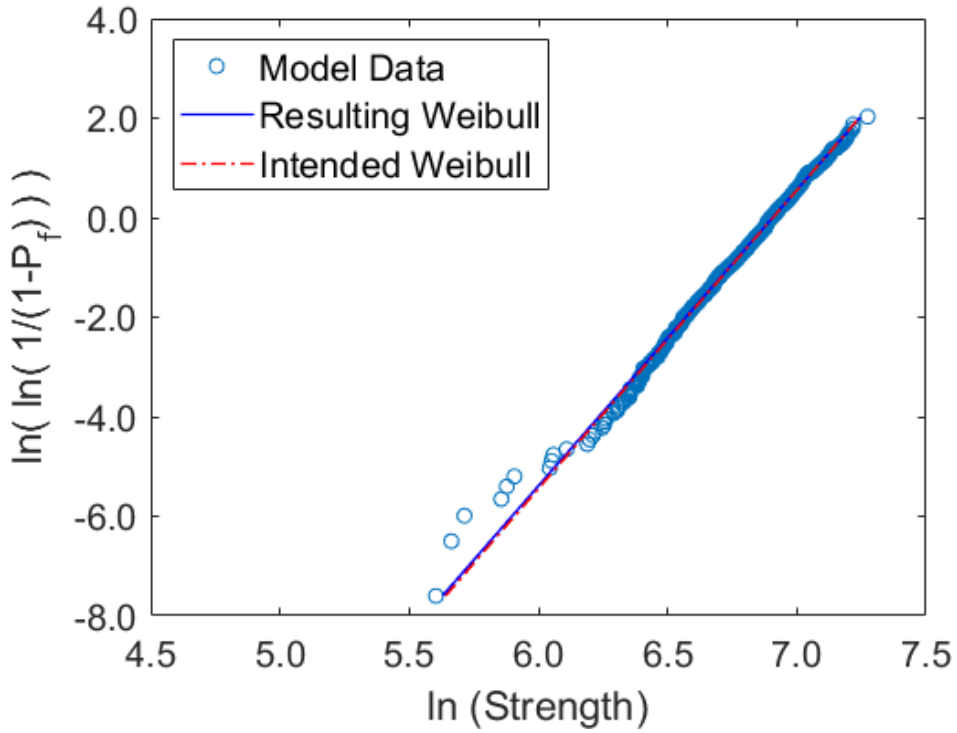

Figure 4-3 The Weibull plot of case 2, a local model of a tensile test with horizon ratio m = 1, with the strength of bonds adjusted relative to the intended strength of the part to be modelled using Weibull size scaling. Shown are the results of the simulations, the line of best fit, and the target Weibull plot.

Increasing the horizon ratio to 3 for case 3 (see Figure 4-4) is the first instance in which a two-stage failure process is seen, similar to the results found by Casolo and Diana [4]. The first bond to fail (termed stage one failure) occurs before overall model fracture, termed stage 2 failure. There was an error in characteristic stress of the overall model ($\sigma_{0,\ Stage\ 2}$ =1331 MPa as opposed to the intended 1000 MPa) and a large error in Weibull modulus ($\beta_{Stage\ 2}$ 10.3 as opposed to 6.0). This is plotted in Figure 4-4 alongside the intended Weibull and a Weibull distribution made up of the stresses at which the first bond failed. The distribution of stage one failures is almost a perfect match to the intended Weibull distribution, with Weibull parameters of $\sigma_{0,\ Stage\ 1}$ = 996 and $\beta_{Stage\ 1}$ = 6.0. Some deviation from the distribution can be seen in the lower tail of the stage 2 fracture, where three stage 2 data points noticeably do not sit on the

trendline. This is in part due to the logarithmic nature of the axes. Differences of the same size appear larger on logarithmic scales when the values are lower. Because of this, deviations in strength from the trendline appear larger at the lower end of the trendline.

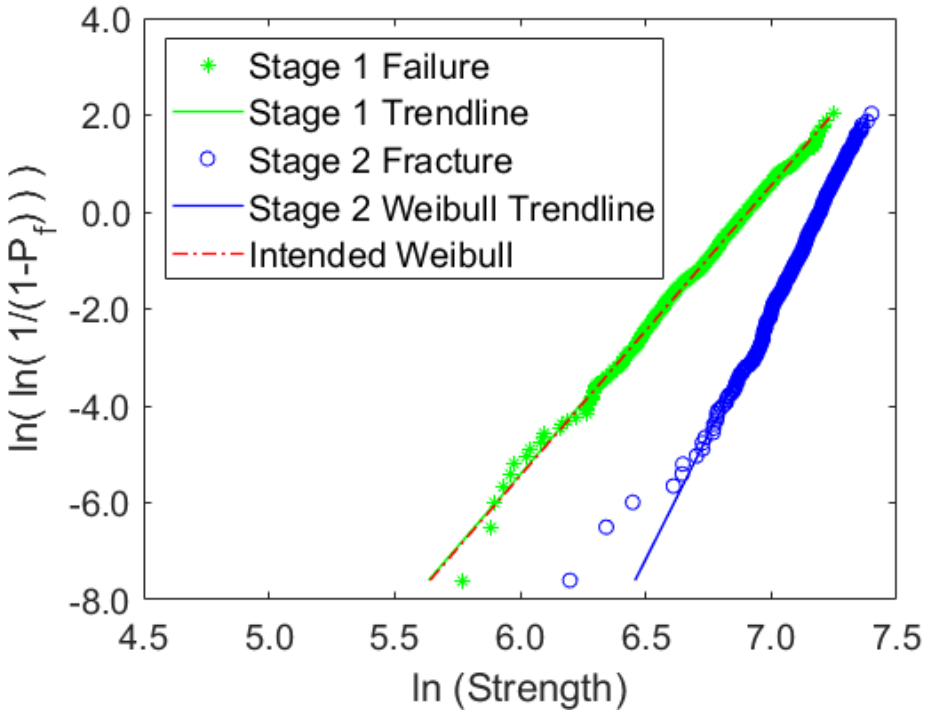

Figure 4-4 The Weibull plot of case 3, a non-local model of a tensile test with horizon ratio m = 3, with the strength of bonds adjusted relative to the intended strength of the part to be modelled using Weibull size scaling. Shown are the stage 1 and 2 failures, the lines of best fit for each, and the target Weibull plot.

When viewing the stress-strain curves of the case three models (see Figure 4-5), a curious phenomenon can be seen. Although the models are intended to be perfectly brittle, and the bonds themselves are, some models can be seen to fracture in stages. The stiffness should be the same (signified by a uniform σ-ε gradient) until complete fracture occurs and the stress immediately goes to zero. In some cases though, the stress can be seen to decrease, before continuing upwards at a lower gradient, before eventually fracturing fully. It was deduced that this unexpected stress-strain profile

was due to some bonds failing while others remained, bridging the gap left by the failed bond. This caused a reduction in global stiffness due to the reduction in the number of bonds. This behaviour is similar to that seen in low temperature ferritic steel fracture toughness tests, and is termed "pop-in" [5]. It is also similar to the two stage fracture seen in peridynamics models using Weibull distributions by Casolo and Diana [4] although in that case the reduction in stiffness is much smaller. The results of the first 3 cases are summarised in Table 4-2.

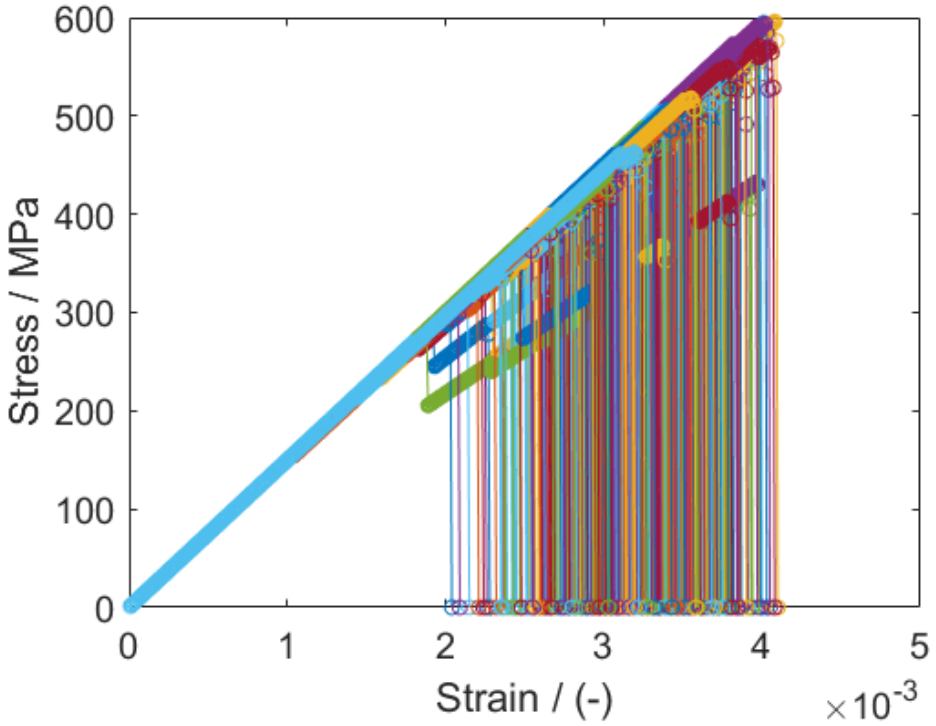

Figure 4-5 The stress strain curves of the parts modelled in case 3, a non-local model of a tensile test with horizon ratio m = 3, with the strength of bonds adjusted relative to the intended strength of the part to be modelled using Weibull size scaling.

Table 4-2 - Parameters describing the Weibull distributions of the bonds and the resulting data for naïve cases 1, - 3.

Variable	Unit	*Case 1*	*Case 2*	*Case 3*
Distribution of bond strength	σ_0 (MPa)	1000	2154	2154
	β	6.00	6.00	6.00
Horizon Ratio, m	-	1	1	3
Scaling	-	None	Bond	Volume
	σ_0 (MPa)	466.8	998.4	1331

Resulting distribution (stage 2)	β	5.90	5.95	10.3

4.4.2 Cases 4-7: Localisation of Failure

Cases 4-7 used the material points as the location of the randomised probability of failure, with the intention that localising this value around each material point would prevent large differences between strengths of bonds occupying similar spaces, and therefore reduce the difference between stage-one and stage-two failure.

Case 4 (see Figure 4-6) produced very similar stage 1 and stage 2 distributions. The models were much stronger than intended ($\sigma_{0,\text{Stage 1}}$ = 1412 MPa and $\sigma_{0,\text{Stage 2}}$ = 1397 MPa) and with a much higher Weibull modulus ($\beta_{Stage\ 1}$ = 10.8 and $\beta_{Stage\ 2}$ = 10.8). In both cases, the data fits well to the Weibull distributions with R^2 values > 0.98 in both cases.

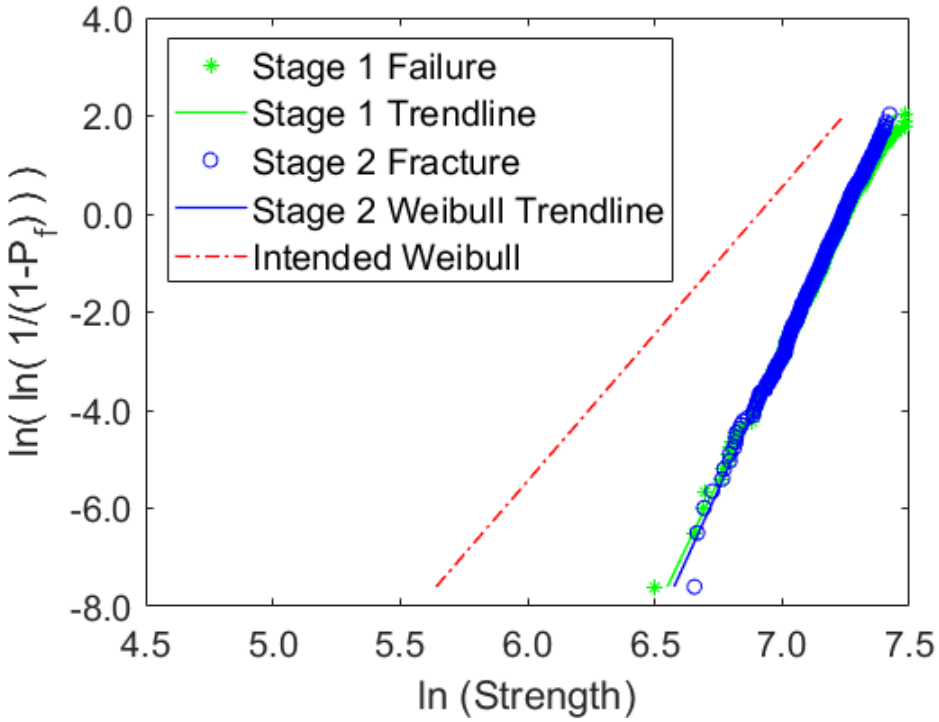

Figure 4-6 The Weibull plot of case 4 a non-local model of a tensile test with horizon ratio m = 3, with the strength of bonds adjusted relative to the intended strength of the part to be modelled using Weibull size scaling. Bond strengths were determined based on averaging random strengths assigned nominally to the material points. Material points sampled for a given bond were those at either end

of the bond. Shown are the stage 1 and 2 failures, the lines of best fit for each, and the target Weibull plot.

Case 5 (see Figure 4-7) used the average of a larger number of random probability of failure values to determine strengths, but similarly produced an overestimate for both characteristic stress ($\sigma_{0,\,Stage\,1}$ = 1424 $\sigma_{0,\,Stage\,2}$ = 1430) and Weibull modulus ($\beta_{Stage\,1}$ = 11.0 $\beta_{Stage\,2}$ = 14.5).The distribution of fracture strengths produced was still a good fit to a Weibull distribution though, with R^2 = 0.9910.

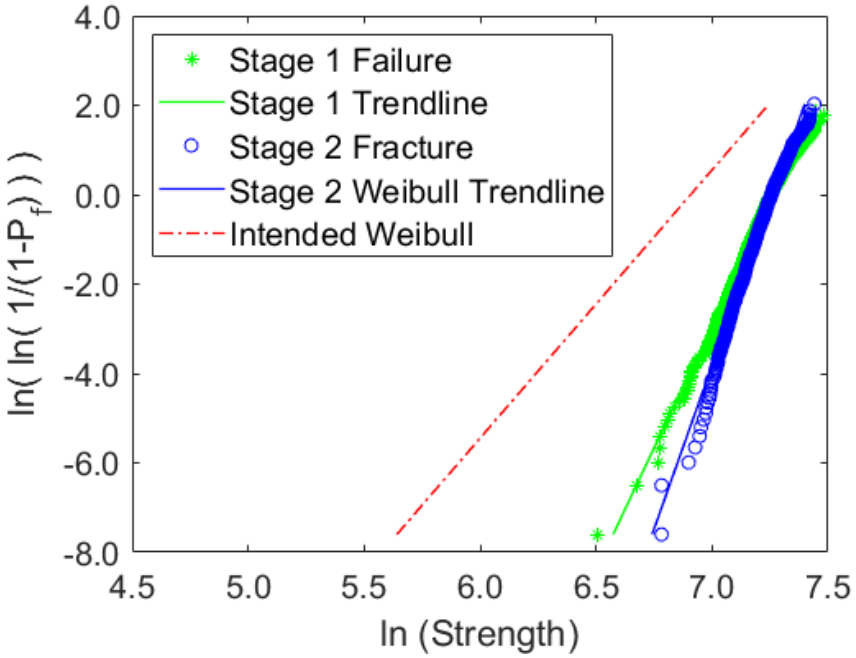

Figure 4-7 The Weibull plot of case 5, a non-local model of a tensile test with horizon ratio m = 3, with the strength of bonds adjusted relative to the intended strength of the part to be modelled using Weibull size scaling. Bond strengths were determined based on averaging random strengths assigned nominally to the material points. Material points sampled for a given bond were all those "overlapped by the bond. Shown stage 1 and 2 failures, the lines of best fit for each, and the target Weibull plot.

Case 6 (see Figure 4-8) assigned the more extreme of the two probability of failure values for the material points a bond connects to the bonds, resulting in a very close match to the intended Weibull distribution in the stage 1 failures ($\sigma_{0,\,Stage\,1}$ = 1014, $\beta_{Stage\,1}$ = 5.94) but the stage 2 failure was inaccurate ($\beta_{Stage\,2}$ = 7.61 and $\sigma_{0,\,Stage\,2}$ = 1226). In both cases R^2 was >0.98. Even in stage 2, this is a step-change in accuracy relative

to the intended Weibull distribution, but still has a significant error. As can be seen in the stress strain curves in Figure 4-9, fracture still occurs in several stages, and in isolated cases the resulting error is very large.

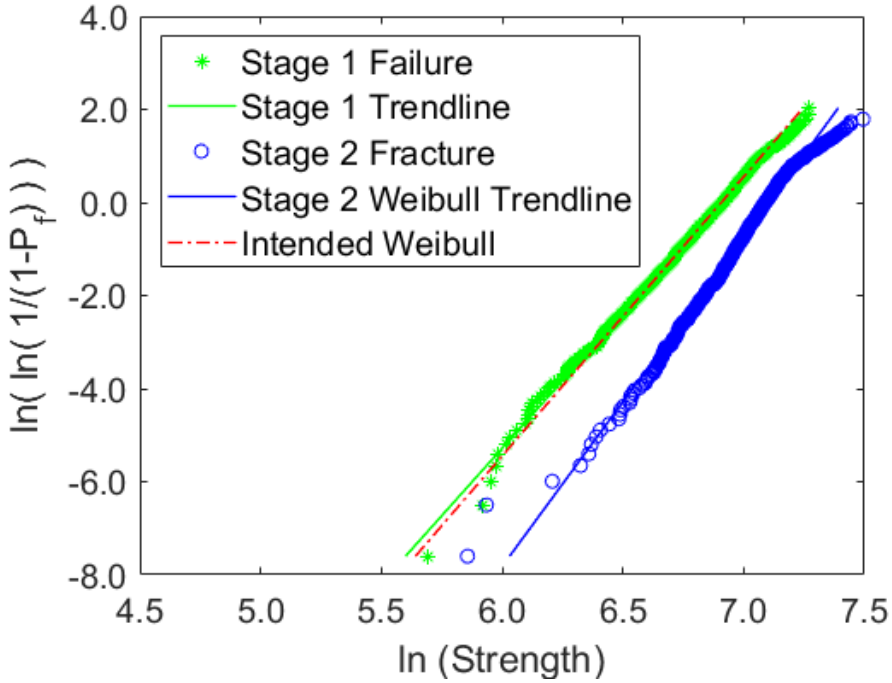

Figure 4-8 The Weibull plot of case 6, a non-local model of a tensile test with horizon ratio m = 3, with the strength of bonds adjusted relative to the intended strength of the part to be modelled using Weibull size scaling. Bond strengths were determined based on the most extreme random strengths assigned nominally to the sampled material points. Material points sampled for a given bond were the two at either end of the bond. Shown are the stage 1 and 2 failures, the lines of best fit for each, and the target Weibull plot.

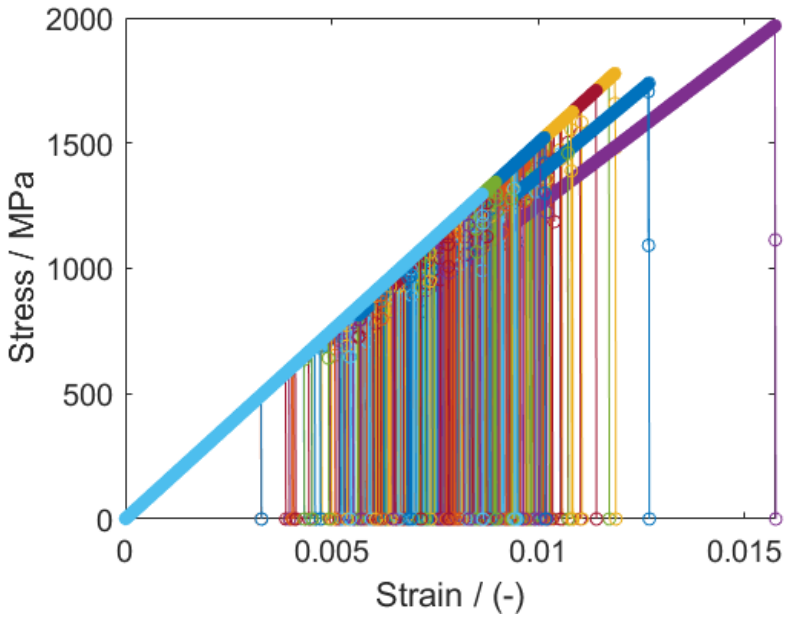

Figure 4-9 The stress strain curves of the parts modelled in case 6, a non-local model of a tensile test with horizon ratio m = 3, with the strength of bonds adjusted relative to the intended strength of the part to be modelled using Weibull size scaling. Bond strengths were determined based on the most extreme random strengths assigned nominally to the sampled material points. Material points sampled for a given bond were the two at either end of the bond.

Case 7 (see Figure 4-10) used parts of cases 5 and 6, namely the consideration of all material points a bond overlaps, and the extreme probability of failure method. This produced an almost exact match with the intended Weibull parameters (β_{Stage1} = 5.87, β_{Stage2} = 5.87 and $\sigma_{0,Stage1}$ = 995.3 MPa, $\sigma_{0,Stage2}$ = 1001 MPa) in both cases R^2 = 0.998.

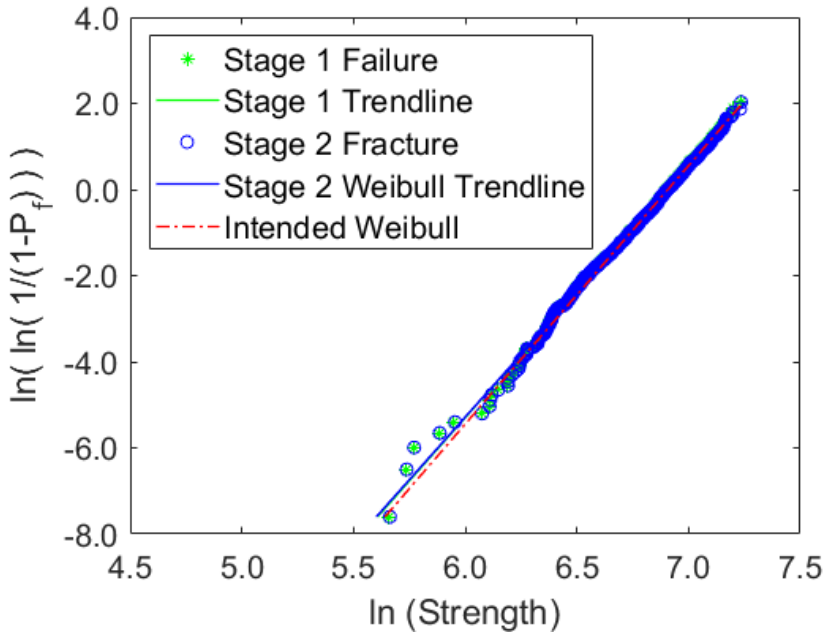

Figure 4-10 The Weibull plot of case 7, a non-local model of a tensile test with horizon ratio m = 3, with the strength of bonds adjusted relative to the intended strength of the part to be modelled using Weibull size scaling. Bond strengths were determined based on the most extreme random strengths assigned nominally to the sampled material points. Material points sampled for a given bond were all those "overlapped" by the bond. Shown are the results of the simulations, the line of best fit, and the target Weibull plot.

The results of both the stage 1 and stage 2 failure distributions from section 4.4.2 are summarised in Table 4-3.

Table 4-3 - Parameters describing the Weibull distributions of sample, the bonds and the resulting data for cases 4-7. The characteristic strength of the sample was 1000 MPa and the modulus 6.00.

Variable	Unit	*Case 4*	*Case 5*	*Case 6*	*Case 7*
Distribution of bond strength	σ_0 (MPa)	2154	2154	2154	2154
	β	6.00	6.00	6.00	6.00
Method	-	Average Connected	Average Overlap	Extreme Connected	Extreme Overlap
Stage 1 Failure Distribution	σ_0 (MPa)	1397	1424	1014	995.3
	β	10.8	11.5	5.94	5.87
Stage 2 Failure Distribution	σ_0 (MPa)	1412	1430	1226	1001
	β	10.8	14.5	7.61	5.87

4.4.3 Mesh Sensitivity

Having established a method that reproduces a Weibull distribution with the correct parameters, mesh sensitivity tests were performed to ensure that the results would be consistent with different material point spacing and horizon ratios. Given that the intention is to scale this model up to higher dimensions and then different geometries, the mesh refinement is expressed in terms of number of total material points. The parameters for the resulting Weibull distributions are summed up in Table 4-4 (Weibull modulus) and Table 4-5 (characteristic stress).

The resulting parameters seem to be insensitive to varying horizon ratio at a consistent material point spacing, as long as the mesh refinement is at a sufficient level, meaning the total number of material points is greater than ~100. Where the number of material points $N = 20$, there is noticeable variation in Weibull parameters with increasing horizon ratio. In the stress-strain curves for large horizon ratios, the partial failure issue is seen to reoccur, but the distortion of the parameters is opposite to that which accompanied this error previously, with both parameters being lower than their intended values. In meshes such as the $m = 5$, $N = 20$ case, half of the model is made up by material points that do not consist of a full horizon, and this leads to the reduction in strength. In any case, such insufficiently refined meshes are clearly not useful for recreating Weibull distributions in one-dimensional peridynamics.

In all cases with $N \geq 100$, the largest error in characteristic strain is <2% and the largest error in characteristic strain is <4%. It can be said with some confidence that this method is mesh insensitive for $N \geq 100$.

Table 4-4 The variation output Weibull modulus with mesh parameters horizon ratio, m and number of material points, N. The input Weibull modulus was β = 6

Number of Material Points, *N*	Horizon ratio, *m* = 1	2	3	4	5
20	5.7	6.00	5.6	5.1	4.9
100	5.77	6.01	6.00	6.13	5.99
200	6.28	5.97	6.02	6.10	5.88
500	6.33	6.02	6.11	5.89	6.01

Table 4-5 The variation in characteristic strength with mesh parameters horizon ratio, m and number of material points, N. The input characteristic strength was 1000 MPa.

Number of Material Points, N	Horizon ratio, *m* = 1	2	3	4	5
20	996.1	1010	966.2	933	870
100	999.7	1001	993.9	981.6	983.8
200	993.8	1006	992.8	987.9	1018
500	995.9	998.4	997.6	987.6	1030

Since Weibull modulus $\beta = 6$ is an arbitrary selection, it was important to also verify that the method is also accurate for other Weibull moduli. Values ranging from $\beta = 1$ to $\beta = 100$ were used, with the same sample size of 1000 as for previous tests. Some small error is visible (up to 5% error in characteristic stress, up to 7% error in Weibull modulus) but the method can reasonably be said to be accurate for this range of β values.

Table 4-6 The variation of output Weibull parameters from a peridynamics model of a tensile test with horizon ratio m = 3, using the "average overlap" method outlined in case 7, with variation in input Weibull parameters. The input characterisitc strength was 1000 MPa

Weibull Modulus (input)	1	10	50	100
Weibull Modulus (output)	0.99	9.64	46.8	101.1
Characteristic Stress (Output)	1044	994.9	949.0	1010
R^2	0.9955	0.9959	0.9651	0.9841

4.5 Discussion

It was established by cases 1 and 2 that scaling of the Weibull distribution to allow for the difference in size between bonds and the overall peridynamics model is a critical step in correctly recreating a Weibull distribution in peridynamics as would be expected based on experimentation [6] and theory [7]. This is not presented as a truly novel result, but was useful to demonstrate given the lack of consideration given to size scaling in the peridynamics literature [2], when distributions of any kind are applied to fracture strengths in modelling. This simple, one-dimensional peridynamics model with the smallest possible horizon can be said to embody the ethos of this chapter. The complexity of the model was reduced such that the only factor controlling the ultimate fracture strength of the model was the strengths determined by the Weibull distribution. The correct method of applying the Weibull distribution then becomes clear. By steadily building up the layers of complexity, the correct method of applying Weibull distributions in more complex models can also be determined.

In cases 3 and 4, it was shown that using size scaling for the Weibull distribution is insufficient when considering a non-local approach, such as peridynamics with a horizon ratio $m > 1$. In higher dimension models, using a horizon size $m < 3$ can cause problems in the calculation of shear forces, since the directions that force can be applied are limited. For this reason, such small sizes are rarely used in the peridynamics literature, and even then for demonstration purposes only [3], although a horizon ratio $m = 2$ is used in 1-Dimension in [8]. Regardless, for the method to be of use in two-dimensional models, it must be established to work at horizon ratios with significant non-locality, and cases 3 and 4 show poor accuracy in recreating the

Weibull distribution. These cases, and case 3 in particular, act to outline the problem as it existed before the work in this chapter was carried out. Fracture distributions, when applied naively to peridynamics are distorted by the sampling of the distribution for each bond. By the nature of size scaling these errors are reduced by increasing of the Weibull modulus, but would still be noticeable in [2] (fracture distribution approximately as broad as a Weibull distribution with $\beta = 10$) and [9] where a Weibull modulus $\beta = 50$ is used. Even when the appropriate scaling method is used, partial fractures of the model distort the Weibull parameters of the overall model, and promote unphysical stress-strain curves. The result in Case 4 is similar to that in Casolo and Diana [4]. In the stage 2 failure there is good agreement at the top tail of the distribution, but the slope of the distribution is too steep, and therefore there is poor accuracy to the intended distribution at the bottom tail. The stage 1 failure is much more accurate in this work than in the model by Casolo and Diana. This may be due to scaling using the number of gaps between material points in this work compared to the size scaling used by Casolo and Diana, based on the relative volume of bonds to the overall part to be modelled. It is worth noting too, that recreating Weibull distributions in peridynamics is much more complex in two dimensions than in one dimension, as will be explored in Chapter 5.

Cases 5-8 display the iterative process towards a method of accurately recreating a Weibull distribution in peridynamics. The starting point was that strength of bonds should be related to their location in some way, such that bonds with very different strengths do not occupy the same inter-material point spaces. Since bonds do not simply exist at a single point along the one-dimensional model, it was necessary to

determine the appropriate way for the location of the bonds to be interpreted for this purpose. Using a simple average of the probability of failure values at each end of the bond, as in case 5, perhaps unsurprisingly produced poor results because of the loss of fidelity to the intended distribution at the lower tail, which is critical in determining fracture strength. Not only did extending this method slightly to take account of the material points in between not significantly improve the results, it in fact made them less accurate, increasing the error in Weibull modulus from 95% to 142%. The reason for the inefficacy of the averaging methods is that fracture distributions are inherently dependent on the lowest values of fracture stress, since these are the points at which fracture occurs. Averaging the fracture stresses increases the lowest values, increasing the average fracture strength of the models, and decreasing the variability between the strongest and weakest models.

The methods for cases 7 and 8 were therefore conceived as the opposite of averaging. Where averaging drags all values towards the middle, the “extreme” method discards the values that are close to the average fracture stress.

4.6 Conclusions

A method for recreating Weibull distributions in one-dimensional peridynamics was outlined. The key aspects of this method to be carried forward into a future two-dimensional model are:

- Fracture distributions applied to peridynamics bonds must be scaled appropriately to accommodate the difference in size between bonds and the overall part to be modelled. The distribution applied to the bonds must be

significantly stronger on average than the distribution that is intended to be recreated in the model, but have the same variability in relative terms. This transformation is relatively simple for the Weibull distribution.

- Fracture criteria of peridynamic bonds must be heterogeneous. If the bond strengths are randomised completely, the effect is to "smear" the randomisation, effectively removing it. By tying bond strengths to location, bonds occupying similar spaces take on similar strengths, and the nucleation of fracture is made concurrent with propagation.
- The lower tail of the fracture distribution must be maintained through any operations performed on the distribution. Any method which alters the fracture criterion of the lowest strength bond will alter the overall distribution. This was achieved in this work by using an "extreme" method which deliberately samples the distributions at the two tails.

4.7 References

[1] L. D. Jones, T. A. Haynes, L. J. Vandeperre, and M. R. Wenman, "Theory and application of Weibull distributions to 1D peridynamics for brittle solids," *Comput. Methods Appl. Mech. Eng.*, vol. 363, p. 112903, May 2020, doi: 10.1016/j.cma.2020.112903.

[2] S. Oterkus and E. Madenci, "Peridynamic modeling of fuel pellet cracking," *Eng. Fract. Mech.*, vol. 176, pp. 23–37, May 2017, doi: 10.1016/j.engfracmech.2017.02.014.

[3] F. Bobaru and W. Hu, "The Meaning, Selection, and Use of the Peridynamic Horizon and its Relation to Crack Branching in Brittle Materials," *Int. J. Fract.*, vol. 176, no. 2, pp. 215–222, Aug. 2012, doi: 10.1007/s10704-012-9725-z.

[4] S. Casolo and V. Diana, "Modelling laminated glass beam failure via stochastic rigid body-spring model and bond-based peridynamics," *Eng. Fract. Mech.*, vol. 190, pp. 331–346, Mar. 2018, doi: 10.1016/j.engfracmech.2017.12.028.

[5] R. W. Boyle, A. M. Sullivan, and J. M. Krafft, "Determination of plane strain fracture toughness with sharply notched sheets," *Weld. J.*, vol. 41, p. 428, Sep. 1962.

[6] A. Bhushan *et al.*, "Weibull Effective Volumes, Surfaces, and Strength Scaling for Cylindrical Flexure Specimens Having Bi-Modularity," *J. Test. Eval.*, vol. 44, Sep. 2016, doi: 10.1520/JTE20150301.
[7] W. Weibull, "A Statistical Distribution Function of Wide Applicability," *ASME J. Appl. Mech.*, Sep. 1951.
[8] F. Bobaru, M. Yang, L. F. Alves, S. A. Silling, E. Askari, and J. Xu, "Convergence, adaptive refinement, and scaling in 1D peridynamics," *Int. J. Numer. Methods Eng.*, vol. 77, no. 6, pp. 852–877, Feb. 2009, doi: 10.1002/nme.2439.
[9] W. Li and K. Shirvan, "Multiphysics phase-field modeling of quasi-static cracking in urania ceramic nuclear fuel," *Ceram. Int.*, vol. 47, no. 1, pp. 793–810, Jan. 2021, doi: 10.1016/j.ceramint.2020.08.191.

Chapter 5 Modelling Weibull Distributions in Two-Dimensional Peridynamics

5.1 Introduction

In Chapter 4 it was established that while peridynamics may not immediately lend itself to implicit modelling of fracture distributions (i.e. where the fracture distribution is produced by variations in bond properties, representing flaws on a scale much smaller than the mesh), it is still possible in one dimension. There may be situational uses for such a model but given the lack of information provided beyond that which is input to the model, such uses are limited. In order for a peridynamics model with an implicit fracture distribution (i.e by modifying the material properties of the bonds, not by explicitly including the small flaws that lead to a distribution of strengths) to be useful in engineering applications it must at the very least be scaled up to two dimensions.

Increasing the number of dimensions brings significant challenges. Appropriately size scaling the Weibull distribution was one of the key steps in producing an accurate one-dimensional model, but the size scaling was made simpler by all of the bonds being

equally involved in fracture. No bond was more likely to nucleate a crack than another, and there was almost no crack "growth" to speak of. In 2-dimensions cracks can nucleate either on the edges of the mesh, representing the surface of a 3-dimensional body, or in the bulk. This means size scaling can be dependent on either the total area of the model, or just the length of the loaded edges, or anywhere in between.

In order to test the model in 2-dimensions, a change in implementation was first necessary. Although MATLAB proved useful in rapidly testing the simple one-dimensional model, building from scratch meant no access to implicit time integration and other useful tools built into Abaqus. Implicit time integration is essentially a necessity for modelling fracture on an engineering scale which can occur on long-timescales, especially where nucleation must occur first. The intention is to model the fracture of nuclear fuel on a power ramp on the order of hours [1], and the model must be able to resolve brittle crack growth bursts occurring on the order of μs [2]. If the model could not increase and reduce the timestep appropriately, either instability or impractical computational expense would be inevitable.

This chapter outlines a method for recreating a Weibull distribution in a two-dimensional bond-based peridynamics model, and tests its resilience to varying mesh and Weibull parameters.

5.2 Methodology

5.2.1 Weibull in Peridynamics Implementation

This implementation of Weibull in peridynamics takes as its starting point the one-dimensional implementation from chapter 4. Every material point is randomly

assigned a probability of failure, which can be considered as a fracture strain by rearranging the Weibull cumulative probability distribution

$$P_f = 1 - exp\left(-\left[\frac{\varepsilon}{\varepsilon_0}\right]^{\beta}\right) \tag{5.1}$$

Where P_f is the probability of failure at a given strain ε for an object with Weibull modulus β and characteristic strain ε_0

Knowing that the additive inverse of the probability of failure P_f is the probability of survival P_s

$$P_s = 1 - P_f \tag{5.2}$$

We can substitute (5.2) into (5.1) and rearrange

$$P_s = exp\left(-\left[\frac{\varepsilon}{\varepsilon_0}\right]^{\beta}\right) \tag{5.3}$$

And by taking the natural logarithm of both sides

$$-\ln\left(P_s\right) = \left[\frac{\varepsilon}{\varepsilon_0}\right]^{\beta} \tag{5.4}$$

Before raising each side to the power of $1/\beta$

$$-\ln\left(P_s\right)^{\frac{1}{\beta}} = \left[\frac{\varepsilon}{\varepsilon_0}\right] \tag{5.5}$$

And finally multiplying both sides by the characteristic strain ε_0 gives the failure strain ε assigned to that material point.

$$\varepsilon = \varepsilon_0(-\ln(P_s)^{\frac{1}{\beta}}) \tag{5.6}$$

Since material points do not themselves undergo strain, this property must be transferred to the bonds. In 1-dimension this was done by considering the P_f values of all material points that were overlapped by a bond, and taking the most extreme value. The "extremeness" φ of a value is defined by

$$\varphi = |0.5 - P_f| \tag{5.7}$$

In order to recreate this method in 2-dimensions, the idea of "overlapping" must be reconsidered. In 1-dimension, overlapping is defined as such:

The relevant material points to a bond connecting material point i to material point j are any which satisfy

$$x_i \leq x_{mp} \leq x_j \tag{5.8}$$

where x_i is the location of the first material point connected to a bond, x_j is the location of the second material point a bond is connected to, and x_{mp} is the location of any other material point.

To generalise this statement so it can be applied to two dimensions, for a material point to be considered for a given bond, it must be no further than a bond's length away from either material point making up the ends of the bond. For a given material point *k* to be considered relevant to a bond connecting material points *i* and *j*, it must satisfy both conditions

$$distance_{i-k} \leq distance_{i-j} \tag{5.9}$$

$$distance_{j-k} \leq distance_{i-j} \tag{5.10}$$

The area of consideration is therefore extended in the direction perpendicular to the bond. This can perhaps most easily be understood in schematic form (see Figure 5-1). This produces the effect that the bonds surrounding and perpendicular to a "low-strength" material point take on its low failure criterion, and cracks can propagate more easily from that spot.

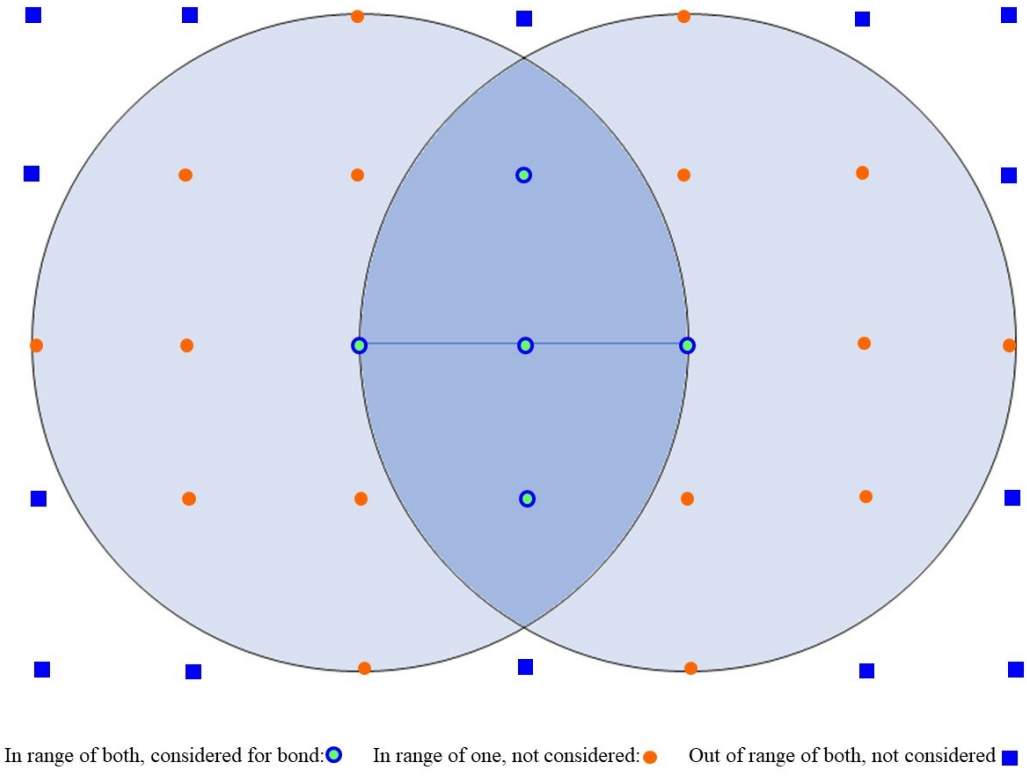

Figure 5-1 A schematic of the region of material points scanned to determine the failure strain of a bond with length equal to twice the material point separation. The circles have radii equal to the length of the bond, represented by a blue line.

Just as the heterogenization method had to be reconsidered when scaling up to 2-dimensions, the same is true for size-scaling. Mathematically, the size-scaling is the same, since the model is still discretised into a number of material points *N*, just as in the one-dimensional case, so the correction to the characteristic strain is the same.

$$\varepsilon_{0,Bond} = N^{1/\beta}\varepsilon_{0,Sample} \tag{5.11}$$

The difference in 2-dimensions is the interpretation of *N*. In a one-dimensional tensile test, *N* is simply the number of material points in the model. There is no other way to define the size of a one-dimensional peridynamics object in terms of its material points. Real objects are much more complex, and determining the effective size of a test specimen is an important step in Weibull analysis [3]–[5]. Weibull characteristics can scale with either the volume of the specimen, or the surface area. Determining the best way to define the effective size of the peridynamics model, and what value to use for *N* is an important part of formulating a method for recreating Weibull distributions in two-dimensional peridynamics, and is addressed in section 5.3.1.

5.2.2 Simulation Setup

Typically, brittle materials of the type that would benefit from Weibull analysis are tested in flexion, [3]–[5] often either three or four-point bend tests. This introduces difficulties in peridynamics whereby bonds in the areas close to where the load is applied can undergo fracture induced by the load, rather than by the bending moment. This fracture can be avoided by artificially increasing the resistance to failure of the

bonds in such areas, but this may interfere with legitimate cracks that may grow into these areas.

In order to avoid the complications of flexural tests, the model was tested in a tensile test arrangement. The reason this method is not used in physical experiments is that applying such a load is difficult for brittle materials, but there are no such issues in a peridynamics model. An increasing displacement boundary condition was applied to one end of the model, while the other end was restricted to zero displacement in the direction of the extension. The material points making up the mid-line of the model in the direction parallel to the extension were restricted to zero displacement perpendicular to the extension in order to constrain the model. Although a correction is applied to make up for the reduced stiffness in surface areas, it is not perfect, so to prevent an influence of this on the failure strain of the model, bonds originating within one horizon of either end of the model are prevented from failing. A schematic of the setup is show in Figure 5-2.

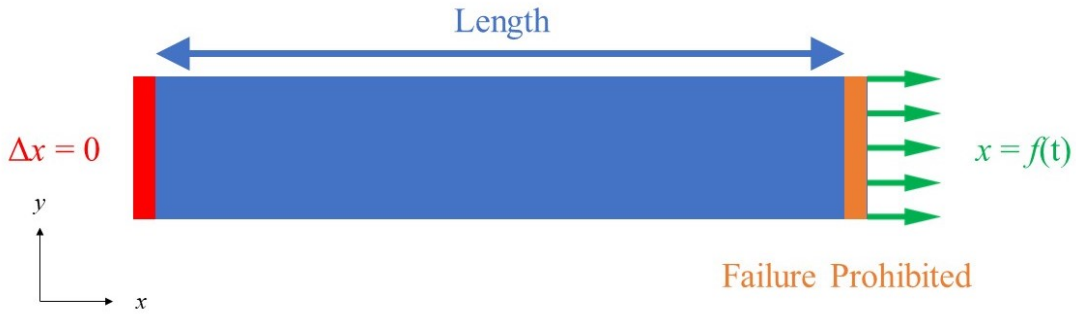

Figure 5-2 Setup of simulations to evaluate Weibull behaviour in 2D peridynamics. A strain-controlled tensile test was used. Reproduced from [6].

In more complex loading regimes, this would require determining how much load is applied to each area or edge length, and determining the effective area or edge length

of the model. The tensile test setup was chosen so as to simplify these calculations though, and the effective edge length was simply the gauge length, the length of the two edges parallel to the displacement, accounting for the fact that bonds at either end were prevented from failing divided by the material point spacing.

The effective area of the model was simply the number of material points in the model, accounting for the fact that some bonds were prevented from failing, and therefore did not contribute to the effective area.

The mesh used was square, with inter-material point spacing varying between 0.04 and 0.125mm, as described in Section 5.3.2.1. With a square mesh, there is a tendency for cracks to grow in the two primary directions of the mesh. In this case, this meant that cracks growing directly across the specimen were more likely than cracks growing diagonally. While crack growth direction is to some degree affected by microstructure and defects, this was not represented in this work. The dominant factor in determining crack growth direction in this model is the load direction.

5.3 Results

5.3.1 Scaling Method

Firstly it was necessary to determine the most appropriate size-scaling method for the Weibull distributions in this model. A sample of 30 simulations each were run with the area-scaled method (representing volume in 3D) and the length-scaled (representing surface area in 3D) method. Weibull parameters were then determined based on these samples and these were compared to the Weibull parameters of ε_0 = 8.34 x 10^{-4} and β = 6.00. The length-scaled method produced a distribution with parameters of ε_0 = 9.38 x 10^{-4} and β = 12.5. The area-scaled method produced a

distribution with parameters of ε_0 = 1.70 x 10^{-3} and β = 8.65. Although the area-scaled method more closely recreates the intended shape of the distribution, it is plain to see when the results are plotted, as in Figure 5-3, that the length-scaled method produces a closer fit to the intended distribution. Further evidence of this is that of all of the area-scaled models, only two fractures were caused by cracks initiating in the bulk. Since fracture overwhelmingly initiates at the surface regardless of scaling method, it is clear that in this setup, the dominant size feature is the length of the object being modelled. No conclusion can be drawn from this data as to whether this is a feature of modelling technique or the loading regime.

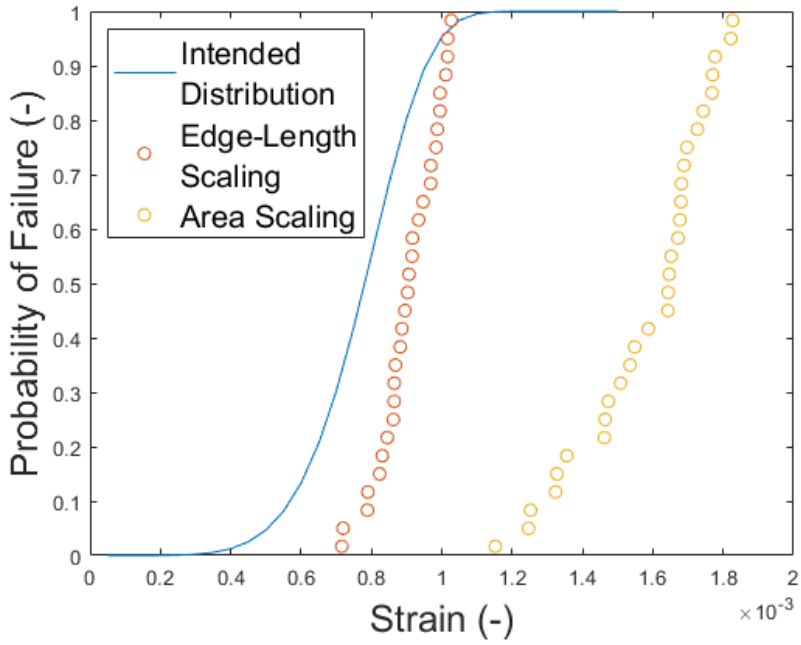

Figure 5-3 The results of using entirely surface-scaled or entirely volume-scaled bond strength. The intended Weibull parameters are $\varepsilon_0 = 8.3 \times 10^{-4}$ and $\beta = 6$. The surface scaled method gave values of $\varepsilon_0 = 9.38 \times 10^{-4}$ and $\beta = 12.46$. The volume scaled method gave $\beta = 8.65$ and $\varepsilon_0 = 17 \times 10^{-4}$. Reproduced from [6].

A notable characteristic of both methods was the failure of significant numbers of bonds not immediately leading to fracture of the entire model, which only occurs after

a significant amount of additional strain is accrued. An example of this is shown in Figure 5-4. This behaviour contrasts with the idea inherent to Weibull that fracture occurs at a single value for strain.

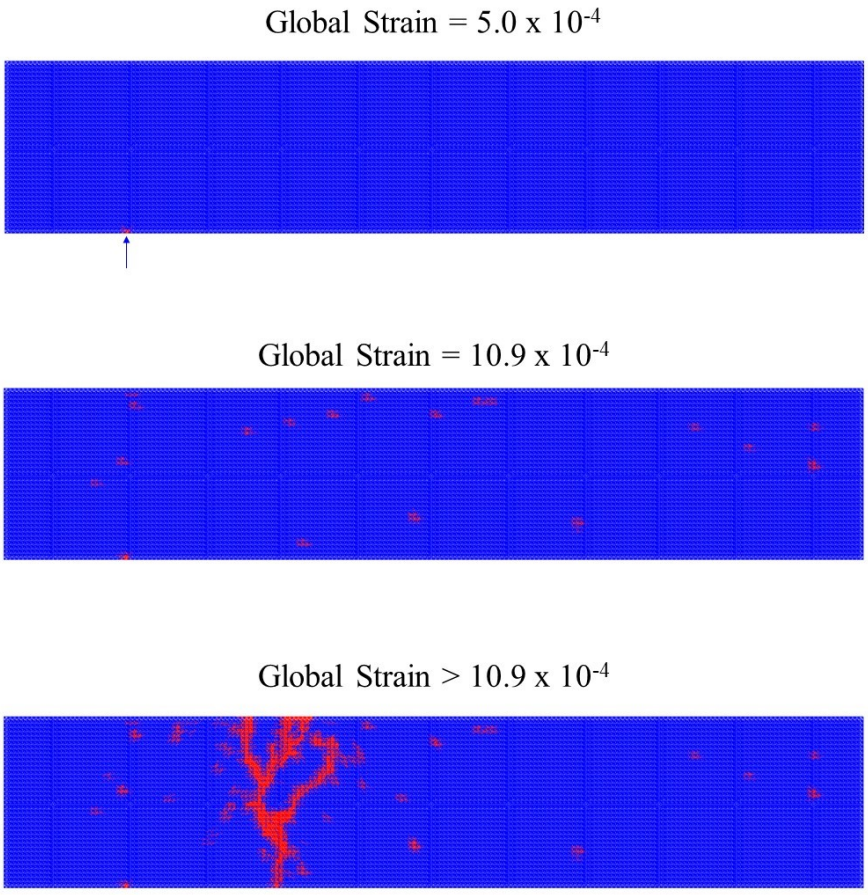

Figure 5-4 Using the all surface-scaled method, cracks can initiate, but then be stopped before they reach critical size. This can lead to much higher strain at failure than would otherwise be dictated by the Weibull distribution. Reproduced from [6].

Fracture in the peridynamics models occurs in two stages, similar to the models of Casolo and Diana [7]. First, there is failure of a small number of bonds, termed stage 1 failure, followed by eventual failure of the entire tensile test specimen, termed stage

2 failure. Examining the values for strain at which the first bond failure occurs, and fitting a Weibull distribution gives the parameters of $\varepsilon_{0,\ Stage\ 1} = 8.70\ x10^{-4}$ and $\beta_{Stage\ 1} = 7.94$. When plotting the two datasets next to the intended distribution, (see Figure 5-5) a much better fit to the intended distribution can be seen in the strain values for initial bond failure. It is notable that the initiation failure strains are not below the intended distribution, as they were when similar simulations were performed by Casolo and Diana [7]. The gap between initial failure and eventual fracture of the model is larger for models with low fracture strain, and this is what distorts the Weibull shape parameter. The error stemmed in part from the fact that the fracture strain of bonds was randomised all across the model, meaning some bonds in the bulk were very strong, and prevented growth of cracks that had nucleated in weaker bonds on the surface.

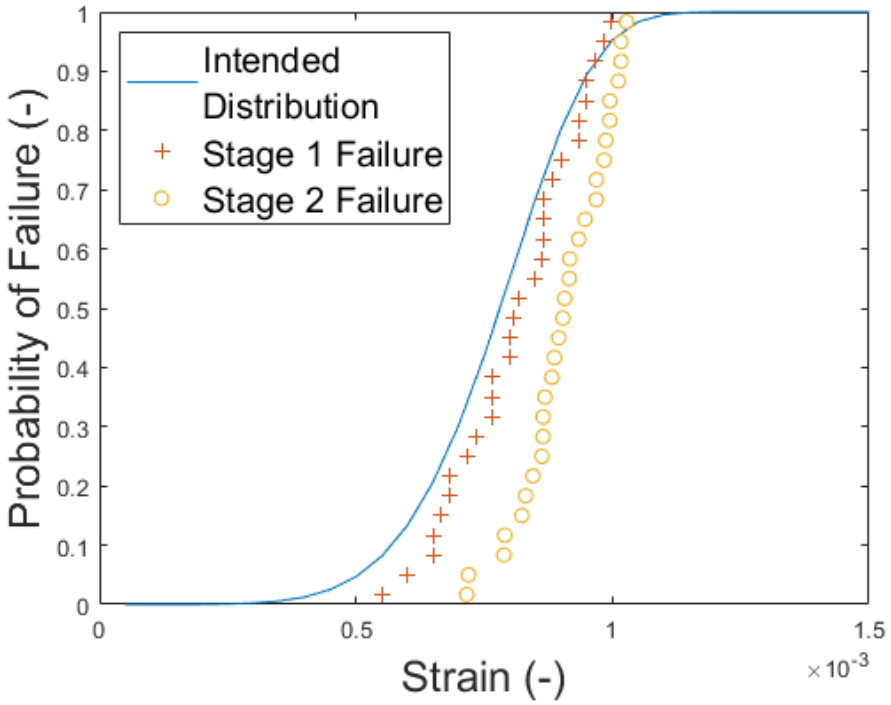

Figure 5-5 The stage 1 (failure of a single bond) and stage 2 (fracture of the overall part modelled) failure strains plotted relative to the intended distribtuion of $\varepsilon_0 = 8.3 \times 10^{-4}$ and $\beta = 10$ randomising

all bond critical strain values accoring to a Weibull distribution scaled according to the edge length of the modelled part. Reproduced from [6].

If it is assumed that cracks always nucleate on the surface (a reasonable assumption in many applications, and true of the length-scale method) the bulk of the model should not have a randomised fracture strength at all. Cracks would only be growing in the bulk, not nucleating, and the Weibull distribution applied to the bonds is intended to control the nucleation behaviour of cracks, not growth. When only the edges of mesh were randomised according to a Weibull distribution the overall resulting characteristic strengths were similar, (9.30×10^{-4} with edge-only, 9.41×10^{-4} when all the bonds were randomised) but the edge-only method gave a much better fit to the intended Weibull modulus (8.24 with edge-only, 12.4 when all the bonds were randomised).

The difference that arises from using the edge-only method is visible in a quantitative comparison of the crack arrest phenomenon shown in Figure 5-4. The degree to which arrest occurs is plotted against the strain at crack initiation in Figure 5-6, for the edge-only method and the all Weibull method. Significant extra strain is accrued before fracture in many cases with the all Weibull method, where only an isolated few see more than 10^{-4} extra strain when randomising only the bonds connected to edge material points. When increasing the Weibull modulus to 7.5 using the same method, there are zero such cases.

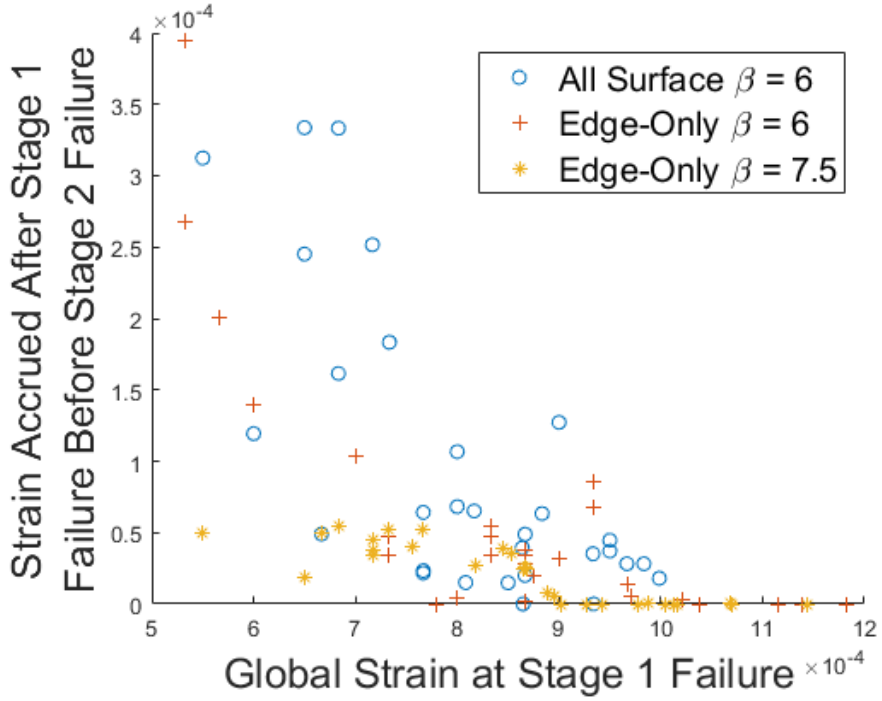

Figure 5-6 Crack arrest profiles of the all surface-scaled method, and the edge-only method with β = 6.0 and β = 7.5. Reproduced from [6].

When increasing the Weibull modulus beyond 7.5, the error in the output Weibull modulus can be seen in Table 5-1 to stabilise at 12-13%. As the Weibull modulus gets smaller, the spread of fracture strains grows. As such, any error associated with these strengths would be expected to grow. It appears that using low Weibull moduli (in this case, $\beta = 6$) causes an increase in the error in both Weibull modulus and characteristic strain such that the model can no longer be said to be sensitive to changing input Weibull modulus. This drastic increase in error relative to the higher Weibull modulus ($\beta \geq 7.5$) can largely be attributed to a greater propensity for cracks to not immediately propagate after initiation in the $\beta = 6$ case. Evidence of this can be seen in the fact that the stage 1 distributions remain quite responsive to changes in input Weibull modulus, and in Figure 5-7, where some significant crack arrest can be seen in the $\beta = 6$ case, decreasing to almost zero in the $\beta = 12$ case.

Table 5-1 The effect upon output Weibull parameters of varying input Weibull modulus

Input β	β stage 1 (error)	$\varepsilon_{0,\text{ Stage 1}}$ (10^{-4}) (error)	β stage 2 (error)	$\varepsilon_{0,\text{ Stage 2}}$ (10^{-4}) (error)
6.0	5.27 (-13%)	9.10 (+9%)	8.24 (+37%)	9.30 (+12%)
7.5	6.41 (-15%)	9.12 (+9%)	8.38 (+12%)	9.14 (+10%)
9.0	7.65 (-15%)	8.98 (+8%)	10.06 (+12%)	9.00 (+8%)
12.0	14.79 (+23%)	8.97 (+8%)	13.59 (+13%)	8.97 (+8%)
1.0 x10^5	N/A	8.34 (+0%)	N/A	8.34 (0%)

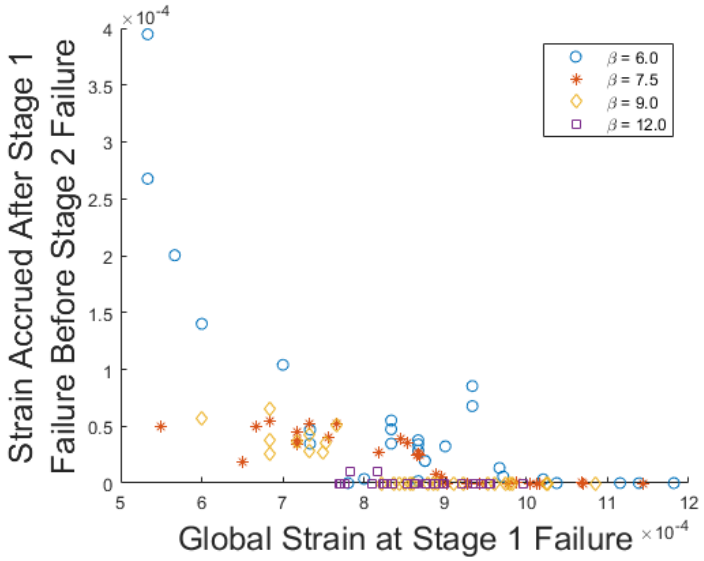

Figure 5-7 Crack arrest profiles using the edge-only Weibull method with β = 6.0, β = 7.5, β = 9.0 and β = 12.0. Reproduced from [6].

5.3.2 Mesh Parameter Testing

To test the model's capacity to adjust to changing mesh conditions and still produce an approximately correct distribution, it was necessary to perform the test with a

variety of different inter-material point spacings and horizon ratios. These tests were performed using an intended Weibull modulus of $\beta = 6$.

5.3.2.1 Inter-Material Point Spacing

The inter-material point spacing was varied between 0.04 mm (254 material points per long edge) and 0.125 mm (74 material points per long edge) and although some variation is visible in the output Weibull parameters (see Figure 5-8), upon plotting graphically, the data appears to be very similar. If taken as one dataset, it can be described by a Weibull distribution with Weibull modulus $\beta = 8.59$, and characteristic strength $\sigma_0 = 9.82 \times 10^{-4}$ and this may be the best way to conceptualise this result. Some small variation would be expected between different samples of this size, and none of the parameters of the individual datasets vary by more than 12% away from the modulus of the combined dataset or 6% from the characteristic strength of the combined dataset.

Nodal Spacing (mm)	Output β	Output ε_0 (10^{-4})
0.1250	8.08	9.76
0.1000	8.60	9.50
0.0800	7.87	9.59
0.0625	7.63	9.79
0.0500	8.24	9.30
0.0400	9.18	9.60

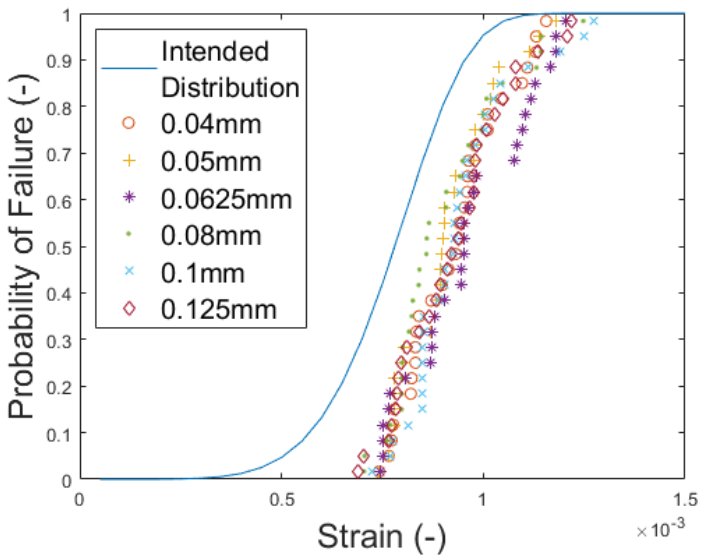

Figure 5-8 The results varying material point spacing from 0.125mm to 0.04 mm. The intended Weibull parameters are $\varepsilon_0 = 8.3 \times 10^{-4}$ and $\beta = 6$. Reproduced from [6].

No trend can be seen in the crack arrest plot for the different inter-material point spacings (Figure 5-9). All follow roughly the same pattern of increasing error with decreasing initial fracture strain. It is notable that of the few noticeable errors at high initial fracture strain, most come from the two coarsest meshes tested, and so it is recommended to use at least 119 edge material points in future work, equivalent to the 0.08 mm mesh spacing here.

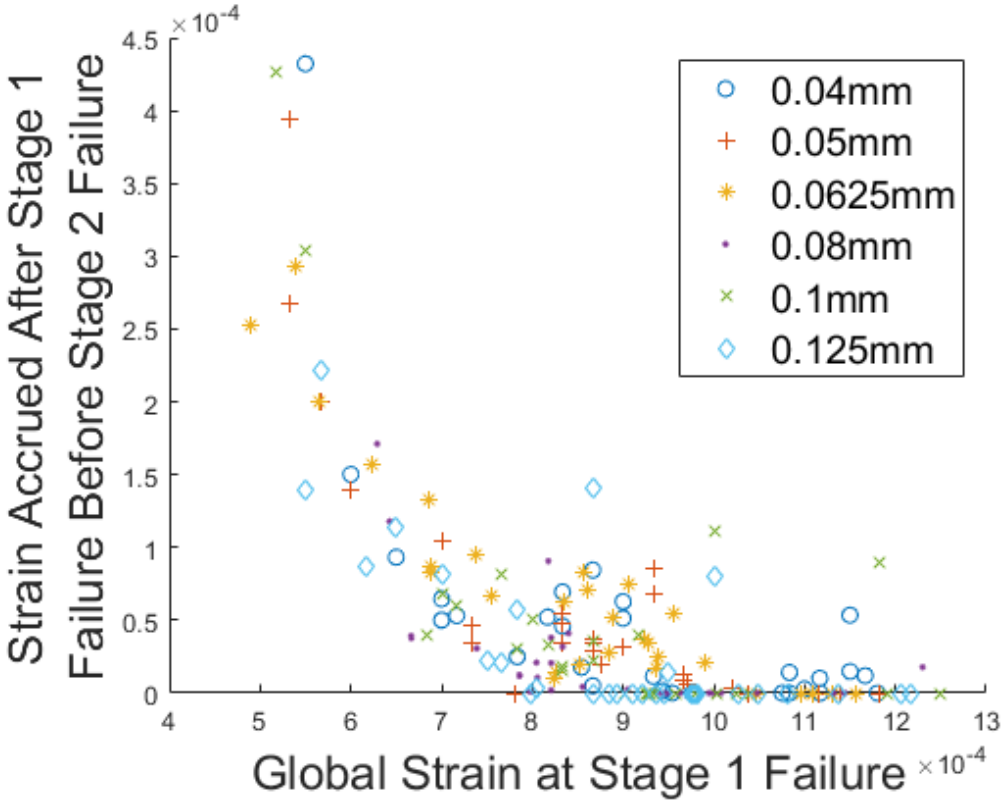

Figure 5-9 The crack arrest profiles of five different mesh refinements. Reproduced from [6].

5.3.2.2 Horizon Ratio

Based upon the work in methodology Section 3.2.5, the horizon ratio, m, was varied between 3-5 using only integers, as these are the values which most accurately recreate the intended elastic behaviour. This was done using a consistent inter-material point spacing of 0.08 mm, so that the m = 5 case still used a sufficiently small number of bonds so as not to trigger memory allocation issues in Abaqus.

Where the different inter-material point spacing samples were characterised by random variation between different samples, the same cannot be said when varying horizon ratio. A clear pattern is visible in that increasing horizon ratio drastically increases the output Weibull modulus. The exact source of this error is unknown, but it is possible that this is another example of the same fundamental problem that occurred in the development of the one-dimensional method. As more non-locality is added, the chances of bonds interfering with an initiated crack and preventing it from propagating are increased.

Horizon Ratio	Output β	Output ε_0 (10^{-4})
3	7.87	9.59
4	9.29	9.85
5	15.44	9.91

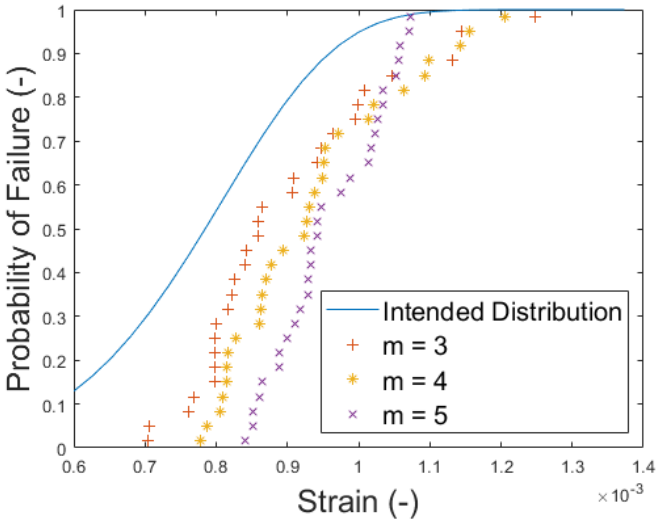

Figure 5-10 The results of varying horizon ratio, m. The intended Weibull parameters are $\varepsilon_0 = 8.3 \times 10^{-4}$ and $\beta = 6$. Reproduced from [6].

There is some evidence for the theory that non-locality is preventing cracks from propagating in the crack arrest plot in Figure 5-11. There are two cases of very significant crack arrest in the $m = 4$ case, and widespread examples of arrest in the $m = 5$ case.

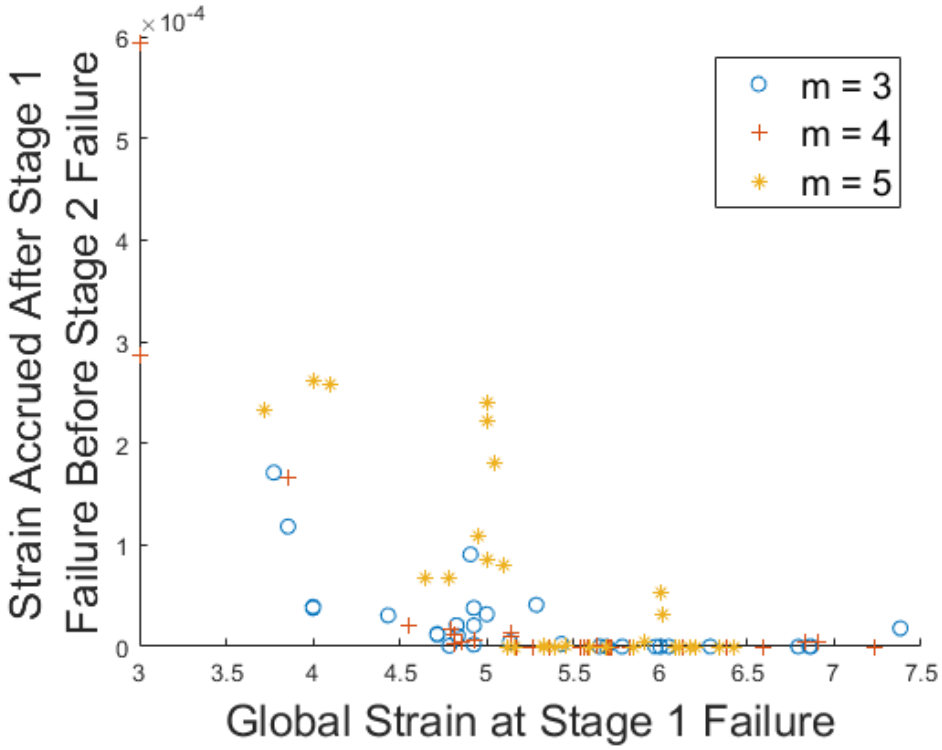

Figure 5-11 5-12 The crack arrest profiles of three different horizon ratios. The intended Weibull parameters are $\varepsilon_0 = 8.3$ x10^{-4} and $\beta = 6.0$. Reproduced from [6].

Sample size was kept to 30 for the Weibull parameter and mesh sensitivity testing in order to be able to test mesh parameters in a time-effective manner. However, for future use of this method it would be useful to test a larger sample, to somewhat negate the effects of the variance and bias discussed in Section 3.3. This test was carried out using Weibull parameters of $\beta = 10$ and $\varepsilon_0 = 8.3 \times 10^{-4}$, internodal spacing of 0.5 mm, and horizon ratio $m = 3$. The resulting Weibull parameters were $\varepsilon_{0,\text{Stage 2}} = 8.481 \times 10^{-4}$ and $\beta_{Stage\ 2} = 11.16$. This compares interestingly to the results in Table 5-1, in that the Weibull modulus error almost perfectly matches the 12% error in the higher modulus samples there. From that it is reasonable to draw the conclusion that this error is inherent to this application of Weibull distributions in peridynamics, and was not simply the result of random variation. In contrast, the characteristic strain at stage 2 failure in the larger sample has < 2% error relative to the intended value, where this

value had been around 8% in the smaller samples, even in cases where the modulus was > 10, which would be expected to produce smaller errors of this kind. This is evidence, though not overwhelming, that some significant part of the error in characteristic strain shown in Table 5-1 can be attributed to the small sample size bias discussed in Section 3.3. It is likely that much of the error is attributable to simple variance from sample to sample, which coincidentally resulted in similar error.

The difference between stage 1 and stage 2 failure is in most cases negligible, (see Figure 5-13) although there are a few isolated cases where it is noticeable in the lower tail of the distribution. Notably, this is not responsible for the difference between the intended and resulting distribution at the lower tail, as the stage 1 failure values are also higher than expected in the lower tail.

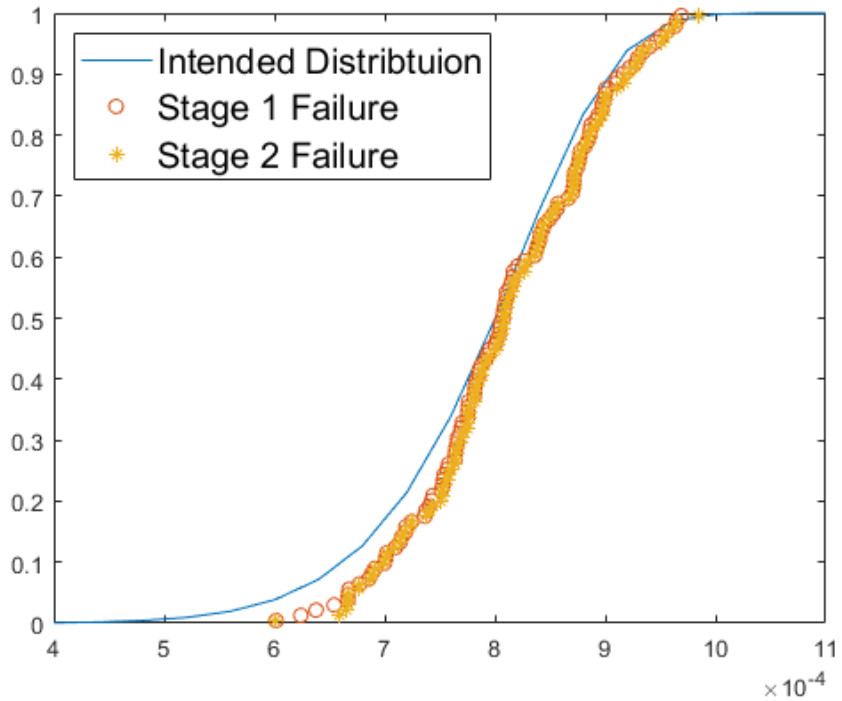

Figure 5-13 The stage 1 (failure of a single bond) and stage 2 (fracture of the overall part modelled) failure strains plotted relative to the intended distribtuion of $\varepsilon_0 = 8.3 \times 10^{-4}$ and $\beta = 10$ using the edge-only method of critical strain randomisation. Reproduced from [6].

5.4 Discussion

The first key finding upon using the Weibull peridynamics formulation from Chapter 4 in two dimensions is that scaling the Weibull distribution according to edge-length is more accurate than scaling according to total material point number, at least in loading regimes where fracture is expected to occur at edges. Although scaling for edge length is not sufficient to make the method perfectly accurate, it is considerably better than using the total number of material points, and it was established in Chapter 4 that failing to use Weibull scaling at all is also inaccurate.

Attempts to make the method considerably more accurate than the initial edge-scaled version were affected by effectively the same issue as occurred in 1-dimension: after damage is initiated, it does not always propagate immediately, and this error is greater at lower initial fracture strain. Unlike in 1-dimension, it was not possible to entirely solve this problem in 2-dimensions. Even after altering the method to only use Weibull-randomisation at the edges, where fracture was expected to occur, there was still a relatively consistent error in that the output characteristic strains were larger than the intended value.

The method was determined to be insensitive to variations in mesh refinement as long as at least 119 material points (corresponding to 0.8mm node-spacing in this case, when accounting for the bonds which could not be broken near the ends of the bar) were used on each edge. Significant sensitivity was seen when varying horizon ratio, though. This effectively precludes the use of horizon sizes other than 3 in future work using this formulation. This, however, is the most typical horizon size [8] so being constrained in this sense is not a serious problem for the method.

Despite the ways in which this method is imperfect, it does succeed in recreating given Weibull distributions with sufficient accuracy that many different Weibull parameters can be used with reasonable confidence, especially in the case of Weibull moduli ≥ 10. This would allow experimentally measured behaviour to be accurately modelled. With the caveat that any output distribution will be slightly steeper than intended, a Weibull distribution can be used in peridynamics simulations using the method outlined in this work to examine the effects of varying Weibull modulus in different loading situations.

The form of randomisation used in this work may be considered continuous, since each material point is assigned its own value. This leads to many more critical strain values than Casolo and Diana's [7] discrete randomisation scheme, which was restricted to 25. It is noted by Casolo and Diana that this discrete method produces a discrete output in terms of stage 1 failure, the stress at which the first bond fails. Since there are a limited number of bond critical stress values, stage 1 is forced to occur at one of these. Stage 2 failure meanwhile is a more global phenomenon and this allows for the strengths of the part to be sufficiently "smeared" and the results appear continuous.

The randomisation in Casolo and Diana's peridynamics model was applied to all bonds in the mesh with the volume of all material points considered individually. Whether this contributed to the appearance of the two stage failure process is not clear, but it would follow logically that this may be the case, since it would result in large variations in strength between bonds, potentially retarding crack growth.

The result of a two-stage failure process is presented by Casolo and Diana as desirable, and a good representation of fracture of heterogeneous material. While this may be the case in the glasses that Casolo and Diana were attempting to model, 2 stage failure characterised by reaching the elastic limit before full fracture only occurring after a ~10% increase in stress is not a behaviour that would be expected in an engineering ceramic. For this reason, it was prioritised in this work to reduce the gap between stage-1 and stage-2 failure as far as possible. This priority is the primary justification for the use of the edge-only method over using Weibull-type randomisation for all bonds in the mesh, since the edge-only method improved the accuracy the stage 2 failure distribution without significantly altering the stage 1 failure distribution, which was largely accurate in either case.

Casolo and Diana accept the large increase in Weibull modulus as a limitation in their model, stating that Weibull modulus is not a material property and is relative to object geometry. In this chapter, the source of this error is investigated, and is identified as being largely attributable to low Weibull modulus, and also to cracks not immediately propagating after nucleation. The latter issue is partially solved by using Weibull-type randomisation on only material points on the edges where fracture is expected, while the former is thoroughly investigated. A lower limit of Weibull modulus $\beta = 7.5$ is established, and a very accurate result at $\beta = 10$ is shown, meaning such Weibull moduli can be used with confidence in future applications.

5.5 Conclusions

- By continuously randomising bond strengths relative to a Weibull distribution in a two-dimensional peridynamics model, a Weibull distribution was

recreated accurately. This is limited to Weibull distributions with modulus, β, $\leq$ 7.5, and peridynamics models with horizon ratio, m, = 3.

- Using Weibull moduli β < 10 in a two-dimensional peridynamics model resulted in a two-stage fracture process, with significant additional strain incurred between the failure of the first bond, and the overall fracture of the modelled object.
- Two-dimensional peridynamics models of tensile tests are best scaled for Weibull distributions by the length of the edges of the mesh parallel to loading. Scaling according to the total area of the two-dimensional model results in bonds that are much stronger than the intended fracture distribution.
- Weibull distributions were more accurately recreated when only the fracture criterion of the bonds connected to an edge material point were randomised according to a Weibull distribution. Randomising all bond strengths across the modelled object resulted in large variations in strengths within the interior of the modelled object, slowing crack growth in an unrealistic manner.

5.6 References

[1] M. Ho, E. Obbard, P. A. Burr, and G. Yeoh, "A review on the development of nuclear power reactors," *Energy Procedia*, vol. 160, pp. 459–466, Feb. 2019, doi: 10.1016/j.egypro.2019.02.193.

[2] X.-P. Xu and A. Needleman, "Numerical simulations of fast crack growth in brittle solids," *J. Mech. Phys. Solids*, vol. 42, no. 9, pp. 1397–1434, Sep. 1994, doi: 10.1016/0022-5096(94)90003-5.

[3] A. Bhushan *et al.*, "Weibull Effective Volumes, Surfaces, and Strength Scaling for Cylindrical Flexure Specimens Having Bi-Modularity," *J. Test. Eval.*, vol. 44, Sep. 2016, doi: 10.1520/JTE20150301.

[4] G. D. Quinn, "Weibull Effective Volumes and Surfaces for Cylindrical Rods Loaded in Flexure," *J. Am. Ceram. Soc.*, vol. 86, no. 3, pp. 475–479, 2003, doi: 10.1111/j.1151-2916.2003.tb03324.x.

[5] D. Petersen, R. Link, S. Duffy, E. Baker, A. Wereszczak, and J. Swab, “Weibull Analysis Effective Volume and Effective Area for a Ceramic C-Ring Test Specimen,” *J. Test. Eval.*, vol. 33, no. 4, p. 12617, 2005, doi: 10.1520/JTE12617.
[6] L. D. Jones, L. J. Vandeperre, T. A. Haynes, and M. R. Wenman, “Modelling of Weibull Distributions in Brittle Solids Using 2-Dimensional Peridynamics,” *Procedia Struct. Integr.*, vol. 28, pp. 1856–1874, Jan. 2020, doi: 10.1016/j.prostr.2020.11.009.
[7] S. Casolo and V. Diana, “Modelling laminated glass beam failure via stochastic rigid body-spring model and bond-based peridynamics,” *Eng. Fract. Mech.*, vol. 190, pp. 331–346, Mar. 2018, doi: 10.1016/j.engfracmech.2017.12.028.
[8] F. Bobaru and W. Hu, “The Meaning, Selection, and Use of the Peridynamic Horizon and its Relation to Crack Branching in Brittle Materials,” *Int. J. Fract.*, vol. 176, no. 2, pp. 215–222, Aug. 2012, doi: 10.1007/s10704-012-9725-z.

Chapter 6 Application of Weibull Fracture Strength Distributions to PWR Fuel Pellet Simulations in Peridynamics

This Chapter is based on work submitted to the Journal of Nuclear Materials in July 2022, under the title "Application of Weibull Fracture Strength Distributions to Modelling Crack Initiation Behaviour in Nuclear Fuel Pellets Using Peridynamics", manuscript number JNUMA-D-22-00832. A pre-review manuscript of that same paper was also published on engrxiv.

6.1 Introduction

Modelling fracture explicitly in nuclear fuel pellets has the potential to offer a great deal of qualitative insight into the process of cracking of in-service fuel. In order for this insight to be useful though, these explicit methods must first be shown to match the quantitative data that exist on fuel pellet crack patterns observed in post irradiation examinations (PIE). Walton and Husser [1] counted radial cracks on low burnup (< 5 GWd mtU^{-1}) PWR pellets after power ramps to various linear power ratings. Barani et al. [2] later fit a curve to the Walton and Husser data using the formula

$$n = 0 \; if \; LHR < LHR_0$$

$$n = n_0 + (n_\infty - n_0)\left[1 - exp\left(-\frac{LHR - LHR_0}{\tau}\right)\right] \; if \; LHR \geq LHR_0 \qquad (6.1)$$

Where n is the number of cracks, n_∞ is the number of cracks at an arbitrarily high linear heat rate (set to 12 to fit the Walton & Husser data), n_0 is the number of cracks at the initial cracking event; LHR is the linear heat rate in kW m^{-1}; LHR_0 is the linear heat

rate at the appearance of the first crack (set to 5 to fit the Walton & Husser data) and τ is a fitting parameter describing the curve, set to 21 to fit the Walton and Husser data.

The Walton and Husser PIE data is compared in Figure 6-1 to three explicit crack modelling papers. Both the models of Huang et al. [3] and Jiang et al. [4] fit the Walton and Husser data remarkably well, given that neither makes reference to it in their work. However, it is notable that Huang et al. makes reference to Oguma's model [5]. Huang et al. claim that the roughly linear nature of the increase in radial cracks with power, shown in their paper, is evidence of their model's validity. The results of the simulations by Wang et al. [6] do not fit the trend well, but this is to be expected, since in that case temperature was ramped very quickly, and the cracking was driven by thermal shock.

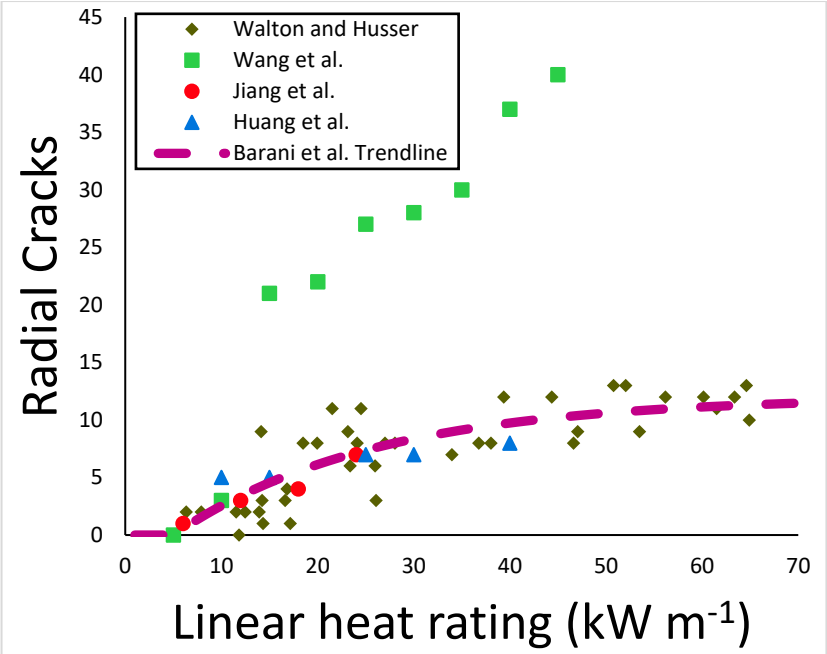

Figure 6-1 Radial crack numbers observed in PIE by Walton & Husser [1], and the curve fit to that data by Barani et al. [2] alongside the number of cracks at given linear ratings in simulated pellets as modelled by Huang et. al [3], Jiang et al. [4] Wang et al. [7].

Other significant explicit crack modelling of PWR nuclear fuel not shown in Figure 6-1 include that of Oterkus and Madenci [8] and Li and Shirvan [9]. In both these cases, all cracks seem to initiate at once, so they do not appear to be appropriate for comparison to the Walton and Husser [1] data. In the case of Oterkus and Madenci, [8] this is due to a difference in the heating regime. Instead of following a semi-realistic power ramp history, the power in the pellet is instantaneously set to a given level, before allowing the temperature to equilibrate. This regime more closely resembles the thermal shock in the work by Wang et al. [7] than the Walton and Husser data. It is not made clear in the work by Wang et al. whether the cracks initiate all at once, or consecutively.

Li and Shirvan [9] however, follow a power ramp up and down over the course of ~3 days, with the intention of mimicking a real reactor power history. The radial cracks all nucleate during the initial part of the power rise to 18 kW m^{-1}, and no new cracks initiate during the following rise to 35 kW m^{-1} (see Figure 6-2). This finding seems to conflict with the findings of Walton and Husser. A possible explanation for this difference reported in (12) is that the cracks that form due to the initial power rise are all very small, and then significant growth occurs in several cracks by the time the linear rating reaches 35 kW m^{-1}. It is plausible that Li and Shirvan's model barely differs from the reality Walton and Husser observed, if the small cracks seen in Li and Shirvan's model were missed or dismissed by Walton and Husser. Had Walton and Husser been presented with a pellet cracked similarly to Li and Shirvan's 35 kWm^{-1} snapshot, they could reasonably have counted 5-13 radial cracks, since the very small

ones would be much harder to see in PIE, once the pellet has cooled. This could be consistent with the Walton and Husser data.

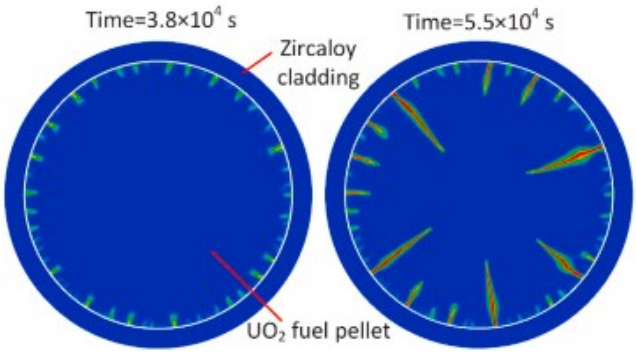

Figure 6-2 Images of a cracked fuel pellet modelled by Li and Shirvan[9] using a phase field method. It can be seen in (a) that cracks largely nucleate together at ~5 km^{-1}, before in (b) certain cracks grow preferentially over others at ~10 kWm^{-1}. Reproduced from [9].

The randomness of fracture strength in brittle materials is represented in a number of different ways in the various explicit nuclear fuel cracking models. In some models it is quite explicitly considered, such as by Oterkus and Madenci [8] who used a Gaussian distribution for failure strain applied to the peridynamics bonds with mean value of 10^{-3} and standard deviation of 10^{-4}, which roughly corresponds to a Weibull distribution with characteristic value 10^{-3} and a Weibull modulus of 10. In other cases, such as the work by Wang et al. [7], no mention is given to this randomness at all, but the crack patterns are not obviously symmetrical, so it may be assumed that some small degree of heterogeneity was used or possibly introduced inadvertently due to numerical rounding in creating the mesh. The degree of randomness in the discrete element modelling (DEM) model by Huang et al. [3] is hard to compare to the other methods. I n this case it stems from the size of the nodes, which vary according to a uniform distribution, rather than a model property analogous to some material property, like the strength variations in other work. That only one result is given suggests that using a different random seed would not materially change the results or

it was simply not considered. The phase-field model by Li and Shirvan [9] uses a Weibull distribution of critical fracture strength with parameters of characteristic stress, $\sigma_c = 60$ MPa and Weibull modulus, $\beta = 50$. Also of interest is the work by Mella involving lattice site perturbation as a method for introducing heterogeneity sufficient to prevent mesh dependent crack nucleation behaviour [10]. It was found that nodal perturbation did reduce the influence of the mesh on the crack patterns, and did not alter the macroscopic properties of the material. Mella and Wenman [11] found in their LAMMPs implementation of peridynamics that heterogeneity stemming only from rounding errors in the numerical implementation of peridynamics was sufficient to produce a distribution of crack numbers in an advanced gas-cooled reactor pellet similar to PIE data.

Objects made of typical structural engineering ceramics have Weibull moduli of around 10, with materials such as chalk, brick, stone and pottery having lower values of around 5 [12]. This variation roughly corresponds to the regime used by Oterkus and Madenci [8], but is significantly greater than the nominal variation in properties used in other explicit pellet cracking models such as Huang et al.[3], Wang et al. [7], or Li and Shirvan [9]. Compounding this, the distribution must be scaled according to the difference in size between the constituent parts of the model (material points in peridynamics) and the engineering scale object in question in order to reproduce Weibull distributions accurately, as shown by the authors in previous work [13], [14] and in chapter 4 and 5. This is done by increasing the characteristic value, which also increases the difference in the variation of strength between low and high P_f values. Using a distribution of bond strengths, intended to reproduce a real fracture

distribution, produces much more variability, than the nominal variation typically used in fracture modelling.

It is considered here that modelling the simple thermo-mechanical processes is sufficient to get some idea of the reality of initial fuel pellet fracture (i.e. early life behaviour). In order to get a more complete fuel life picture, additional processes must be iteratively added to the model, as Oterkus and Madenci [8], for example, did with oxygen diffusion. In this chapter, it is proposed that the introduction of realistic fracture strength distributions, modelled here as Weibull distributions, are a material property worthy of consideration in accurately reproducing nuclear fuel pellet fracture. A method for appropriately modelling them, based on the 2D method outlined by the authors in [13] is included, and the effects of such a distribution on the number of radial cracks at the end of a power ramp are discussed with respect to other works and PIE data.

6.2 Methodology

The method in Chapter 5 was shown to recreate Weibull distributions with reasonable accuracy in a 2-dimensional representation of a tensile test. The surface of an expanding circle, such as the pellet slice modelled in this work, may be considered analogous to the surface of a 2-dimensional tensile test specimen, since the surface stress is ostensibly uniformly distributed in both cases. 2-dimension Weibull peridynamic bodies have an additional complication relative to 1-dimension peridynamic bodies in that crack propagation must be considered. This is doubly true in the fuel pellet scenario, as the hoop stress at the tip of ingrowing radial cracks

decreases as the cracks grow inward, and the tip moves towards the centre of the pellet, where the stress is compressive.

In contrast to real materials, initiation and propagation of cracks in 2-dimension peridynamics bodies of the kind modelled in this work are fundamentally separate processes. In real brittle materials, Griffith's criterion [15] describes the process of cracking, and allows only for growing, shrinking and (in equilibrium) stable cracks. It makes no mention of the initiation of cracks. Cracks are presumed to exist, in a way that they do not in continuum models. This difference is the reason for the randomisation of the properties of some bonds in order to recreate the properties of a Weibull distribution.

Peculiarly, Weibull makes the opposite assumption about fracture. There are no rules for the growth of cracks, only initiation. Fracture in Weibull analysis is a single event, not a process. This contradiction can be reconciled by having Weibull analysis govern the bonds involved in fracture initiation, (i.e. the surface) and cracks in the bulk governed by a single value strain criterion. Inherent to this method is an assumption that cracks initiate solely on the surface which, given the stress profile, seems a safe one. Through this split-regime method, crack initiation can be defined by strain as this was shown by the authors to be possible to calibrate to a Weibull distribution in [13]. Given the potentially large differences between the bulk values and the Weibull-randomised surface values, it was necessary to create a region of thickness equal to one horizon radius at (i.e. three nodal spacings) the surface for the Weibull values (see Figure 6-3). This allows for nucleated cracks to grow a small distance while still governed by the Weibull values.

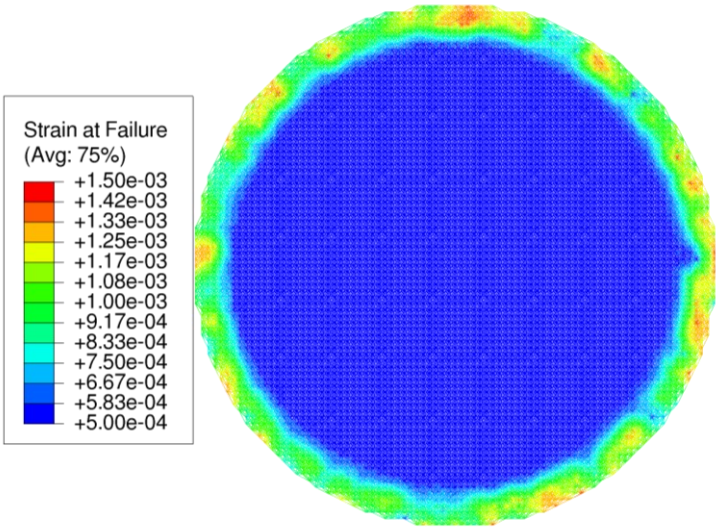

Figure 6-3 The failure strains of bonds attached to nodes within one horizon of the surface were randomised according to a Weibull distribution, with Weibull modulus β = 10, characteristic strain $\varepsilon_0 = 5.34 \times 10^{-4}$ and using size scaling to account for the difference in size between peridynamics bonds and the pellet. The bonds in the bulk were assigned a fixed value equal to the characteristic strain.

6.2.1 Boundary Conditions & Mesh

The mesh was square shaped, with 0.1 mm nodal spacing. The results of Chapter 5 would suggest that a mesh spacing of 0.08mm or lower would be preferable, but the size of the objects is slightly different. In the case of a circular mesh with a diameter of 8.2 mm the circumference is ~256 times greater than a 0.1 mm nodal spacing. This corresponds quite closely to the ratio in the 0.8mm case demonstrated in the tensile tests in chapter 5. In that case the effective surface length was equivalent to 230 nodal spacings, after accounting for the buffer zones at either end where the bonds cannot be broken. The horizon ratio m, was set to 3. This material point spacing is below the convergence size relative to the overall mesh found in chapter 1, and the horizon ratio is typical in peridynamics work in the literature [16], [17]. Given the results of the mesh refinement sensitivity study in Chapter 5, it was thought that using a finer mesh would not produce significantly different crack patterns or radial crack numbers.

In order to constrain the pellet, 2 perpendicular lines of nodes, intersecting at the centre, were restricted to have zero movement in the hoop direction. This forced the pellet to grow concentrically, and not move from its original position. To achieve this in Abaqus, lines of nodes in the x and y direction were included in 2 boundary conditions to restrict their movement in the y and x direction, respectively. This boundary condition regime may have had the effect of preventing through cracks, but it was necessary in order to run the simulations. A similar effect could be achieved by using an encastre boundary condition on only the central node, but this results in instability in the simulation due to large reaction forces exerted on that node..

Should the pellet fragment, these constraints are no longer sufficient, since a fragment may no longer be connected to any constrained nodes. Extra truss elements were inserted, connecting the central node to all surface nodes. These truss elements have the same material properties as the main peridynamics bonds, meaning they expand at the same rate, so apply minimal force to surface nodes, causing less than a 1% variation in maximum displacement of surface nodes (see Table 6-1). They were assigned an arbitrarily high fracture strain, assuring that they would never break. When a fragment breaks free from the constrained portion of the pellet, the stiffness of these additional trusses constrains the fragment.

Table 6-1 Maximum displacements of nodes in simulations with no fracture.

	Maximum displacement (10^{-2} mm)
Finite element model	7.612

Peridynamics with support trusses	7.597
Peridynamics without support trusses	7.555

Since the model is only of a 2D "slice" of a pellet, the additional unbroken truss elements also act as a proxy for the remaining pellet above and below this slice, preventing the pellet from moving too freely. Without this constraint, cracks can curve artificially due to the inertia of fragments shearing away from the centre, which can lead to unrealistic crack paths growing in an outward radial direction. The effect of these additional trusses is shown in Figure 6-4. A possible reason for this curving is the lack of including a contact behaviour between newly created crack face "surfaces" in this implementation of peridynamics. Pellet fragments are free to move without regard for contact between these surfaces, causing spurious crack curvature and branching. This movement also reduced the stability of the simulations, slowing them down, and often leading to the model crashing.

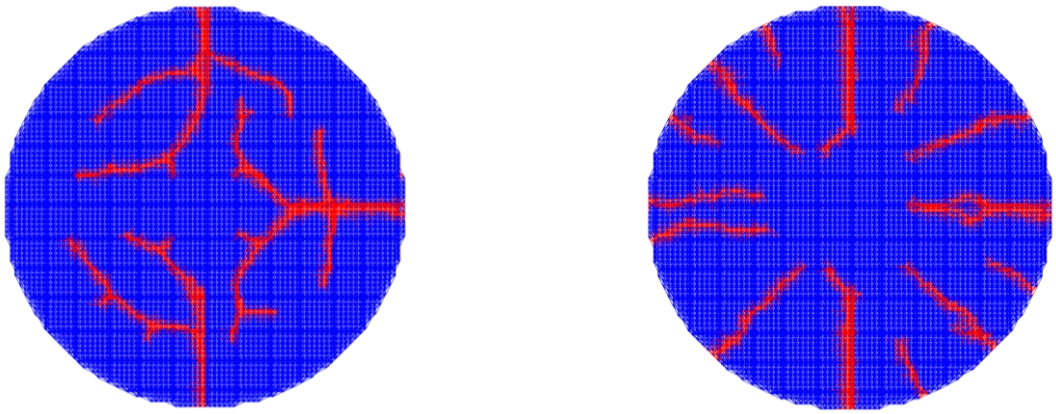

(a) (b)

Figure 6-4 (a) Curved cracks in the absence of supporting trusses, (b) Relatively straight cracks observed when using supporting trusses. Bond strengths were as given in figure 6-3 in both cases, and both (a) and (b) show pellets ramped to 40 kWm^{-1}.

There is agreement in the literature that ramping to higher powers over similar periods of time results in more radial cracks around the surface of a nuclear fuel pellet, although there is some disagreement as to the provenance of such cracks. With this in mind, a test was performed to ramp pellets from 0 kW m^{-1} up to a 70 kW m^{-1}. The pellet was ramped up to 70 kW m^{-1} over 10^3s. The intention was to avoid the thermal shock that has been explored in peridynamics by Oterkus & Madenci [8] and Wang et al. [7], and instead show cracking as it occurs in a fuel pellet heating up over industrial timescales of the order of days rather than seconds.

Implementing a heat transfer model in peridynamics requires a temperature convergence criterion, and therefore short time increments, which is computationally expensive. This would negate the advantage of the variable incrementation regime used. Instead, temperatures were determined by an ENIGMA fuel performance code (NNL version) run [18], and then applied to the nodes of the peridynamics model. ENIGMA is the primary UK computer code for thermal reactor fuel performance analysis [19] and can be used to calculate the thermo-mechanical behaviour of either LWR or AGR fuel pellets in steady-state or transient conditions. ENIGMA is validated against a large database of LWR fuel irradiations.

Surface temperatures, T_s and the centreline temperature T_c were applied exactly, with a simple parabola in between.

$$T_{node} = T_C - ((T_C - T_S) * r^2) \tag{6.2}$$

Where T_C is the centreline temperature defined by the ENIGMA calculations, T_S is the surface temperature defined by the ENIGMA calculations, and r is the distance

between the centre of the pellet and the node in question, normalised such that for the surface nodes $r = 1$:

$$r = \frac{(Dist_{Centre-Node})}{MAX(Dist_{Centre-Node})} \tag{6.3}$$

The effects of cracks on temperature distribution are not considered, but this solution allows for temperature to be computed cheaply, and for a larger sample of pellets to be generated. The modelled centreline temperatures reach 2727 K, sufficiently close to the melting point to induce significant changes in material properties, which are for the most part neglected.

Temperatures were defined by ENIGMA at ~714 s intervals, equivalent to an increase in power of 5 kW m^{-1}. The peridynamics model used a linear interpolation method to determine centreline and surface temperatures between these times. There was no user applied control on the time incrementation requiring time, t, to match these defined times exactly, so there were increments with some "*overshoot*" (see Figure 6-5) where temperature increased according to the gradient between t_{n-1} and t_n to a time $t > t_n$ *where* n is the increment number. Since the gradient between t_n and t_{n+1} is different, this produced a small error. If, on the next increment, T were to be defined according to a linear interpolation between T_n and T_{n+1}, there would be a sharp change to correct this error, which in some cases induced a thermal shock sufficient to nucleate a number of small cracks. In order to avoid this, temperatures at the end of increments ($T_{c,\,End}$ and $T_{s,\,End}$ for the centre and surface temperatures respectively) were defined according to a linear interpolation between the temperature at the start of an increment ($T_{c,\,Start}$ and

$T_{s,\,Start}$) and the next defined temperature from the ENIGMA model. This allowed the error to correct slowly over time according to equations 4 and 5

$$T_{c,End} = (T_{c,Next} - T_{c,Start}) * (t_{Next} - t_{Start}) \quad (6.4)$$

$$T_{s,End} = (T_{s,Next} - T_{s,Start}) * (t_{Next} - t_{Start}). \quad (6.5)$$

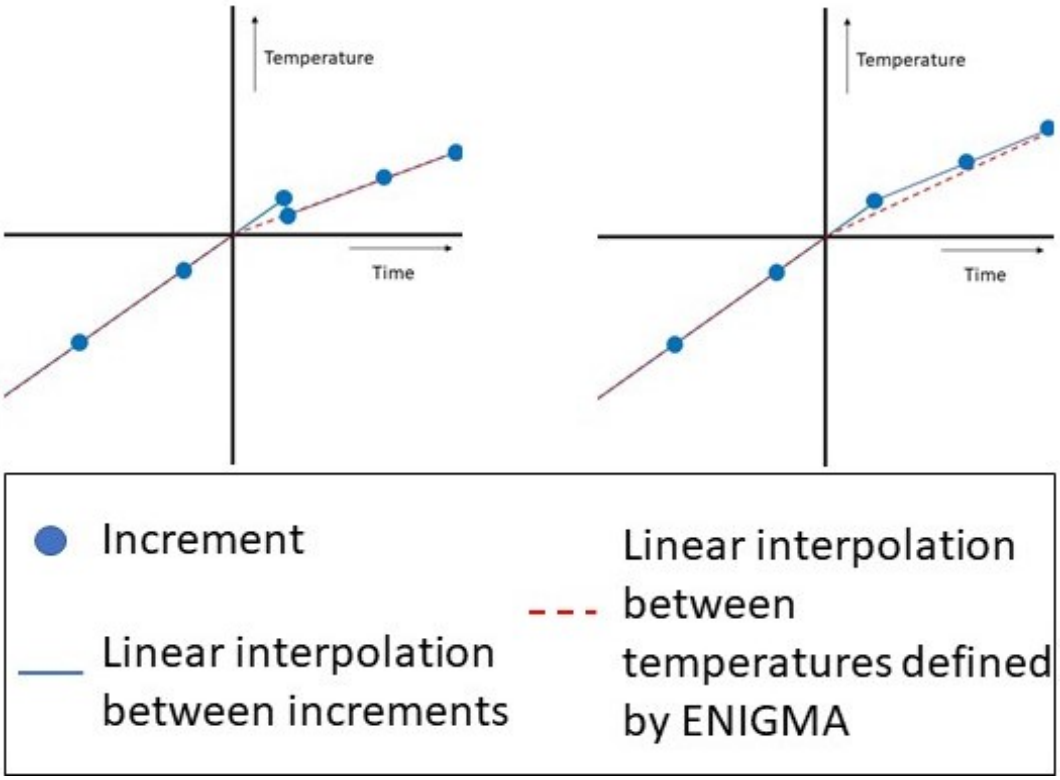

Figure 6-5 The temperature at a node at a particular time is determined by interpolating between a past temperature and a future temperature determined by ENIGMA. (b) The temperature at a node at a particular time is determined by interpolating between the current temperature and a future temperature determined by ENIGMA. This avoids sharp temperature drops, which can cause artificial nucleation of cracks.

The resulting temperature profile is a perfect parabola (see Figure 6-6), which does not perfectly match the shape described by ENIGMA. The errors are considered small though, with the largest being ~1%. The effects of cracks on temperature distribution are not considered but given the temperature gradient is radial and cracks are radial they should have minimal impact. The circumferential cracks that form on the power down ramp would impact the temperature distribution at that point, but it is not believed that this including variation would affect the final radial cack numbers. Despite these limitations, this solution allows for temperature to be computed cheaply, and for a larger sample of pellets to be generated while still utilising the complex and well-benchmarked solution for temperatures found in ENIGMA, including effects such as thermal conductivity degradation.

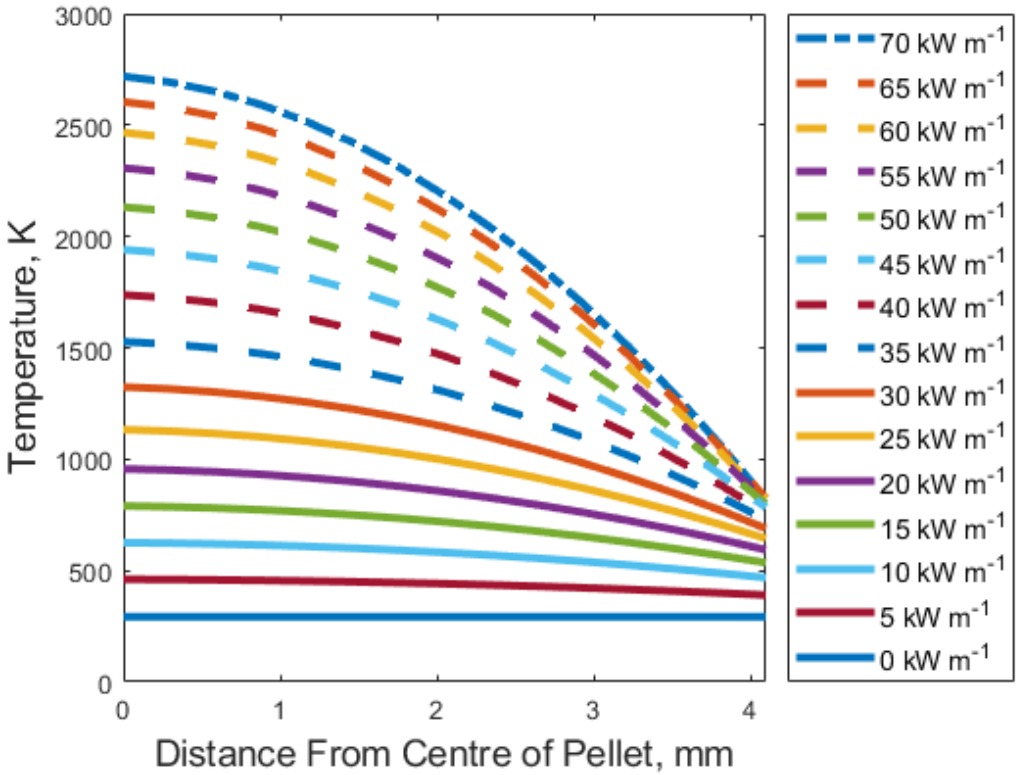

Figure 6-6 Temperature profiles for the peridynamics models of PWR fuel pellets on a 10,000s ramp up to 70 kW m^{-1}. The centre and surface temperatures are taken from ENIGMA calculations, and a parabolic relation is used to calculate the temperatures in between.

6.2.2 Material Properties

The UO_2 pellet was defined by the material properties given in Table 6-2. The elastic modulus was temperature dependent, but all other properties in the peridynamics model were not. For the elastic modulus calculation, D represents the fraction of theoretical density, which is set to 0.95, and T is temperature in Kelvin. The fracture strain is determined based on the fracture stress and elastic modulus at 500 K, calculated from [20].

Table 6-2 Material properties used for the UO_2 fuel simulations.

Property	Unit	Value/Formula	Reference
Elastic Modulus	MPa	$2.334 \times 10^{11}[1 - 2.752(1 - D)][1 - 1.0915 \times 10^{-4}\ T]$	[20]
Fracture Strain	-	5.64×10^{-4}	[20]
Thermal Conductivity	$J\ K^{-1}\ m^{-1}$	ENIGMA-B	ENIGMA-B
Coefficient of Thermal Expansion	-	10^{-5}	[20]
Specific Heat Capacity	$J\ kg^{-1}\ K^{-1}$	ENIGMA-B	ENIGMA-B
Density	$Kg\ m^{-3}$	1096	[20]

6.2.3 Computational experiments

Since the work is of an inherently statistical nature, some thought is required to determine an appropriate sample size. Typically, a larger sample size will produce results more representative of the population, but that would not be a good like for like

comparison to the PIE data in this case. The intent was to compare the number of radial cracks in the peridynamic pellets to the real cracks observed by Walton and Husser [1] using the parameters of Barani et al. [2]. A larger sample size would lead to an increased likelihood of a low probability event, such as a very large number of cracks. This could lead to an increase in the n_∞ parameter, simply as a result of observing a larger sample size. In reference [1] a total of 45 pellets, after ramping to a range of powers from 7 – 65 kW m^{-1}, were observed. This is replicated in the peridynamics simulations, with 45 pellets, each ramped to a power corresponding to one of the pellets observed in [1].

In order to measure the closeness of fit between the data from [1] and that from the peridynamics simulations, the formula used by Barani et al. [2] to fit a curve to the data from [1] was used to plot a line of best fit for the peridynamics data. The parameters, which produced the lowest χ^2 compared to the simulation results were used. The difference between the parameters used by Barani et al. and those used for each of the peridynamics models serves as a measure for the difference between the Walton and Husser data and the peridynamics.

Despite the lack of pellets ramped to less than 5 kW m^{-1}, this is a reasonable estimate for the power at first cracking and this parameter is kept the same for all curves plotted in this work. The same is true for the number of cracks at first failure, n_0. Although no data is shown in this work where a single crack is present, this was observed to be possible in all cases except the *naïve* case where the Weibull shape parameter was arbitrarily high ($\beta = 10^5$) i.e. single fracture strength. The parameters for each set of

peridynamics data were chosen based on the lowest possible χ-squared value for parameters using only integers.

Finally, to briefly demonstrate the necessity of some level of fracture strain randomisation, a pellet was simulated with surface bonds randomised according to a distribution with a Weibull modulus of 10^5 i.e. effectively an infinite Weibull modulus.

6.3 Results

Differences in failure strain for the pellet with Weibull modulus of 10^5 were negligible. The pellet fractured perfectly symmetrically, with 8 radial cracks initiating on the points most distant from the centre at around 5 kW m^{-1}. It continued to fracture symmetrically, with multiple cracks initiating at once, in 3 fracture events. 16 cracks is more than would be expected based on the Walton and Husser data, and they occur in a pattern that does not fit the PIE data or the curve from Barani et al. [2].

When the relationship of number of cracks against the linear rating at which they occur is plotted, (see Figure 6-7) it does not seem to show the characteristic exponential shape as described by Barani et al. [2]. It is possible that after the first group of 4 simultaneous cracks, there is a more linear shape to the distribution. The best possible fit of a Barani-type exponential curve was to use parameters of $n_0 = 8$, $n_\infty = 20$, $LHR_0 = 5$ kW m^{-1}, and $\tau = 5$, although with only 3 data points, the curve does not fit the data well, and the parameters were calculated only for the purposes of comparison to later curves. The cracking of the pellet is shown in Figure 6-8.

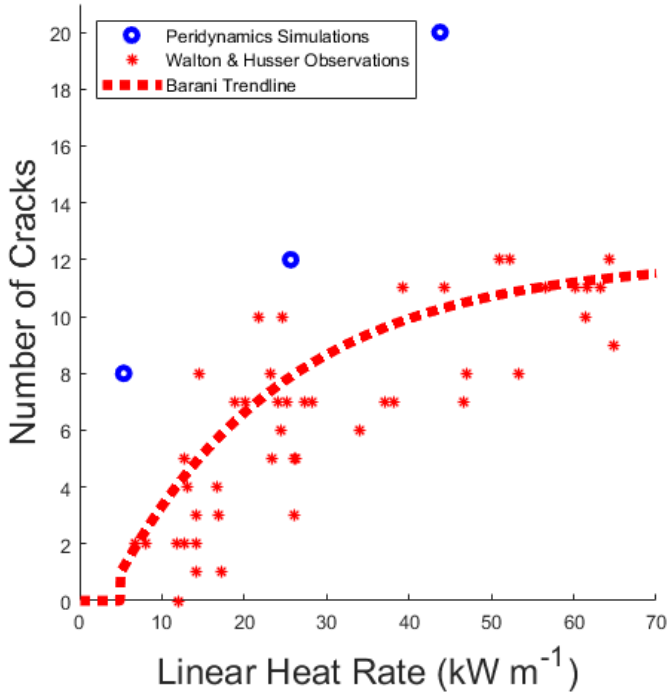

Figure 6-7 A comparison of the peridynamics with a Weibull shape factor β = 10^5 to the curve plotted by Barani et al. [2] to fit the PIE data in [1].

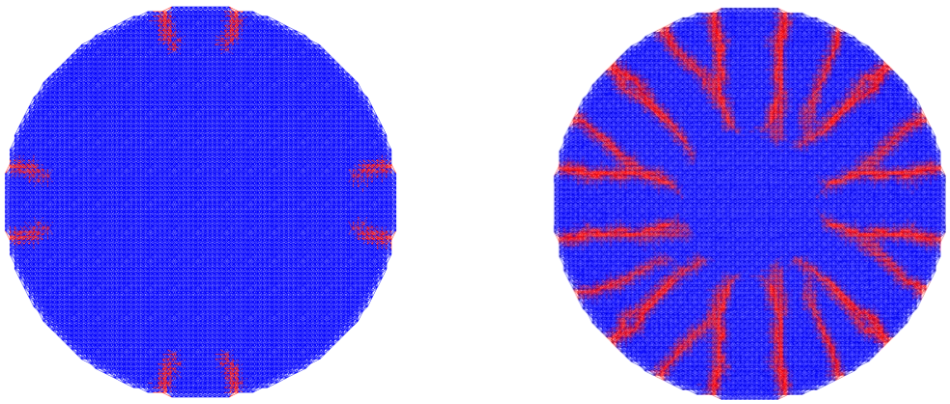

(a) (b)

Figure 6-8 shows the extent of cracking in the β = 10^5 case at (a) 5.35kW m^{-1} and (b) 70kW m^{-1}

Using a Weibull modulus of 10^5 is highly unlikely to produce realistic results and serves simply as a comparison point for the Weibull-randomised pellets. A more typical randomisation scheme would be to use a Weibull shape parameter of 10, with no size scaling. This in fact corresponds closely to the Gaussian randomisation used in reference [8] and is not too dissimilar from the Weibull distribution used by Li and Shirvan [9].

Plotting a Barani-type curve (see equation (6.1)) using the best-fit parameters of n_0 = 1, n_∞ = 25, LHR_0 = 5 kW m^{-1}, and τ = 30 against the curve fit to the Walton and Husser data shows a considerable overestimation in the number of cracks predicted at a given power, in relative terms at low power, and in absolute terms at higher power (see Figure 6-9).

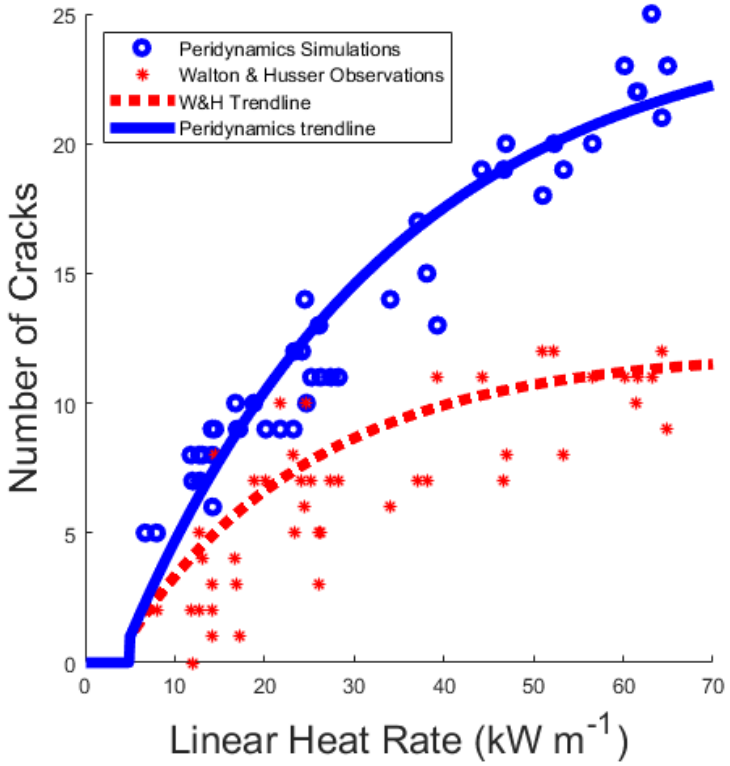

Figure 6-9 The data produced by recreating the experiment in [1] in peridynamics with a Weibull shape factor β = 10 but with no size scaling to account for the difference in size between bonds and the overall object compared to the curve Barani et al. [2] plotted to fit the PIE data in [1]

By using the size-scaling method outlined in the methodology section and keeping the Weibull shape factor at 10, this error can be reduced. Fitting an exponential curve to such data produces the parameters n_0 = 1, n_∞ = 17, LHR_0 = 5 kW m^{-1}, and τ = 25. This model data is close to the curve for the experimental data from [1] reasonably well up to around 30 kW m^{-1} but with increasing power this difference becomes significant (see Figure 6-10).

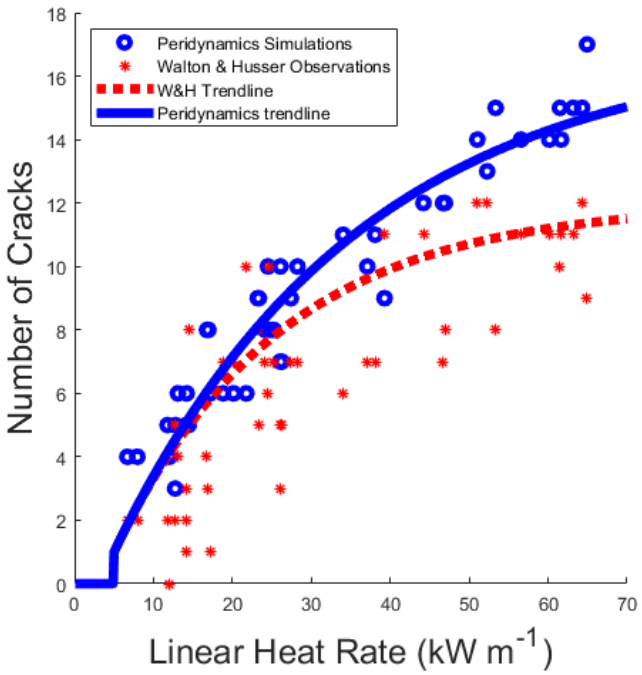

Figure 6-10 The data produced by recreating the experiment in [1] in peridynamics with a Weibull shape factor β = 10 with size scaling to account for the difference in size between bonds and the overall pellet, compared to the curve Barani et al. [2] plotted to fit the PIE data in [1].

Since the peridynamics simulations still result in significantly more cracks than were observed in the PIE, and there is evidence that using broader Weibull distributions produces lower crack numbers at very high power, which would fit closer to the data in [1], the experiment was repeated with a Weibull modulus of just 5. Several cracks appear above the n_∞ of 12 set, based on the Walton and Husser data, but otherwise this is a close fit to the curve that best describes the Walton and Husser data (see Figure 6-11). The parameters used to fit to the peridynamics model data were $n_0 = 1$, $n_\infty = 13$, $LHR_0 = 5$ kW m^{-1}, and $\tau = 25$.

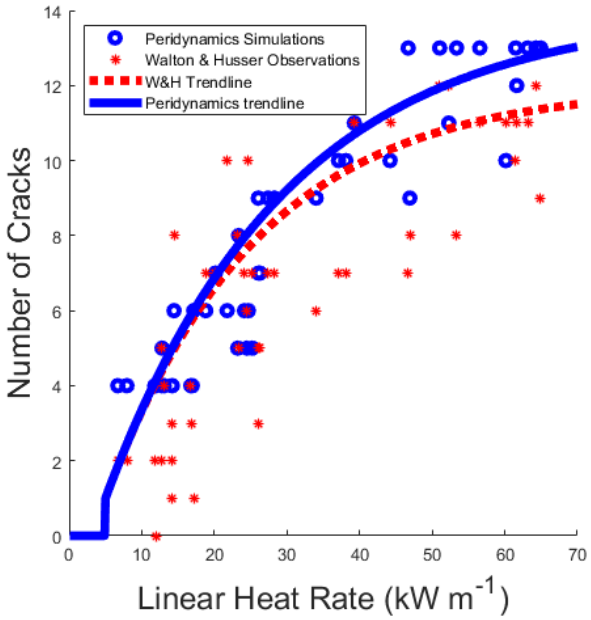

Figure 6-11 The data produced by recreating the experiment in [1] in peridynamics with a Weibull shape factor β = 5 with size scaling to account for the difference in size between bonds and the overall pellet compared to the curve Barani et al. [2] plotted to fit the data in [1].

A Weibull shape parameter of $\beta = 5$ is not fully supported by the method set out in [13] though, as it is below the lower bound of $\beta = 7.5$. Using a Weibull shape factor this low introduced a tendency for cracks to initiate in the bulk region, away from the surface, shown in Figure 6-12. Non-surface initiating cracks are an artefact of the simulation method, and not a good representation of the behaviour of the material in reality. These cracks were counted as surface cracks for the purposes of Figure 6-11.

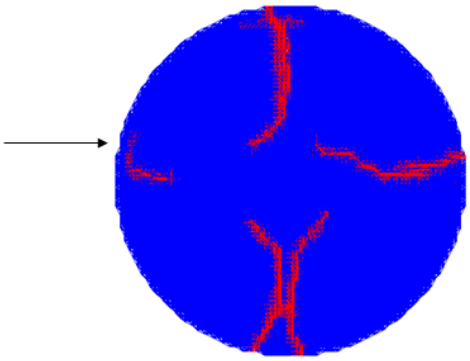

Figure 6-12 A pellet simulated with a Weibull shape factor β = 5, with an arrow highlighting a crack which nucleated in the bulk region of bonds, rather than at the surface. Red signifies broken bonds.

The parameters used to plot the curves in Figures 6 – 9 are collated in Table 6-3. Case 1 is the so-called *naïve* approach with essentially zero randomisation of material fracture strengths. Case 2 is the approach designed to be reasonably close to that of the fracture distributions used in other works, without surface size scaling. Case 3 uses the same Weibull shape parameter, (i.e. one that is reasonable for a ceramic of this type [12]) but also includes the size scaling effect between bonds and the peridynamic model. Case 4 is the attempt to attain a closer fit to the PIE data in [1] by means of using a smaller Weibull shape parameter.

Table 6-3 Parameters used for fitting curves in figures 6 -7 to 6-11.

Case	Weibull Shape Parameter β	Fitting Parameter τ	Maximum Number of Cracks n_∞
Original Data	N/A	21	12
1	10^5	5	20
2	10 (No Scaling)	30	25
3	10	25	17
4	5	25	13

Although case 4 shows the best fit to the original experimental data, the artificial crack nucleation it shows precludes the use of such low Weibull shape parameters. Case 3 is therefore the result most appropriate for guiding future work, given that it shows a good overall fit, especially at powers below 30 kW m^{-1}, bearing in mind that most LWRs typically operate well below this, and care would be needed to simulate high power accident conditions using this method.

Figure 6-13 shows the crack profile of a pellet ramped over 10,000 s to a linear rating of 70 kW m^{-1} before holding for 10,000 s and then ramping down over 10,000 s to 0 kW m^{-1}. Notable features include:

- Nucleation of a single crack at ~5 kW m^{-1} as predicted by Walton and Husser [1].
- Some evidence of hierarchical crack growth, with alternating longer and shorter cracks, paticularly in the higher power images.
- No additional radial cracks nucleate on the entirety of the ramp down, although in a few cases circumferential crack growth originating at the tips of radial cracks can be seen at the end of the ramp down.
- Radial cracks initiating at the tips of other approximately radial cracks. (See Figure 6-13 (i)). Although this growth could be an expression of a real physical phenomenon, it is more likely an artefact resulting from stress in the support trusses.

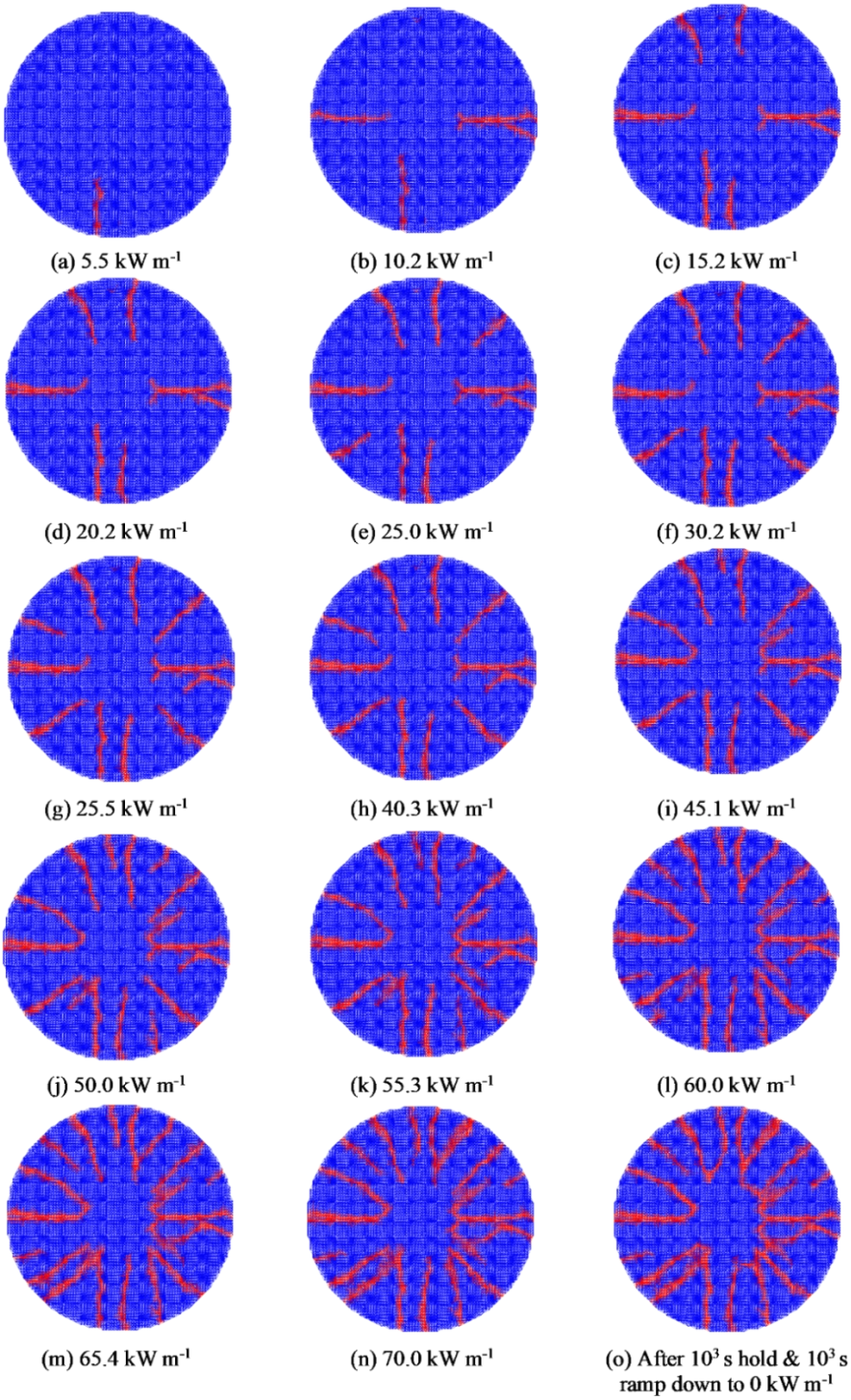

Figure 6-13 Crack patterns on a peridynamics model of a UO_2 a pellet ramped to 70 kW m^{-1} over 10^3 s then held at power and ramped down to 0 kW $^{-1}$ over 10^3 s. Red shows broken bonds, blue unbroken.

The method of using support trusses to prevent overlapping of the pellet causes the pellets to display broadly similar crack patterns regardless of Weibull modulus, with the exception of the symmetry in case 1 (see Figure 6-14). The cracks are broadly

straight, radial in nature and originate at the surface. In most cases there is also evidence of hierarchical crack growth, where the growth of roughly every second crack is stunted by the neighbouring cracks. It is, however, worth commenting on what effect a variation in radial crack number might have in reality. In [21] deviations in direction can be seen in what might be expected to be straight cracks where cracks are more isolated. This can be seen to some degree in some of the pellet modelling in the literature, particularly Huang et al. [3]. Cracks that deviate from a purely radial direction i.e. do not grow directly towards the centre of the pellet could affect the radial heat flow of the pellet, but the degree to which this is the case is not clear and not measurable by experiment. In any case, circumferential cracks are likely to grow on the first cool down of the pellet's lifetime, so the effect of radial crack curvature would be obscured by this.

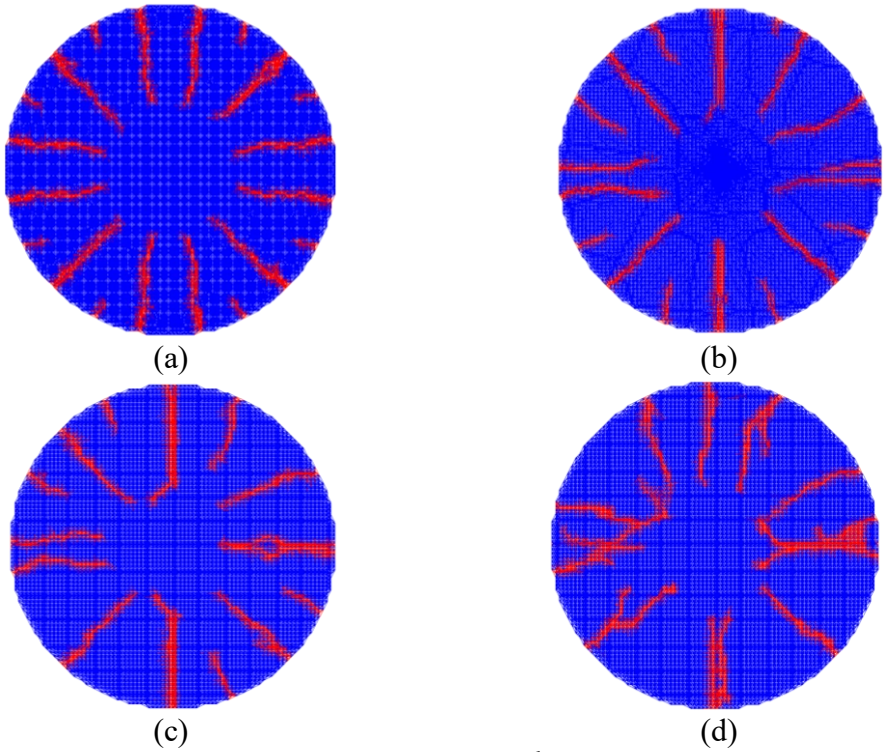

Figure 6-14 Crack patterns after ramping up to 45 kW m^{-1} over ~6,500s using (a) Case 1 (b) Case 2 (c) Case 3 (d) Case 4 bond strength randomisation.

6.4 Discussion

The Walton and Husser data suggests that the number of cracks that nucleate with respect to power decreases with increasing power, since the relationship between crack number and linear heat rating is logarithmic. The explanation for this, which fits with the data in this work relates to the interaction between stress and crack numbers. If there are more cracks, more strain energy is expended on the growth of those cracks as power increases. This increases the amount of power required to produce the same stress at the surface. If there are more cracks, the surface length between them is smaller, reducing the stress. The first crack appears at the weakest point on the surface of the pellet, and each subsequent crack will appear at a point on the surface that is stronger. If strength were the only determining factor, this effect would not be noticeable in a real pellet, with a vast number of possible crack initiation sites. However, crack initiation tends to occur in exactly the middle of two other cracks, where the stress is highest, falling off to zero with decreasing distance from the nearest crack. This whole process means each crack samples a smaller line segment in the 2D model (surface area in 3D) than the preceding cracks, which will effectively increase the characteristic strength of the material for each new crack.

Using nominal randomisation of strengths on the order of Weibull modulus $\beta = 10$ with no size scaling has some benefit, in that the symmetrical effects of the mesh are lessened. There is still an element of symmetry to the final crack patterns, owing to the square, relatively coarse nature of this mesh. Perhaps the most notable advantage of this degree of randomisation is to allow individual cracks to occur, rather than nucleating many at once. This means the number of cracks in the pellet follows a

smoother trend with respect to the power. This is the only significant difference between this randomisation scheme and the no randomisation scheme. This makes sense, since the express goal of this nominal randomisation in other work is to avoid the qualitative problems associated with a homogenous strength distribution, without changing the quantitative results.

Using a much greater degree of randomisation (the amount that would realistically be seen in a ceramic like a UO_2 fuel pellet) better spread the gap in power between cracks, and also reduced the maximum number of cracks to be more in line with the Walton and Husser PIE data. Reducing the Weibull shape parameter further may produce an even better fit to this data, but produces artificial crack nucleation behaviour because the fracture strains in the surface region are raised so high relative to the interior bonds, that the interior bonds reach their fracture strain first. This issue stems from the fact that bond failure is determined by failure strains, assigned with the goal of reproducing Weibull distributions, which govern crack initiation, but make no prediction about crack growth. The interior bonds fail at strain greater than 5.34×10^{-4}, the characteristic strain of the Weibull distribution, based on the literature value for UO_2 fracture stress [20]. Due to the Weibull distribution scaling, surface bonds typically fail at much higher strains, with only isolated instances of lower failure strains, dictating where cracks nucleate. In the low Weibull modulus ($\beta = 5$) case, this is more pronounced, producing cracking in the interior, which is now weaker than the surface. Bonds on the surface being stronger than those in the interior is at odds with the reality that the surface contains bigger flaws, and is therefore 'weaker' in reality. This bond strength scheme is used only to achieve the required Weibull-type behaviour. Using a different

failure criterion for the interior bonds could be justified, since the strain criterion is intended to control the initiation of fracture, rather than the growth of cracks. What is clear is that the reduction in number of cracks nucleating relative to power with increasing power is more accurately described when applying a reasonably accurate amount of material strength randomisation. The exact optimal value of Weibull shape parameter β is not fully defined by this work, but it is clear that a value in the region of 5 – 10 would be sensible.

6.4.1 Comparison to models and PIE

Qualitatively, the crack patterns are difficult to assess. The model has no capacity to create surfaces that interact with each other properly so ramping down power does not necessarily produce accurate results. Assessing the crack patterns against PIE is therefore somewhat difficult. Comparing to other explicit cracking methods shows a good similarity with some, with cracks growing toward the centre but not penetrating into the central compressive stress zone. This may not be an entirely accurate description of the behaviour of crack growth. It does not fit the model described by Oguma [5] nor does it particularly closely match the schematics outlined by Walton & Husser [1]. This uncertainty around the behaviour in the bulk of the pellet is more reason to avoid fitting too exactly to the Walton and Husser data, since this behaviour affects the number of cracks nucleating with increasing power. A more robust model of crack growth in the bulk of the pellet would be required before fine tuning the initiation behaviour any further.

Since direct comparison to PIE data is difficult due to the inability of the model to accurately represent cracks originating during a power down-ramp, it is useful to

compare the model to other models in the literature. In other modelling of pellet cracking, crack paths are broadly straight, radial and originate from the surface after an increase in power but before a decrease (see Figure 6-2 and Figure 6-15). Hierarchical crack growth is also visible. It is notable that when a lower fracture criterion was used by Jiang et al. in [4], cracks continued to grow, curving around the centre of the pellet.

In the case of Wang et al. [7] the power set to the full power rating instantly at the start of the simulation and in [8] over the power is ramped up over 5 s, resulting in more thermal shock than occurs in the other work. That both heating regimes resulted in straight, radial cracks is evidence that the circumferential cracks seen in PIE occur in a part of the power history not related to increasing power. From this evidence it can be stated with some confidence that the crack patterns shown in the peridynamics simulations run for this work display a crack pattern which is broadly consistent with other modelling work in the literature.

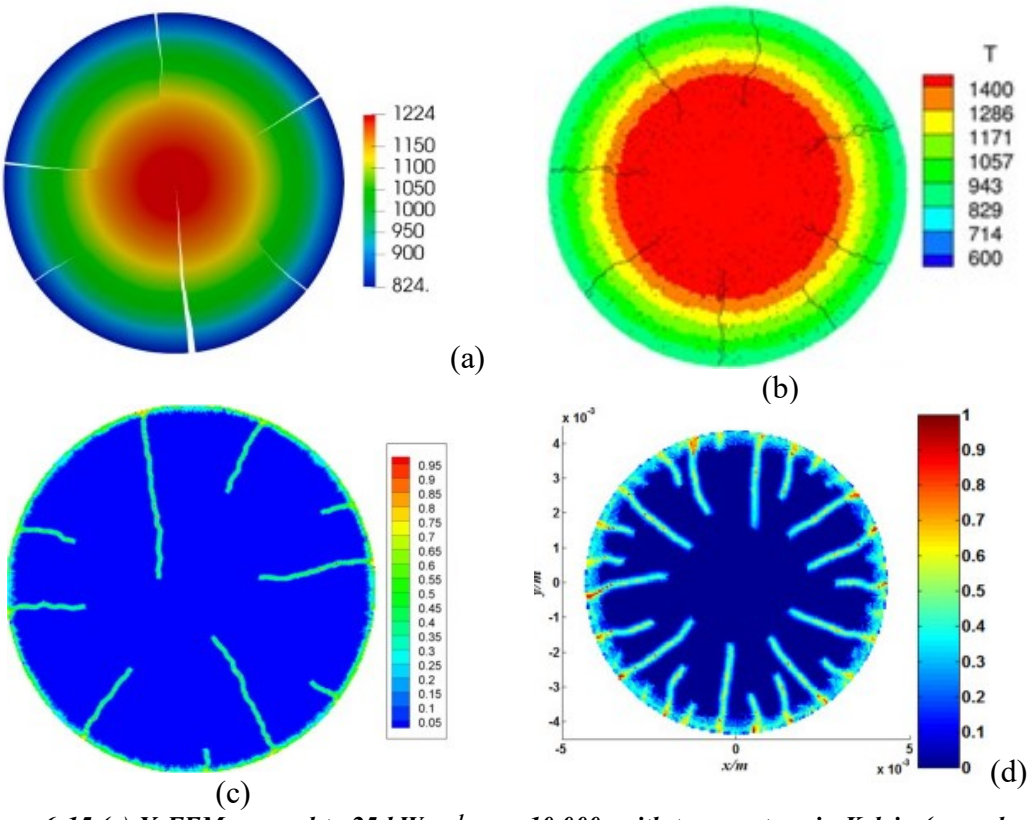

Figure 6-15 (a) X-FEM ramped to 25 kW m^{-1} over 10,000s with temperature in Kelvin (reproduced from [4]), (b) DEM ramped to 40 kW m^{-1} over 10,000s with temperature in Kelvin (reproduced from [3]), (c) peridynamics pellet ramped instantly to ~10 kWm^{-1} and held at power for 4.5s with colour marking fraction of damaged bonds connected to a material point (reproduced from [8]), (d) Peridynamics pellet ramped to 45kW m^{-1} over 5s and held at power for a further 5s with colour fraction of damaged bonds connected to a material point (reproduced from [7]).

In the simulations in [7] circumferential cracks nucleated on crack surfaces upon ramping down the power rating. The crack pattern in Figure 6-16 (b) is presented in [7] in comparison to the PIE crack pattern in Figure 6-17 (a) as evidence of accuracy in representing PIE crack patterns. From this, the conclusion can reasonably be drawn that the peridynamics simulations run for this work are a reasonable representation of the behaviour of real pellets, given that they are a good match to the simulations in [7], and they are in turn a good match to PIE. That no additional radial cracks initiate on the surface on the power down-ramp is evidence that the crack numbers recorded are usefully comparable to the Walton and Husser data.

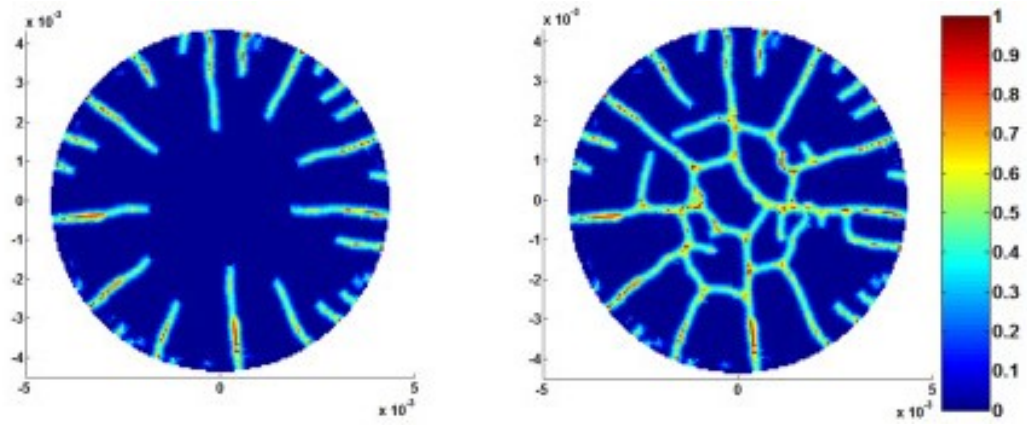

(a) (b)

Figure 6-16 (a) Peridynamics pellet after being ramped to 25 kW m^{-1} over 5s, and (b) after being held at power for 5s, then ramped down to 0 kW m^{-1} over 5s. Colours show damage, meaning the proportion of bonds connected to a material point that have failed.Reproduced from [7].

A notable difference between the modelled crack patterns and PIE images is an absence of cracks from surface to surface through the central region of the pellet, of the kind outlined by Oguma [5]. Given that Oguma's is a relatively simple analytical model compared to modern numerical models, there should be no rush to alter models to match its results. Cracks of this type do seem to appear in PIE though. A strong candidate for such a crack can be seen in Figure 6-17 (b) and a possible one in Figure 6-17 (c). The reason for the absence of such cracks in the explicit numerical methods explored here is not clear. It may be caused by over-constraining the mesh in the central region.

It should be noted that off the five models presented here (the peridynamics model presented in this thesis, plus the models of Huang et al. [3], Wang et al. [7], Oterkus and Madenci [8], and Jiang et al. [4]) only the models by Huang et al. [3] and Wang et al. [7] implemented contact between pellet and cladding. Any difference between the pellet crack patterns in these works and observed crack patterns from PIE is therefore

not thought to be due to PCMI or a lack thereof. The models with cladding did not produce any characteristics not seen in the models without.

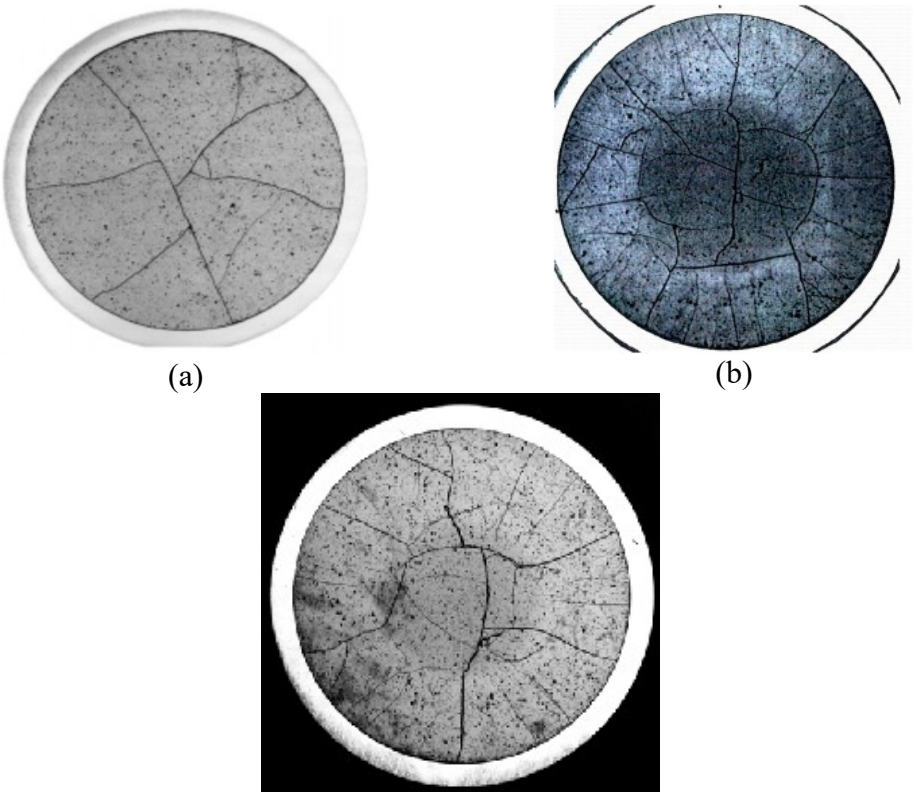

(a) (b)

(c)

Figure 6-17 Crack patterns from PIE (a) after base irradiation,(b) after a power ramp test, both reproduced from Michel et al. [22] (c) ramped to 40 kWm^{-1} reproduced from Nonon et al. [23]

6.5 Conclusions

- The model presented is based on a 2-dimensional application of Weibull theory to peridynamics, presented in chapter 5, that can recreate the observed relationship between pellet radial crack number and linear power rating, in low-burnup nuclear fuel, with reasonable accuracy, relative to available PIE data.
- Crack patterns produced using this 2-dimensional peridynamics method are shown to be similar to other models up to the approximate point in the power history modelled, where such models have been shown to produce accurate crack patterns relative to PIE data after a complete power history. It can

therefore be stated with some confidence that the qualitative patterns shown by the 2-dimensional peridynamics method in this work are accurate.

- Using the fracture strain of UO_2 as the critical strain for peridynamics bonds produces a nuclear fuel pellet model that first nucleates radial cracks at the expected linear power rating (~5kW m^{-1}) but without randomisation of bond failure strains, subsequent radial cracks nucleate at lower powers than expected relative to PIE data. Using a Weibull distribution for the failure strains improves the fit, and scaling the distribution to account for the size of the bonds relative to the pellet improves it further.
- Standard UO_2 nuclear fuel pellets are most appropriately modelled using a Weibull shape parameter, β, of 5-10, although using the method outline in this work necessitates using the higher end of this range to avoid artificial crack nucleation in near-surface regions.

6.6 References

[1] L. A. Walton and D. L. Husser, "Fuel pellet fracture and relocation," Art. no. IWGFPT--13, 1983, Accessed: Nov. 03, 2020. [Online]. Available: http://inis.iaea.org/Search/search.aspx?orig_q=RN:17006978

[2] T. Barani, D. Pizzocri, G. Pastore, L. Luzzi, and J. D. Hales, "Isotropic softening model for fuel cracking in BISON," *Nucl. Eng. Des.*, vol. 342, pp. 257–263, Feb. 2019, doi: 10.1016/j.nucengdes.2018.12.005.

[3] H. Huang, B. Spencer, and J. Hales, "Discrete element method for simulation of early-life thermal fracturing behavior in ceramic nuclear fuel pellets," *Nucl. Eng. Des.*, vol. 278, pp. 515–528, Oct. 2014, doi: 10.1016/j.nucengdes.2014.05.049.

[4] W. Jiang, B. W. Spencer, and J. E. Dolbow, "Ceramic nuclear fuel fracture modeling with the extended finite element method," *Eng. Fract. Mech.*, p. 106713, Oct. 2019, doi: 10.1016/j.engfracmech.2019.106713.

[5] M. Oguma, "Cracking and relocation behavior of nuclear fuel pellets during rise to power," *Nucl. Eng. Des.*, vol. 76, no. 1, pp. 35–45, Oct. 1983, doi: 10.1016/0029-5493(83)90045-6.

[6] Y. Wang, X. Zhou, and Y. Shou, "The modeling of crack propagation and coalescence in rocks under uniaxial compression using the novel conjugated

bond-based peridynamics," *Int. J. Mech. Sci.*, vol. 128–129, pp. 614–643, Aug. 2017, doi: 10.1016/j.ijmecsci.2017.05.019.
[7] Y. Wang, X. Zhou, and M. Kou, "Peridynamic investigation on thermal fracturing behavior of ceramic nuclear fuel pellets under power cycles," *Ceram. Int.*, vol. 44, no. 10, pp. 11512–11542, Jul. 2018, doi: 10.1016/j.ceramint.2018.03.214.
[8] S. Oterkus and E. Madenci, "Peridynamic modeling of fuel pellet cracking," *Eng. Fract. Mech.*, vol. 176, pp. 23–37, May 2017, doi: 10.1016/j.engfracmech.2017.02.014.
[9] W. Li and K. Shirvan, "Multiphysics phase-field modeling of quasi-static cracking in urania ceramic nuclear fuel," *Ceram. Int.*, Aug. 2020, doi: 10.1016/j.ceramint.2020.08.191.
[10] R. Mella, "Finite Element Modelling of the Advanced Gas-Cooled Reactor Fuel Performance," PhD, Imperial College, London, 2014.
[11] R. Mella and M. R. Wenman, "Modelling explicit fracture of nuclear fuel pellets using peridynamics," *J. Nucl. Mater.*, vol. 467, Part 1, pp. 58–67, Dec. 2015, doi: 10.1016/j.jnucmat.2015.08.037.
[12] D. R. Askeland and P. P. Phulé, *The Science and Engineering of Materials*. Thomson Brooks/Cole, 2003.
[13] L. D. Jones, L. J. Vandeperre, T. A. Haynes, and M. R. Wenman, "Modelling of Weibull Distributions in Brittle Solids Using 2-Dimensional Peridynamics," *Procedia Struct. Integr.*, vol. 28, pp. 1856–1874, Jan. 2020, doi: 10.1016/j.prostr.2020.11.009.
[14] L. D. Jones, T. A. Haynes, L. J. Vandeperre, and M. R. Wenman, "Theory and application of Weibull distributions to 1D peridynamics for brittle solids," *Comput. Methods Appl. Mech. Eng.*, vol. 363, p. 112903, May 2020, doi: 10.1016/j.cma.2020.112903.
[15] A. A. Griffith, "The Phenomena of Rupture and Flow in Solids," *Philos. Trans. R. Soc. Lond. Ser. Contain. Pap. Math. Phys. Character*, vol. 221, pp. 163–198, 1921.
[16] Y. D. Ha and F. Bobaru, "Studies of dynamic crack propagation and crack branching with peridynamics," *Int. J. Fract.*, vol. 162, no. 1–2, pp. 229–244, Jan. 2010, doi: 10.1007/s10704-010-9442-4.
[17] Y. D. Ha and F. Bobaru, "Characteristics of dynamic brittle fracture captured with peridynamics," *Eng. Fract. Mech.*, vol. 78, no. 6, pp. 1156–1168, Apr. 2011, doi: 10.1016/j.engfracmech.2010.11.020.
[18] G. Rossiter, "ENIGMA Runs - [OFFICIAL]," Sep. 29, 2020.
[19] G. Rossiter, "DEVELOPMENT OF THE ENIGMA FUEL PERFORMANCE CODE FOR WHOLE CORE ANALYSIS AND DRY STORAGE ASSESSMENTS -Nuclear Engineering and Technology | Korea Science," *Nucl. Eng. Technol.*, vol. 43, pp. 489–498, 2011.
[20] "MATPRO - A Library of Materials Properties for Light-Water-Reactor Accident Analysis," Idaho National Engineering and Environmental Laboratory, 20555–0001. [Online]. Available: https://www.nrc.gov/docs/ML0103/ML010330363.pdf

[21] L. J. Vandeperre, A. Kristofferson, E. Carlstrom, and W. J. Clegg, “Thermal Shock of Layered Ceramic Structures with Crack-Deflecting Interfaces,” *J Am Ceram Soc*, vol. 84, no. 1, pp. 104–110, 2001.
[22] B. Michel, J. Sercombe, G. Thouvenin, and R. Chatelet, “3D fuel cracking modelling in pellet cladding mechanical interaction,” *Eng. Fract. Mech.*, vol. 75, no. 11, pp. 3581–3598, Jul. 2008, doi: 10.1016/j.engfracmech.2006.12.014.
[23] C. Nonon *et al.*, “PCI BEHAVIOUR OF CHROMIUM OXIDE-DOPED FUEL,” Aix-en-Provence, Mar. 2004.

Chapter 7 Conclusions and Further Work

- Naively applying Weibull distributions (and by extension other distributions) to the fracture strengths of peridynamic bonds has the effect of producing a different distribution of strengths in the modelled object than intended. The distribution of strengths in a modelled part has a lower characteristic strength than the distribution of the peridynamics bond strengths. This is true for even the simplest possible peridynamics-like model, a one-dimensional tensile test with a horizon ratio $m = 1$, and is due to the facts that fracture is dictated by the lowest strength in the object, and that sampling the same distribution multiple times tends to produce a lower minimum value.
- The most fundamental issue with implementing Weibull distributions in one-dimensional peridynamics (namely the issue that bond strengths must be higher than the intended strengths of the modelled objects they make up) may be solved by scaling the bond strengths according to the size of the bonds relative to the modelled object. This can be done following the established method for scaling Weibull distributions between objects of different sizes.
- Non-locality in peridynamics can hinder the ability to model truly brittle behaviour in modelled object with an applied Weibull distribution. Since bonds may have considerably different fracture strengths (especially when the distributions are scaled according to the difference in size between the bonds and the modelled object) failure of a single bond may not cause sufficient stress redistribution to cause failure of surrounding bonds, even in the one-dimensional case. This leads to discontinuous fracture behaviour more closely

resembling composite materials or low-temperature steels than the brittle fracture intended for modelling ceramics.

- The issue of peridynamics models failing in stages may be addressed by localising the fracture strengths of the bonds by assigning fracture strengths to material points, and having bond fracture strengths defined by the material points around them. In the one-dimensional case, this is done by having the bond fracture strengths defined by the values assigned to the material points at either end of the bond, as well as any bonds in between them. Averaging these values produces a distortion of the lower end of the tail of the Weibull distribution, so the preferred method is to use the most 'extreme' values (i.e. those furthest from the fracture strength at which probability of failure = 0.5) from the considered material points. Since the Weibull distribution is sampled once for each material point rather than once for each bond, the scaling of the distribution should be relative to the difference in size between one material point and the modelled object. This method can be used to accurately recreate Weibull distributions in one-dimensional peridynamics models with horizon ratio $m = 3$ with no restriction on Weibull modulus.
- In the two-dimensional case, the method of localising fracture strength may be applied by having the fracture strength of bond determined by values applied to material points within an area surrounding the bond. This area is defined as the overlap between two circles centred on the material points at the ends of a bond, with radii equal to the length of the bond.
- In the case of a two-dimensional peridynamics model of a tensile test, fracture is overwhelmingly likely to initiate on one of the edges of the mesh running

parallel to the loading direction. For this reason, the Weibull distribution should be scaled according to the number of material points along these edges. Only the bonds connected to a material point on one of these edges should have their fracture strain defined according to a Weibull distribution, and the other bonds should be assigned a single fracture strain, since they are not involved in determining the strain at the initiation of fracture.

- When modelling a tensile test in 2-dimenisonal peridynamics, a Weibull distribution of fracture strains of a modelled part can be accurately recreated from a Weibull distribution of bond fracture strains if the modulus is sufficiently high. Using a Weibull modulus $\beta \geq 10$ produces a very good match to both Weibull parameters, while using a Weibull modulus $\beta \geq 7.5$ introduces an error in characteristic strength. Using Weibull modulus $\beta < 7.5$ produces an error in Weibull modulus of the modelled parts such that the method can no longer be considered sensitive to decreasing Weibull modulus, and is not recommended.
- It is possible to recreate the observed quantitative relationship between radial crack number and linear power rating in a UO_2 nuclear fuel pellet, by applying Weibull theory in the manner described above to a peridynamics model.
- Crack patterns produced using this method are qualitatively a good match to other explicit fuel pellet cracking models. They show radial cracks nucleating on an upwards power ramp, in increasing number with increasing power, and circumferential cracks nucleating between the radial crack tips on a downwards power ramp. This is a reasonable match to crack patterns observed in PIE images, although all models discussed lack cracks which originate on one side

of the pellet and terminate on the other, a commonly observed feature of PIE images.

7.1 Future Work

This work acts as a useful proof-of-concept for Weibull distributions implemented in the Abaqus-based peridynamics method and its capacity to solve nuclear engineering problems although this could be easily extended to many other engineering systems. There are several areas in which it could be improved so as to be a more appropriate tool for such problems. Firstly, the model should be repeated in an implementation where the problem of memory allocation within Abaqus preventing simulations using meshes with large numbers of elements has been overcome in order to match the mesh density seen in other implementations of peridynamics. Increasing mesh refinement would increase computational expense, potentially reducing the sample size that could practically be used, increasing uncertainty with regards to the statistics of fracture, but given the relatively small sample sizes involved, this should not be an insurmountable issue. The mesh could be improved without increasing the number of bonds by making it cylindrical in nature. A mesh defined according to polar coordinates as opposed to cartesian would have a more perfectly circular surface, without the stress concentrating features that occur on the surface of a cartesian mesh of a circular object, like a two-dimensional representation of a PWR fuel pellet.

Using a software architecture that allows larger models would also facilitate moving to 3-dimensions. The current two-dimensional model includes assumptions about the cracking behaviour above and below the modelled plane. A full 3-dimensional model of a pellet would certainly be desirable, and could model the cracking with a much

greater degree of detail and complexity. An interstitial step could be to model a 3-dimensional slice of a pellet with thickness equal to, or perhaps slightly greater than, one horizon. This would allow the explicit modelling of plane strain and plane stress.

In order to model fuel pellet fracture accurately across an entire power history (even a short one with little regard for the long term effects of radiation) it is necessary that the method is improved to include the effect of contact between the pellet and the clad, as well as between the pellet crack faces. Pellet clad contact could be achieved through tying FE elements to the peridynamics mesh, which would then contact on a FE clad. This could negate the need to develop a contact model truly based in peridynamics as implemented in Abaqus, since FE contact is a well-studied issue. Contact between surfaces created by cracking of the peridynamics mesh would be more complex, as even defining such surfaces is made difficult by the non-local nature of the method.

A more immediate further work using the methods outlined in this thesis would be to repeat the simulations while changing the thermo-mechanical properties to represent other fuel types, such as doped fuels, UN, or UC fuels. Understanding the radial cracking behaviour of other fuel types relative to the UO_2 fuel modelled in this thesis would be useful. Some promising work in this area was completed by an MEng student, which could easily be expanded upon by bringing the modelling method more in line with the work in Chapter 6, particularly with regards to the heat transfer model and power histories.

This work was restricted to low burn-up, short power histories, partly by the availability of PIE against which the model could be validated, and to a greater extent

by the inability to model long time-scale processes such as densification, swelling, and creep. Densification and swelling could be implemented without too much difficulty in the Abaqus peridynamics framework, with creep being a longer-term, more difficult issue. Adding the capability to model such behaviour would open up the possibility of modelling more realistic power histories.

A like-for-like comparison between peridynamics and other fracture models such as a phase field model would also be useful. A quantitative and qualitative comparison of the crack patterns obtained by either method, as well as a comparison of computational time would help establish each methods relative utility for modelling nuclear fuel fracture.

This methodology could be used in modelling of other fuel designs. Tri-structural isotropic (TRISO) fuel particles are small (~0.5mm radius) kernels of fissile material coated in protective pyrolitic carbon and silicon carbide layers. The pressure exerted by gaseous fission products on these coating layers is a primary cause of fission product release in TRISO particles. Given the large number of particles present in a core, the statistical nature of mechanical failure of these layers is of significant importance. A model of a TRISO particle utilising the statistical methods used for LWR fuel in this thesis would be useful to industry and academia alike.

There are also applications outside of nuclear for this modelling methodology. In any engineering application where brittle fracture is present, this modelling methodology could be applied. This includes modelling of fracture of embrittled ferritic steels, and engineering ceramics, but also natural rock formations, ice and concrete. In particular,

heterogenous solids and porous materials which are required to be modelled on scales much larger than their heterogeneities would be of interest, since these effects could be captured using relatively coarse meshes, by incorporating the porosity and heterogeneity into model properties.

Lloyd Jones
3rd July 2022
Preston, Lancashire